

MODELING OF MECHANICAL STRESS IN SILICON ISOLATION  
TECHNOLOGY AND ITS INFLUENCE ON DEVICE CHARACTERISTICS

By

HERNAN A. RUEDA

A DISSERTATION PRESENTED TO THE GRADUATE SCHOOL  
OF THE UNIVERSITY OF FLORIDA IN PARTIAL FULFILLMENT  
OF THE REQUIREMENTS FOR THE DEGREE OF  
DOCTOR OF PHILOSOPHY

UNIVERSITY OF FLORIDA

1999

Copyright 1999

By

Hernan Rueda

To my family

## ACKNOWLEDGMENTS

I would like to express my sincere gratitude to Dr. Mark Law, chairman of my advisory committee, for his patience and guidance. He has introduced me to the research area of process modeling, within which this dissertation falls, and has provided valuable advice and direction throughout my master's and doctorate studies.

Thanks also go to Drs. Gijs Bosman, Toshikazu Nishida, Kenneth K. O and Kevin Jones for their interest and participation in serving on my committee and their suggestions and comments.

I would also like to thank the University of Florida Graduate School for its support during my master's program and the Semiconductor Research Corporation for its support of my doctorate studies.

I have been very lucky to work with many industry mentors who have provided invaluable assistance for my graduate studies. I acknowledge Drs. Jim Slinkman and Dureseti Chidambarao of IBM for their suggestions and direction of the STI SKPM experiment. I also thank Dr. Len Borucki of Motorola for assistance in design of the diode bending experiment. Thanks

also go to Drs. Paul Packan and Steve Cea of Intel for many valuable discussions and suggestions on modern device concerns and strain modeling.

I wish to thank my friends who have made my time, over ten years at the University of Florida, a very enjoyable experience. I've been very lucky to meet so many good friends such as all the old TCAD research assistants, the SWAMP group, my many roommates through all the years, and my 'old school' friends back in the 'hood in Miami.

Last but not least, I express my love to my parents, Hernan Sr. and Gloria, and my brother, Camilo, for their never-ending support, love and encouragement throughout my whole life.

## TABLE OF CONTENTS

	<u>page</u>
ACKNOWLEDGMENTS.....	iv
ABSTRACT .....	viii
 CHAPTERS	
1 INTRODUCTION.....	1
1.1 Motivation .....	1
1.2 Stress-Induced Effects in Silicon Fabrication.....	3
1.2.1 Oxidation Influences .....	4
1.2.2 Diffusion Influences .....	6
1.3 Stress-Induced Effects in Silicon Device Operation .....	7
1.3.1 Carrier Mobility Influences.....	7
1.3.2 Energy Band Influences.....	11
1.4 Goals .....	12
1.5 Organization.....	14
 2 PROCESS-INDUCED MECHANICAL STRAIN MODELS.....	 16
2.1 Continuum Mechanics .....	16
2.1.1 The Stress Tensor.....	17
2.1.2 The Strain Tensor.....	20
2.1.3 Stress-Strain Relationships .....	23
2.2 Strain Sources .....	30
2.2.1 Film Stress.....	31
2.2.2 Dopant Induced Stress .....	35
2.2.3 Oxidation Volume Expansion .....	39
2.3 Strain Computation Methods .....	40
2.3.1 Boundary Loading Method.....	45
2.3.2 Fully-Integrated Method.....	47
2.4 Summary .....	48

3	APPLICATION EXAMPLES AND COMPARISONS.....	50
3.1	FEM Comparisons.....	50
3.1.1	LOCOS.....	55
3.1.2	Post-STI Process Re-Oxidation.....	59
3.2	Raman Spectroscopy Measurements and Comparisons.....	65
3.2.1	Raman Simulation Method.....	66
3.2.2	Nitride Film Edge-Induced Stress.....	67
3.3	Boron-Doped Cantilever Bending Comparisons.....	70
3.3.1	Silicon Bulk Micro-Machining.....	70
3.3.2	Cantilever Bending Simulations.....	73
3.4	3D Boundary Loading Method Example (LOCOS).....	80
3.5	Summary.....	82
4	KELVIN PROBE FORCE STI EXPERIMENT.....	85
4.1	Scanning Kelvin Probe Force Microscopy.....	86
4.2	Work Function Influence.....	88
4.3	STI Experiment.....	93
4.4	SKPM Measurements.....	94
4.5	STI Strain Simulations.....	99
4.6	Results and Discussion.....	101
4.7	Summary.....	105
5	STRESS INFLUENCES IN DEVICE OPERATION.....	107
5.1	Uniaxial Stress Influence Experiment.....	107
5.1.1	Stress-Inducing Apparatus Design.....	109
5.1.2	Stress-Wafer Deflection Relationship.....	112
5.2	Experimental Procedure.....	114
5.3	Experimental Results.....	118
5.4	Summary.....	124
6	SUMMARY AND FUTURE WORK.....	126
6.1	Summary.....	126
6.2	Future Work.....	129
6.2.1	SKPM Strain Measurement Calibration Studies.....	129
6.2.2	Effect of Stress on Dislocations.....	130
6.2.3	Silicidation-Induced Stress.....	131
6.2.4	Three-Dimensional Modeling of the STI Process.....	131
	REFERENCES.....	133
	BIOGRAPHICAL SKETCH.....	140

Abstract of Dissertation Presented to the Graduate School  
of the University of Florida in Partial Fulfillment of the  
Requirements for the Degree of Doctor of Philosophy

MODELING OF MECHANICAL STRESS IN SILICON ISOLATION  
TECHNOLOGY AND ITS INFLUENCE ON DEVICE CHARACTERISTICS

By

Hernan Rueda

May 1999

Chairman: Dr. Mark E. Law

Major Department: Electrical and Computer Engineering

One of the challenges the semiconductor industry faces as it attempts and continues the scaling of silicon integrated circuits is understanding and control of mechanical strain resulting from silicon fabrication technology. High magnitudes of strain can be induced under standard fabrication conditions and may produce deleterious effects in device behavior, such as increased current leakage. Current leakage has been identified as a critical device characteristic for future sub-micron dynamic random access memory (DRAM) and complementary metal oxide semiconductor (CMOS) technologies, as it is a limiting factor for increasing switching speeds and decreasing power consumption. The following are various known sources of stress in silicon technology: thermal expansion mismatch, intrinsic stress,



and oxidation volume dilation. This work results from an examination, by modeling, experiment, and simulation, of the contribution of stress due to these sources using the Florida Object-Oriented Process Simulator (FLOOPS).

The contributions of each source can be simulated using different models that represent or approximate the physics involved. After the models are described and presented, example applications are provided to distinguish the advantages and limitations for each model.

Coupling experiment along with process simulation then validates the results and allows for a better understanding of the problem. One such problem examined in this work is the strain induced by the shallow trench isolation (STI) process. STI has become an essential isolation scheme for present and future sub-micron processes. It consists of several sequential steps that exert stress in the silicon active area by each of the previously described sources. Scanning Kelvin probe force microscopy (SKPM) is then applied as a new technique to characterize the strain exerted from STI processes through measurements of strain-induced work function variations in silicon. Qualitative agreement is demonstrated between the SKPM measurements and the work function influence due to finite element based STI induced mechanical strain computations.

Finally, a wafer bending experiment is performed that quantifies the influence of tensile and compressive uniaxial stress on forward current of pn-

junction devices. This effect is then modeled primarily through the strain influences in the silicon bandgap.

## CHAPTER 1 INTRODUCTION

### 1.1 Motivation

During the quest for increasing device density in integrated circuits, many problems are encountered and need to be solved. As some problems are alleviated, new issues emerge. One of the problems gaining importance in silicon fabrication is process-induced mechanical stress. Many of the processes used in silicon IC fabrication individually and cooperatively contribute to the development of stress in the silicon active areas.

Of prime interest is the mechanical stress generated in the isolation process flow. Isolation technology is continually challenged as design rules are scaled. It is well known that high stress magnitudes in certain silicon dioxide structures cause a decrease in oxidation rate [1, 2].

In LOCOS (LOCal Oxidation of Silicon) isolation processes, silicon nitride is deposited over a thin pad oxide and patterned to mask the oxidation of silicon. In order to cope with the necessary electrical isolation at the ever-decreasing linewidths, increasing the stress during oxidation is exploited [3]. This has been achieved by increasing the nitride thickness and decreasing the pad oxide thickness. These techniques provide the sharp

transition from isolation field oxide to active area that is necessary in decreasing pitch lengths for 0.35 micron technologies.

The main problem associated with this trend is that the silicon substrate yields under the increased magnitudes of strain produced [4, 5]. Dislocations that are generated will degrade device performance [5, 6]. Dislocations serve as gettering sites that attract metal atoms introduced during subsequent processes. Junctions are continually becoming shallower, and therefore these nucleated dislocations have an even greater probability of lying across the device junctions lined with metal atoms. Unacceptably increased magnitudes of leakage current then result. Off-state currents are critical design characteristics in logic and memory circuits, limiting the switching speeds, causing increasing power consumption and limiting reliability.

Shallow Trench Isolation (STI) is steadily becoming the predominant isolation technology as minimum feature sizes decrease below the minimum attainable pitch lengths of LOCOS-based technologies. The general STI process flow includes a nitride-patterned reactive ion etch, sacrificial sidewall oxidation, oxide deposition and finally a chemical mechanical polish. However, stress-induced dislocation generation is not exclusive to LOCOS based isolation technologies and is also a factor in designing STI processes since the steps in the STI process may cooperatively strain the enclosed silicon active areas [7].

Aside from isolation processes, other fabrication processes also induce strain in the silicon crystal. Processes such as thin film deposition and dopant introducing processes induce strain that can generate dislocations. As feature sizes decrease, all these different strain-generating sources become closer together and their influences overlap each other. Under these extreme circumstances, it is important to understand strain fields generated by multiple sources neighboring the silicon active areas.

Strain fields may also play a role in affecting process and device behavior other than generating dislocations. For example, in silicon micro-machining, high residual stresses of boron induce bending sensor structures composed of diaphragms and cantilevers [8]. Strained regions have also been shown to affect diffusion of dopants [9]. Also, it is well known that crystal strain affects the energy band structure [10] and carrier mobilities [11]. Both are major parameters influencing the electrical properties of a device. These are just a few of the many concerns related to the strain state of the crystal.

## 1.2 Stress-Induced Effects in Silicon Fabrication

Stress concerns in process design first became significant in LOCOS isolation technologies. As thermal oxidation temperatures are reduced, dislocation densities in silicon increased due to this isolation technology [4]. These effects were attributed to the increased stress magnitudes induced at lower oxidation temperatures due to the increased viscosities of the silicon

dioxide. Since then, the correlation between increased dislocation densities and high stress magnitudes have caused isolation technologies to be a major stress related concern.

Since then the diffusion process has also been reported to be influenced by film-induced stress [12]. This affect has been explained by stress influences on point defect concentrations as well as extended defect size and concentrations such as dislocation loops. As junction depths continue to decrease in the evolution of sub-micron technologies, the stress influences generated by surface films have a greater effect.

### 1.2.1 Oxidation Influences

It is well known that the growth rate of thermal oxidation of silicon has a stress dependence [13]. This stress dependence occurs in nonplanar regions. In thermal oxidation, a volume of silicon reacts into a volume of silicon dioxide that is 2.2 times in volume. For planar oxidation this does not induce a large stress. This is due to the newly grown oxide lifting the old oxide perpendicular to the surface. Since the surface of the oxide is not constrained the oxide is free to move in this direction so negligible stress is induced normal to the Si-SiO<sub>2</sub> interface.

In nonplanar regions such as convex and concave corners of silicon, a strain is exerted in the silicon dioxide. For the convex corners the strain is laterally tensile since the old volume of oxide is stretched around a longer periphery. In concave corners the strain is laterally compressive since the old



volume of oxide is compressed into a smaller periphery. Convex corners occur at the top corners of a trench oxidation and concave corners result at the bottom corners of a trench oxidation and at the Bird's Beak in a LOCOS oxidation.

It was reported through cylinder structure oxidation experiments that the stress induced in these structures reduced the amount of oxide grown as compared to planar oxidation [1, 2, 13]. This behavior has been observed in highly stressed LOCOS processes and in corners of trench oxidation. It has been documented that the stress induced in the oxide alters the oxidation reaction rate, oxidant diffusion of reactant, and the oxide viscosity [2]. All these influences affect the oxidation growth rate.

The stresses generated in the silicon dioxide are relaxed by exerting force on the neighboring films and the silicon substrate. This leads to strained regions in the silicon due to the oxide growth. Silicon is an elastic material for a wide range of strain. However, as the induced stress exceeds the critical yield stress, dislocations in the silicon crystal are generated to relax the strain [14]. The generated dislocations then present problems in device behavior. Therefore, the strain induced in the silicon by oxidation becomes a concern.

Trenches are popular isolation technologies that also exhibit dislocation generation problems [7, 15]. The stress induced by trench structures is due to other sources also. After the reactive ion etch, an

oxidation is performed to provide a low interface state density and a low oxide trap density. This oxidation is the first source of stress in the silicon substrate in the trench fabrication process. Next the trench is filled with a deposited film. This film influences a stress due to its built in intrinsic stress and thermal expansion mismatch. The three sources all act simultaneously influencing strain in the surrounding silicon substrate. Again, the primary concerns are dislocations generated to alleviate the strain in the substrate induced by the trench process.

### 1.2.2 Diffusion Influences

It has been observed that both phosphorus and boron diffusion behavior under silicon nitride films is different than in inert conditions [9]. It has been established that boron and phosphorus diffusion is governed by interactions with point defects, namely silicon interstitials. Ahn attributed the measured diffusion reduction to a vacancy supersaturation and self-interstitial undersaturation that may be due to the compressive stress under the silicon nitride films [12]. Osada later confirmed this by performing similar experiments [16].

These experiments were performed with junction depths of approximately 0.8 microns. Scaling for sub-micron devices has lead to decreasing junction depths. The magnitudes of strain in silicon due to film stress are at a maximum at the film interface. Therefore, it is believed that



an even greater effect is encountered for the shallower junctions that are getting more prevalent in modern technologies.

### 1.3 Stress-Induced Effects in Silicon Device Operation

Interest in mechanical properties of silicon was sparked with the discovery of its piezoresistive effect [17, 18]. This led to the increased interest of the use silicon as a pressure sensor. Sensor research also extended investigation of the mechanical influences on other electrical parameters such as the energy bands of semiconductor crystals [10, 19-22]. As a result, there is satisfactory understanding of how applied mechanical forces affect electrical device behavior. These principles are used mainly in the design of semiconductor mechanical sensors. In the present age mechanical stress is becoming a limitation in silicon device fabrication, these principles also need to be incorporated into microelectronic device behavior.

#### 1.3.1 Carrier Mobility Influences

The influence of mechanical stress on carrier mobility is starting to gain importance in modern microelectronics. It has been shown that in CMOS transistors the transconductance will vary dependent on the magnitude of applied stress and the behavior is dependent on crystal direction of the current flow as well as the type of carrier [23]. This effect is was also noticed and believed to be due to LOCOS-induced stress in SOI

CMOS devices [24]. The variation in transconductance is attributed to the piezoresistance effect on the carrier mobilities.

The piezoresistance effect of semiconductors describes how the resistivity is influenced by mechanical stress. The electric field vector is proportional to the current vector by a symmetrical resistivity tensor of rank two with nine components:

$$\begin{bmatrix} \varepsilon_1 \\ \varepsilon_2 \\ \varepsilon_3 \end{bmatrix} = \begin{bmatrix} \rho_1 & \rho_4 & \rho_6 \\ \rho_4 & \rho_2 & \rho_5 \\ \rho_6 & \rho_5 & \rho_3 \end{bmatrix} \cdot \begin{bmatrix} i_1 \\ i_2 \\ i_3 \end{bmatrix}. \quad (1-1)$$

If the system axis is aligned along the <100> crystal directions, the normal resistivity components  $\rho_1$ ,  $\rho_2$ , and  $\rho_3$  relate the  $\varepsilon$  field vector component to the current vector  $i$  component in the same direction. The cross-resistivity components  $\rho_4$ ,  $\rho_5$ , and  $\rho_6$  relate the  $\varepsilon$  field vector component to the current vector  $i$  component in a perpendicular direction. If in the unstressed state, the normal components have the same magnitude  $\rho$  and the cross components are equal to zero, this reduces to the following isotropic relationship:

$$\varepsilon = \rho i. \quad (1-2)$$

When the crystal is under mechanical stress, the resistivity components change as the following:

$$\begin{bmatrix} \rho_1 \\ \rho_2 \\ \rho_3 \\ \rho_4 \\ \rho_5 \\ \rho_6 \end{bmatrix} = \begin{bmatrix} \rho \\ \rho \\ \rho \\ 0 \\ 0 \\ 0 \end{bmatrix} + \begin{bmatrix} \Delta\rho_1 \\ \Delta\rho_2 \\ \Delta\rho_3 \\ \Delta\rho_4 \\ \Delta\rho_5 \\ \Delta\rho_6 \end{bmatrix}. \quad (1-3)$$

The piezoresistive coefficients relate the stress-induced changes in the resistivity components to the stress tensor influencing the change. This matrix relating the six resistivity components to six stress components consists of 36 piezoresistive coefficients  $\pi_{ij}$ . Due to the cubic crystal symmetries in silicon, the piezoresistance coefficient matrix reduces to three independent components,  $\pi_{11}$ ,  $\pi_{12}$ , and  $\pi_{44}$ :

$$\frac{1}{\rho} \begin{bmatrix} \Delta\rho_1 \\ \Delta\rho_2 \\ \Delta\rho_3 \\ \Delta\rho_4 \\ \Delta\rho_5 \\ \Delta\rho_6 \end{bmatrix} = \begin{bmatrix} \pi_{11} & \pi_{12} & \pi_{12} & 0 & 0 & 0 \\ \pi_{12} & \pi_{11} & \pi_{12} & 0 & 0 & 0 \\ \pi_{12} & \pi_{12} & \pi_{11} & 0 & 0 & 0 \\ 0 & 0 & 0 & \pi_{44} & 0 & 0 \\ 0 & 0 & 0 & 0 & \pi_{44} & 0 \\ 0 & 0 & 0 & 0 & 0 & \pi_{44} \end{bmatrix} \cdot \begin{bmatrix} \sigma_1 \\ \sigma_2 \\ \sigma_3 \\ \sigma_4 \\ \sigma_5 \\ \sigma_6 \end{bmatrix}. \quad (1-4)$$

The stress components are also referenced with the system axis oriented in the  $\langle 100 \rangle$  directions. Smith initiated the investigations of these piezoresistive coefficients and found the following values for silicon at room temperature displayed in Table 1-1 [17, 18].

The piezoresistance coefficients are also dependent on dopant concentration as well as temperature. Later it was found that they would

decrease as the temperature increases and/or the dopant concentration increases.

Table 1-1: Piezoresistive coefficients for silicon [17, 18].

Material	$\rho$ ( $\Omega\text{-cm}$ )	$\pi_{11}$	$\pi_{12}$	$\pi_{44}$
		(10 <sup>-12</sup> cm <sup>2</sup> /dyne)		
p-Si	7.8	+6.6	-1.1	+138.1
n-Si	11.7	-102.2	+53.4	-13.6

The accepted explanation for this phenomenon is the many-valley model [17, 18]. Anisotropic conditions exist when the mobility in one crystal direction is different than the mobility in the other crystal lattice directions. This results when the semiconductor is in a stressed state. The stress tensor distorts the conduction energy bands of the unstressed semiconductor in different magnitudes depending on direction. The energy levels and curvatures of the band energies corresponding to the perpendicular directions are influenced differently by the applied strain. The effective masses of the carriers are proportional to the energy bands' curvatures in reciprocal  $k$  space. Since the carrier mobilities are functions of the carrier effective masses, the strain influence on the energy band level curvatures results in directionally dependent influences on the carrier mobilities and therefore the resistivities of the semiconductor. The energy band shifts are also influenced on dopant concentration and temperature. Therefore the energy band's sensitivity to stress will also be dependent on these influences.

### 1.3.2 Energy Band Influences

The mechanical stress state's influence on the energy bands also affects the electrical behavior of p-n junction devices such as diodes and bipolar transistors. In these devices the operation is governed by the flow of minority carriers. Using a diode as an example, the forward bias current is described by the following relation:

$$I_F = I_s \exp\left(\frac{V_F}{V_T}\right) + I_{R0} \exp\left(\frac{V_F}{2V_T}\right) \quad (1-5)$$

where the saturation current is

$$I_s = qA \left[ \frac{D_p}{L_p} p_{n0} \coth\left(\frac{W_n}{L_p}\right) + \frac{D_n}{L_n} n_{p0} \coth\left(\frac{W_p}{L_n}\right) \right] \quad (1-6)$$

and the recombination current is

$$I_{R0} = \frac{qAn_i W}{2\tau_o} \quad (1-7)$$

The saturation current term is linearly related to the minority carrier densities  $n_{p0}$  and  $p_{n0}$ . The minority carrier densities are directly dependent to the square of the intrinsic carrier density

$$n_{p0} = \frac{n_i^2}{p_{p0}} \quad (1-8)$$

The intrinsic carrier concentration is exponentially dependent to the stress dependent band gap  $E_g$

$$n_i = K_1 T^{3/2} \exp\left(\frac{-E_g}{2kT}\right). \quad (1-9)$$

The stress induced shifts in the conduction and valence energy bands will alter the band gap and therefore ultimately influence the saturation current. Wortman initiated the quantification of the effects of uniaxial and hydrostatic compressive applied external stresses to forward and reverse biased diodes [10, 22].

Mechanical stress also influences the generation/recombination current component of p-n junction devices. Rindner attributed the effect of uniaxial compressive stresses to increased dislocation densities that decreased the carrier lifetimes and therefore increased the generation/recombination current component [25]. This effect becomes the greater influence under higher magnitudes of stress due to the dislocation generation to relax the applied stress.

#### 1.4 Goals

The goals of this work are primarily to develop a system where strain can be computed from multiple sources simultaneously. Silicon IC fabrication involves a sequential flow of many processes that introduce and alter the strain in the crystal. These process-induced strain fields influence the behavior of processes later in the fabrication flow as well as device operation



once the process flow is completed. An accurate strain solution is necessary for further investigation of its effects.

Once the strain in the system is understood, strain dependent models can be developed to help understand unexplained behavior that has been observed that may be due to strain. Such areas may include point defect and extended crystal defect interactions, diffusion kinetics, and band-gap and mobility influences.

Strain simulations also could aid in the development and analysis of isolation process technologies. Often in fabrication process development, the stress levels generated and dislocation densities produced may decide the isolation process required. A strain field simulator could reduce the amount of experimental work necessary for solving these problems.

Another goal of this work is to validate the process induced strain models with experimental measurements. Currently, this is a major hurdle due to the few characterization techniques available for localized sub-micron strain measurement. Micro-Raman spectroscopy has been the most suitable method for investigating localized strains [26]. But as technologies continue to scale towards the 0.1 $\mu$ m generation, this may even surpass micro-Raman's spatial resolution limits. Therefore, in this work Scanning Kelvin probe force microscopy (SKPM) has been investigated as a new method for analyzing localized strains through detecting influences in the silicon work function.

One last goal is to quantify the influence of tensile and compressive stress on pn-junction device current. This would then provide some insight into the mechanical strain influence on leakage currents.

## 1.5 Organization

Chapter two provides descriptions of the various process induced strain sources and discusses how they are modeled in this work. Afterward, the finite element methods that were developed for strain computation are then described.

Results and comparisons between the methods for various processes are included in chapter three. Example applications are provided to distinguish the advantages and limitations for each model. Next, the film edge-induced stress solutions are validated with published micro-Raman measurements. Finally, three-dimensional applications are demonstrated.

Scanning Kelvin probe force microscopy (SKPM) is then explored as a technique for characterizing STI induced strain in chapter four. An STI experiment is performed and strain influence is measured by SKPM. These measurements are then compared with simulations of band gap influences using the models described in chapter two.

An experiment relating mechanical stress to pn-junction device operation is then described in chapter five. This wafer bending experiment addresses uniaxial stress influences on the forward current. This allows for



quantifying the influence on the reverse leakage current through observation in the forward bias.

Finally chapter six concludes with a summary of the research work accomplished and addresses topics for future work.

## CHAPTER 2

### PROCESS-INDUCED MECHANICAL STRAIN MODELS

The solution of strain present in a particular device technology is computed using a finite element method (FEM) formulated to solve for the strain induced by various sources in silicon technology [27, 28]. In a fabricated device, the strain field in the silicon is generated due to various processes at different steps along the fabrication flow. The most critical sources for inducing stress are deposited and grown films. Sources in the silicon crystal such as dopants and extended defects are becoming more important as technologies advance.

In this chapter, a brief review of continuum mechanics is first provided. Next the individual strain sources are then described. The algorithms used to model the strain generated from each source are also discussed. Afterward the finite element methods used to integrate the various strain sources are described.

#### 2.1 Continuum Mechanics

It is the intention that this review refreshes the reader with the theory and notation of continuum mechanics. References are provided for a more

complete description. The stress tensor is first introduced in this section. Next the strain tensor is described. Finally this section concludes with different stress-strain relationships descriptions and how they may relate in silicon processing.

### 2.1.1 The Stress Tensor

Stress is the distribution of internal body forces of varying intensity due to externally applied forces and/or heat [29]. The intensity is represented as the force per unit area of surface on which the force acts. To illustrate this concept, consider an arbitrary continuous and homogeneous body (Figure 2-1) under the applied external forces,  $F_1$ ,  $F_2$ ,  $F_3$ , and  $F_4$ . If the body is sliced into two smaller volumes  $V_1$  and  $V_2$ , then  $V_2$  exerts force on  $V_1$  at their surface

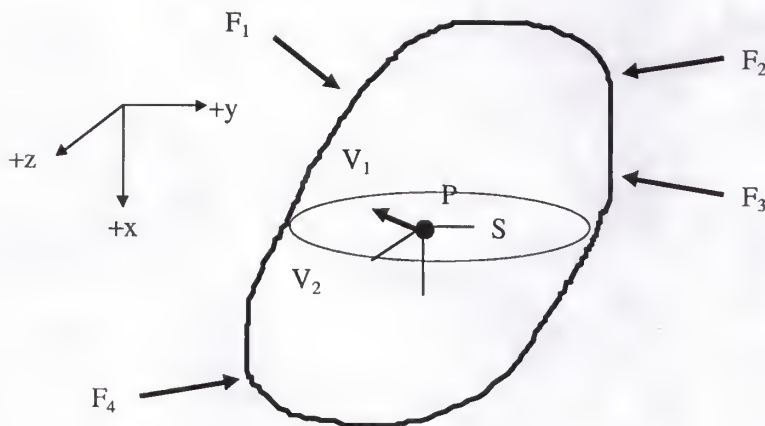


Figure 2-1 Continuous body with external forces applied.

interface  $S$  to remain in equilibrium. The resulting force may be of varying intensities along the surface.

At any point  $P$  on the surface between  $V_1$  and  $V_2$ , the forces can be reduced to a force and a moment, which can be described by a stress vector acting on that surface. Three stress vectors acting on three mutually orthogonal planes intersecting at that point can then determine the stress state at any point  $P$  (Figure 2-2). The stress tensor is composed of the three stress vectors and, according to Cauchy's equations of motion, is sufficient to define the stress state in any element in a body [30].

To illustrate the tensor nature of stress present at point  $P$  in the continuous body, consider a cubic element (Figure 2-2) of infinitesimal

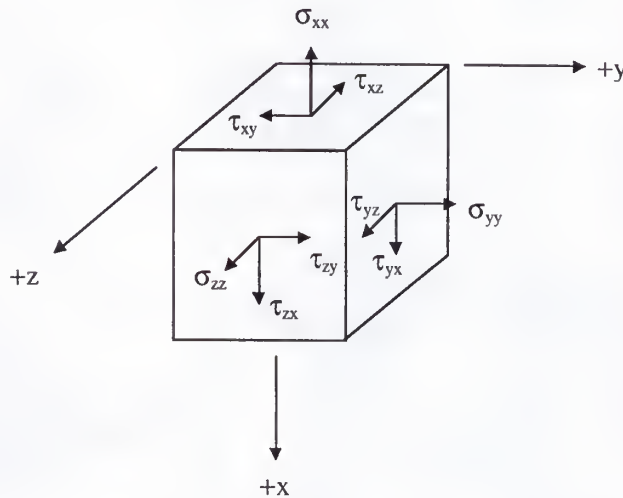


Figure 2-2 An infinitesimal cubic element located within a continuous body with stress tensor components shown.

dimensions located at point P in Figure 2-1. For simplicity of notation, let the cube be aligned perpendicular with the system axis. The stress vector  $T_x$  acting on the plane normal to the  $x$ -direction is the following:

$$T_x = \sigma_{xx} \cdot \hat{x} + \sigma_{xy} \cdot \hat{y} + \sigma_{xz} \cdot \hat{z}. \quad (2-1)$$

Let the surface  $\Delta S$  be the plane of the cube normal to the  $x$ -direction. The stress vector  $T_x$  is defined as the ratio of force acting on that surface area  $\Delta S$ :

$$T_x = \lim_{\Delta S_x \rightarrow 0} \frac{\Delta F_x}{\Delta S_x} = \frac{dF_x}{dS_x} \quad (2-2)$$

The stress tensor on that volume is defined by nine stress components acting on the three surfaces of the cubic element, which make up the three stress vectors  $T_i$ :

$$\sigma_{ij} = \begin{bmatrix} \sigma_{xx} & \tau_{xy} & \tau_{xz} \\ \tau_{yx} & \sigma_{yy} & \tau_{yz} \\ \tau_{zx} & \tau_{zy} & \sigma_{zz} \end{bmatrix}. \quad (2-3)$$

In the definition above,  $\sigma_{ii}$  are the normal stress components acting on the faces perpendicular to  $i$ -direction and  $\tau_{ij}$  are the shear stress components oriented in the  $j$ -direction on the face with normal in the  $i$ -direction. At mechanical equilibrium, it can be shown that the stress tensor is symmetrical [29],

$$\tau_{ij} = \tau_{ji}. \quad (2-4)$$

A column vector of six independent components can then describe the state of stress at a point:

$$\sigma^T = [\sigma_{xx} \quad \sigma_{yy} \quad \sigma_{zz} \quad \tau_{xy} \quad \tau_{yz} \quad \tau_{zx}]. \quad (2-5)$$

### 2.1.2 The Strain Tensor

The application of stress to a body in equilibrium causes it to undergo deformation and/or motion. A measure of deformation is strain. Two common measures for strain are the Lagrangian and the Eulerian definitions. Both are functions of the initial and final dimensions. When the displacement between the final and initial measurement is referenced to the original position dimensions then it is known as the Lagrangian definition. The Eulerian definition describes the deformation displacement referenced with respect to the deformed position.

Figure 2-3 shows a one-dimensional example of the deformation in a

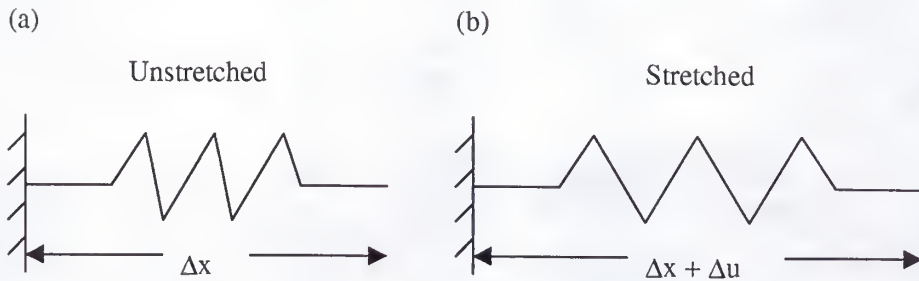


Figure 2-3 One-dimensional deformation of a spring: (a) original length ( $\Delta x$ ), (b) deformed length ( $\Delta x + \Delta u$ ).



spring. The Lagrangian strain and Eulerian strain then, respectively, become the following over the length of the spring:

$$\varepsilon_{Log} \equiv \frac{\text{increase in length}}{\text{original length}} = \frac{\Delta u}{\Delta x} \quad (2-6)$$

$$\varepsilon_{Eul} \equiv \frac{\text{increase in length}}{\text{deformed length}} = \frac{\Delta u}{\Delta x + \Delta u}. \quad (2-7)$$

For the case of infinitesimal deformation, the Eulerian and Lagrangian descriptions become equivalent. An infinitesimal deformation approximation requires that the maximum deformations involved be much smaller than the smallest dimension of the deformed body. A second requirement is that the deformation gradient is much less than one. When these assumptions hold, the infinitesimal strain can be defined by the following relationship for any point in the spring [31]:

$$\varepsilon = \lim_{\Delta x \rightarrow 0} \frac{\Delta u}{\Delta x} = \frac{\partial u}{\partial x}. \quad (2-8)$$

By expanding this definition in three dimensions, the strain is related to the displacements by the following strain components [30]:

$$\begin{aligned} \varepsilon_{xx} &= \frac{\partial u}{\partial x} & \varepsilon_{xy} &= \varepsilon_{yx} = \frac{1}{2} \left( \frac{\partial u}{\partial y} + \frac{\partial v}{\partial x} \right) \\ \varepsilon_{yy} &= \frac{\partial v}{\partial y} & \varepsilon_{yz} &= \varepsilon_{zy} = \frac{1}{2} \left( \frac{\partial v}{\partial z} + \frac{\partial w}{\partial y} \right) \\ \varepsilon_{zz} &= \frac{\partial w}{\partial z} & \varepsilon_{zx} &= \varepsilon_{xz} = \frac{1}{2} \left( \frac{\partial u}{\partial z} + \frac{\partial w}{\partial x} \right) \end{aligned} \quad (2-9)$$

where  $u, v, w$  are the displacements in the  $x, y$ , and  $z$  directions, respectively. These components make up the strain tensor ( $\epsilon_{kl}$ ) that is analogous to the stress tensor:

$$\epsilon_{kl} = \begin{bmatrix} \epsilon_{xx} & \epsilon_{xy} & \epsilon_{xz} \\ \epsilon_{yx} & \epsilon_{yy} & \epsilon_{yz} \\ \epsilon_{zx} & \epsilon_{zy} & \epsilon_{zz} \end{bmatrix}. \quad (2-10)$$

A three-dimensional example of a body undergoing deformation due to an externally applied force is illustrated in Figure 2-4. In the example a compressive force is applied to the infinitesimal cube in the  $x$ -direction. A negative displacement (compressive strain) results in the  $x$ -direction and positive displacements (tensile strains) result in the  $y$ - and  $z$ - directions. The

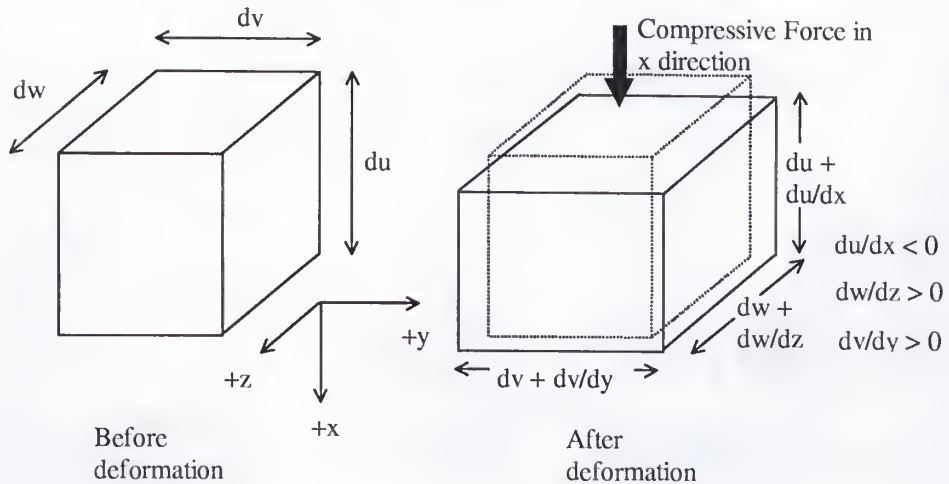


Figure 2-4 Strain reference example displaying a compressive stress in the  $x$ -direction that generates normal strains in the  $x$ -,  $y$ -, and  $z$ -directions.



relationship of how the strain in each dimension results from the applied force will be discussed next.

### 2.1.3 Stress-Strain Relationships

Bodies of different materials but of same dimensions may deform differently under the same stress application. The relationship between the stress tensor and the deformation is known as a constitutive relation. It may vary for a given material depending on conditions such as temperature and pressure.

Elasticity. All structural materials possess, to some extent, the property of elasticity. Elastic bodies possess memory during deformation. For example, when a force is applied on an elastic solid, it will deform until it reaches its elastic yield limit or until the load is released. Microscopically the bonds between atoms that compose the solid 'stretch' during elastic deformation. When the force is removed the body will return to its original shape if it is an ideal elastic body and it had not reached its yield stress, similarly to an ideal spring. When the load is removed the bonds return to their unstressed lengths corresponding to the original environmental conditions.

For a Hookean elastic solid, the stress tensor is linearly proportional to the strain tensor over a specific range of deformation:

$$\sigma_{ij} = c_{ijkl} \epsilon_{kl} \quad (2-11)$$

by the tensor of elastic constants  $c_{ijkl}$  [30]. In order to relate each of the nine elements of the second rank strain tensor to each of the nine elements of the second rank stress tensor,  $c_{ijkl}$  consists of a fourth rank tensor of 81 elements. However due to the symmetries involved for the stress and strain tensors under equilibrium,  $c_{ijkl}$  is reduced to a tensor of 36 elements.

Crystal silicon has diamond cubic crystal geometry resulting from its strong directional covalent bonds. For such crystals,  $c_{ijkl}$  has the following form due to their cubic symmetry [32]:

$$c_{ijkl} = \begin{bmatrix} c_{11} & c_{12} & c_{12} & 0 & 0 & 0 \\ c_{12} & c_{11} & c_{12} & 0 & 0 & 0 \\ c_{12} & c_{12} & c_{11} & 0 & 0 & 0 \\ 0 & 0 & 0 & c_{44} & 0 & 0 \\ 0 & 0 & 0 & 0 & c_{44} & 0 \\ 0 & 0 & 0 & 0 & 0 & c_{44} \end{bmatrix}. \quad (2-12)$$

Thus, for silicon the tensor of elastic stiffness constants reduces to the three independent components:  $c_{11}$ ,  $c_{12}$ , and  $c_{44}$ . Due to the crystal's lattice temperature dependence, the elastic constants are also thermally dependent.

At room temperature (25°C) the elastic constants have been measured as the following for silicon [33, 34]:

$$\begin{aligned} c_{11} &= 1.657 \times 10^{12} \text{ dyn/cm}^2 \\ c_{12} &= 0.639 \times 10^{12} \text{ dyn/cm}^2 \\ c_{44} &= 0.7956 \times 10^{12} \text{ dyn/cm}^2. \end{aligned}$$

The elastic constants' thermal dependence has been documented as the following linear relationship for silicon [35]:

$$Tc_{11} \equiv \frac{\Delta c_{11}}{c_{11}} = -75 \times 10^{-6} / K^{\circ}$$

$$Tc_{12} \equiv \frac{\Delta c_{12}}{c_{12}} = -24.5 \times 10^{-6} / K^{\circ}$$

$$Tc_{44} \equiv \frac{\Delta c_{44}}{c_{44}} = -55.5 \times 10^{-6} / K^{\circ}.$$

From the above linear dependence, it can be seen that the elastic constants do not change significantly for large temperature changes. Also the degree of anisotropy does not change significantly for the range of 100-900°K [36]. These studies support that silicon acts as an anisotropic elastic material over a wide temperature range frequently encountered in silicon IC fabrication.

Although silicon is an anisotropic crystal, it is sometimes desirable to approximate it with isotropic elastic properties for simplification. When the components of elastic constants for a material are equal for any rotation of the reference axis, the material is said to be isotropic. This means that the elastic properties of the material are the same in all directions. The tensor of elastic constants for an isotropic material reduces to the following:

$$c_{11} = \frac{E(1-\nu)}{(1+\nu)(1-2\nu)} \quad (2-13)$$

$$c_{12} = \frac{E\nu}{(1+\nu)(1-2\nu)} \quad (2-14)$$

$$c_{44} = \frac{E}{(1+\nu)} \quad (2-15)$$

where E represents the Young's modulus and  $\nu$  represents the Poisson's ratio. As was demonstrated in Figure 2-4, contractions in one dimension may be accompanied by dilations in other dimensions. The Young's modulus is a measure relating stress and strain for an elastic material when stress is

applied in one direction and the other directions are free to deform as in Figure 2-4. The Poisson's ratio is a material property describing the ratio of a strain perpendicular to the applied stress to the strain oriented in the direction of the applied stress.

Due to its anisotropy,  $E$  and  $\nu$  vary depending in the direction of the applied stress and plane acted upon for silicon. At room temperature  $E$  may vary from  $1.3 \times 10^{12}$  dyn/cm<sup>2</sup> (for  $\langle 100 \rangle$  directions) to  $1.875 \times 10^{12}$  dyn/cm<sup>2</sup> (for  $\langle 111 \rangle$  directions). Poisson's ratio also may vary from 0.06 to 0.34 for the same conditions. The following are measured values for  $E$  and  $\nu$  in silicon at room temperature [32, 33, 35]:

$$\begin{aligned} E_{[100]} &= 1.31 \times 10^{12} \text{ dyn/cm}^2 \\ E_{[110]} &= 1.69 \times 10^{12} \text{ dyn/cm}^2 \\ E_{[111]} &= 1.875 \times 10^{12} \text{ dyn/cm}^2 \\ \nu_{[100]} &= 0.279. \end{aligned}$$

Viscosity. Although silicon deforms elastically over a wide temperature and load range, other materials used in silicon fabrication behave differently. Some deform elastically at temperatures near room temperature and flow at higher temperatures with fluid behavior. Silicon dioxide (SiO<sub>2</sub>) and silicon nitride (Si<sub>3</sub>N<sub>4</sub>) are examples of this these type of materials. Fluids resist deformation with viscous behavior.

As was previously mentioned, Hookean elastic solids will return to their original shape after an applied stress is removed. Materials with viscous constitutive properties may not. Viscous bodies relax or minimize the



strain associated with an applied stress. As the strain is relaxed the stress also reduces. Due to the reduction in strain, when the applied stress is removed, the body will retain its currently deformed shape.

Microscopically, in bodies with viscous mechanical properties, the bonds between atoms that compose the solid break during deformation. New bonds are then formed and re-broken as the body deforms under an applied force. When the applied force is removed the bonds remain in their current configurations.

A common constitutive relationship for a viscous body is the Newtonian fluid. In a Newtonian relationship, the shear stress on the surface is linearly proportional to the rate of deformation [30]:

$$\sigma_{ij} \propto \mu_{ijkl} \dot{\epsilon}_{kl} \quad (2-16)$$

where  $\mu_{ijkl}$  is the tensor of viscosity coefficients. The components of  $\mu_{ijkl}$  for fluids are not as well known as  $c_{ijkl}$  for elastic solids. However, most fluids appear to behave isotropically. An isotropic approximation with the restriction of incompressibility (constant density) allows for the following constitutive relationship known as a Stokes fluid [30]:

$$\sigma_{ij} = -p\delta_{ij} + \mu\dot{\epsilon}_{ij} \quad (2-17)$$

where  $\mu$  now is a scalar that represents the viscosity of the fluid. The normal stress components are dependent on the static pressure  $p$  of the fluid where  $\delta_{ij}$  represents the Kronecker delta function.

Viscoelasticity. It has been recognized that some materials deform with a combination of elastic and viscous properties. There are various models that have been formulated to describe the mechanical behavior of viscoelastic bodies. In the Maxwell model of viscoelasticity, the total strain is simply the sum of the strain due to elastic deformation and the strain due to viscous deformation:

$$\varepsilon = \varepsilon_E + \varepsilon_V. \quad (2-18)$$

This relationship can then be expanded to formulate the well-known Maxwellian viscoelastic relationship between stress and strain:

$$\dot{\varepsilon} = \frac{\dot{\sigma}}{E} + \frac{\sigma}{\mu} \quad (2-19)$$

where  $E$  is the elastic modulus and  $\mu$  is the viscosity of the material. Figure 2-5 illustrates the differences in deformation responses among a Hookean elastic, Newtonian viscous and a Maxwellian viscoelastic material given the same applied pulsed stress. Notice that the viscous and viscoelastic response are time-dependent. Instantaneously after the stress is applied, the viscoelastic body deforms elastically. Later when the applied stress is constant, the viscoelastic body begins to display a linear viscous deformation. As the applied stress is removed, the viscoelastic body then 'elastically' deforms towards its original strain state. However due to the viscous relaxation component, it does not return to its original strain state.

Therefore, for the Maxwellian viscoelastic relationship, the short-term deformation is elastic and the long-term deformation is viscous.

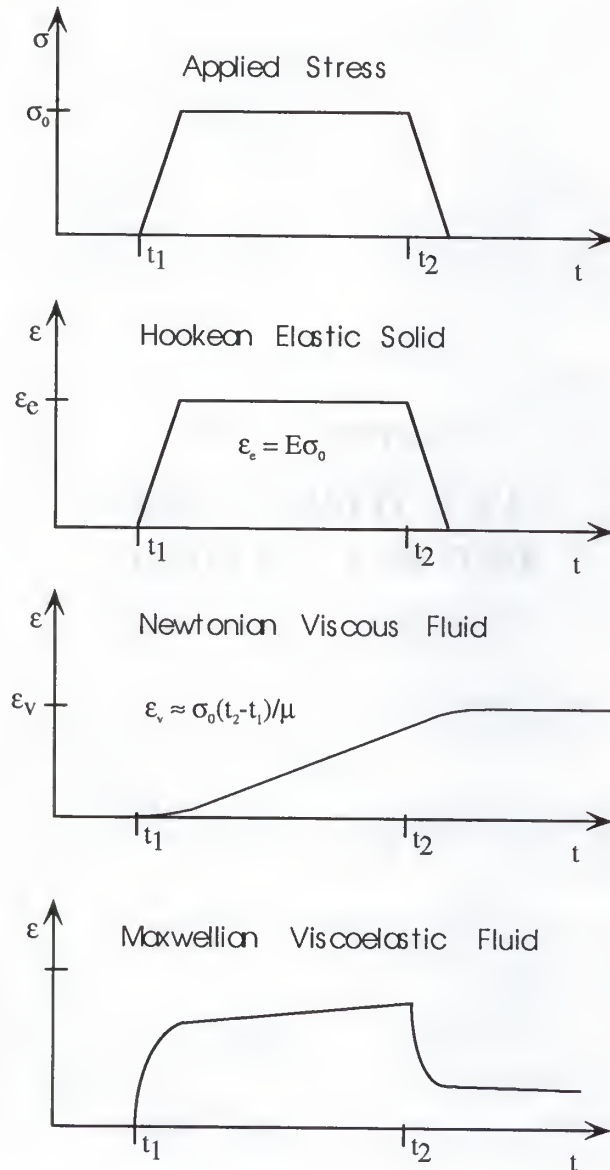


Figure 2-5 Comparison in loading response among Hookean elastic, Newtonian viscous and Maxwellian viscoelastic relationships.

In silicon IC fabrication, oxide ( $\text{SiO}_2$ ) is considered to behave nonlinearly viscoelastic at midrange (800-1100°C) anneal temperatures [2, 14]. The nonlinearity is due to the fact that the degree of its viscosity is also stress dependent. Nitride has been recognized to behave as a viscous body in this same temperature range [37].

Not very many materials behave exactly as a Hookean elastic solid, a Newtonian viscous fluid, or a Maxwellian viscoelastic fluid. However in limited ranges of stress, strain, and temperature, these constitutive relations can approximate their deformation behavior quite well. As an example silicon behaves elastically for a wide temperature and stress range. However under high stresses, silicon will yield and nucleate dislocations and defects in the crystal to relax the stress present. Therefore it is important to learn under what conditions this will result.

## 2.2 Strain Sources

The individual strain sources included for strain computation are discussed next. Three different strain sources are modeled and integrated: film-induced, dopant-induced, and oxidation volume expansion induced strain. Each strain source is discussed and explanations of how they induce strain in the bulk are included. Following each is a discussion on how the strain induced is modeled using the finite element method.



### 2.2.1 Film Stress

Physics. As silicon technology progresses, layers upon layers of different materials are grown and deposited on top of and adjacent to each other. When materials that have different structural, mechanical and thermal properties are attached to each other, strains in each of the materials can result. Adjacent material films relax or expand differently based on their material properties. This causes one film to stretch or contract the other film in a manner that will cause a local strain in each film. Large localized stresses can result due to discontinuous films in regions such as at the film edges and in non-planar sections.

According to Hu [14], stresses result in thin films due to two different mechanisms. The first is referred to as an 'extrinsic' stress and is primarily due to thermal expansion mismatch of neighboring materials. The process used to deposit the film is done at an elevated temperature ranging from 150-1200°C. After the process is over and the thin film is deposited, subsequent thermal cycles will cause the film to expand and contract. If the film was attached to or restrained by a rigid material that does not thermally deform, the amount of strain induced is linearly proportional to the temperature difference:

$$\varepsilon_{th} = \alpha_{th} \cdot \Delta T \quad (2-20)$$

where  $\alpha_{th}$  is the linear thermal expansion coefficient of the film material. The body experiences an increase in volume in each normal direction. No shear

components result from the thermal difference. For many materials the thermal expansion coefficient is not necessarily constant or linear over a wide temperature range. For silicon,  $\alpha_{th}$  varies  $2.5-4.5 \times 10^{-6} / ^\circ K$  over the 300-900K temperature range. Oxygen content and dopant concentration are factors leading to  $\alpha_{th}$  variations.

If the material that the film is attached to also expands due to a thermal increase then the local strain at the interface that is produced is due to the difference in thermal expansion coefficients:

$$\epsilon_{th} = (\alpha_{th1} - \alpha_{th2}) \cdot \Delta T. \quad (2-21)$$

Thermal mismatch stress is often incorrectly shortened and referred to as thermal stress. However, thermal stress is due to thermal gradients within a material. This often occurs in the wafers during before and after temperature cycles. As the wafers cool down, the maximum stress is due to surface tension. However to maintain force equilibrium the interior of the wafer must be in compression. As the wafer heats up, the surface proceeds to expand due to thermal expansion. However, the cooler interior of the wafer restricts this expansion causing a compressive stress at the surface and a tensile stress in the interior. Thermal stress primarily occurs in the substrate as its thickness allows for a greater thermal gradient between the surface and the interior. The thermal stress in the substrate becomes a problem during temperature ramp rates encountered in Rapid Thermal Annealing (RTA). At higher temperature ramp rates, the thermal stress built up from

the high temperature gradient may exceed the yield stress and cause the wafer to shatter. Normally the thicknesses of grown and deposited films in IC fabrication are so thin that a negligible thermal gradient exists across them.

The other source of stress encountered in thin films is the 'intrinsic' stress. Several researchers attribute this stress as due to growth mechanism of the material during the process. For grown oxides, the intrinsic stress results from the planar volume expansion resulting from the oxidation reaction. This stress should not be confused with the stress induced at isolation edges, which is non-planar and is a multidimensional problem discussed later. Other material films such as polysilicon, silicon nitride, and silicides exhibit intrinsic stress also.

After a film is deposited or grown, the wafer will warp according to the total stress in the film. A highly tensile film will bend the wafer's edges towards the film and the reverse for a compressive film. A popular technique for measuring film stress is to measure the amount of wafer curvature optically. The total film stress is then proportional to the radius of curvature by the following relation [38]:

$$\sigma_f = \frac{E_s}{6(1-\nu_s)R} \cdot \frac{t_s^2}{t_f} \quad (2-22)$$

where  $E_s$  and  $\nu_s$  are the elastic properties of the substrate and  $t_s$  and  $t_f$  are the thicknesses of the substrate and film respectively. The film stress measured is the total stress due to thermal mismatch and its intrinsic

components. The intrinsic stress can then be derived from this measurement and the known thermal mismatch stress from the previous relationship.

Even though high stresses can result from the sum of thermal mismatch and intrinsic stress in a film, if the film is uniformly planar then the stress resulting in the substrate due to the film will be orders of magnitude smaller. This is due to the large difference in thicknesses between the film ( $t_f$ ) and the substrate ( $t_s$ ):

$$\sigma_s = -4\sigma_f \frac{t_f}{t_s}. \quad (2-23)$$

Higher local stresses result in the substrate due to discontinuities in the film. Such discontinuities include etched film edges from masking and nonplanarities as in trench fill depositions.

Film-induced Strain Model. The stress due to deposited films is modeled as an initial condition before deformation. The planar measurements of intrinsic stress are used as the initial condition for the finite element solution. The stresses are input at the nodes as the film is deposited. They are directed in a biaxial tangential orientation along the growing interface as is shown in Figure 2-6. To handle the stress components in nonplanar interfaces, the stresses are translated from the planar system axis to the axis perpendicular to the normal of the growing film. After the film is deposited or grown, the stresses at the nodes are then averaged to their neighboring triangular (2D) or tetrahedral (3D) elements.



The thermal mismatch stress is modeled as a hydrostatic stress. Each normal component of strain exerted is equal in magnitude. No shear components result from thermal mismatch. For each element in the film, the three normal components of strain are added by superposition to the previous state of stress due to other sources. This presents a problem in plane strain FEM formulations since the strain in one direction is set to zero. This problem will be addressed in section 2.3.

### 2.2.2 Dopant Induced Stress

As dopants are introduced to the silicon substrate, the mechanical state of the substrate will change. The dopants may substitute for the silicon positions in the lattice. Silicon atoms are displaced forming extended defects that are lodged in the crystal lattice. Different dopants have varying atomic sizes and therefore have different mechanical behavior in the crystal. Precipitates and other atoms present such as oxygen and carbon also alter the mechanical properties of the crystal.

Boron. Boron is well known as a substitutional dopant. Its atomic size is smaller than that of silicon. When it locates into a substitutional site, lattice contraction results due to its smaller size. This presents an atomically localized strain in the crystal due to each boron atom. Figure 2-7 exemplifies this in three- and two-dimensional illustrations. For high concentrations of boron in silicon, these atomic strains add up significantly and result in a larger localized region of strain in the boron doped silicon lattice. The non-

boron doped silicon region will resist the diffused boron layer from contracting and thus result in a tensile strain field. This effect has been demonstrated in silicon micro-machining applications [8, 39, 40], where boron-doped cantilevers have exhibited bending due to strain induced by the boron.

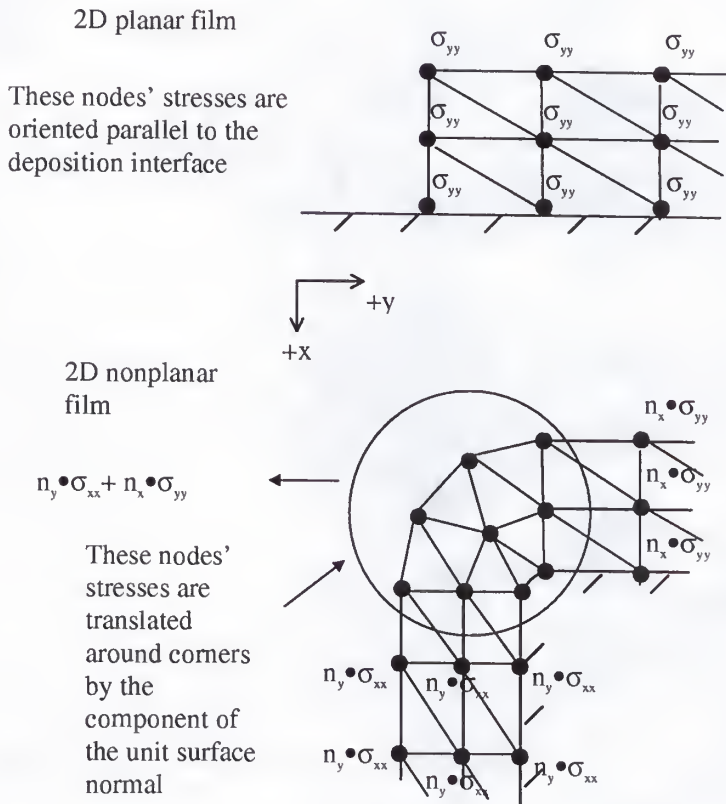


Figure 2-6 Intrinsic film stresses are oriented parallel to the interface on which the film is grown or deposited.



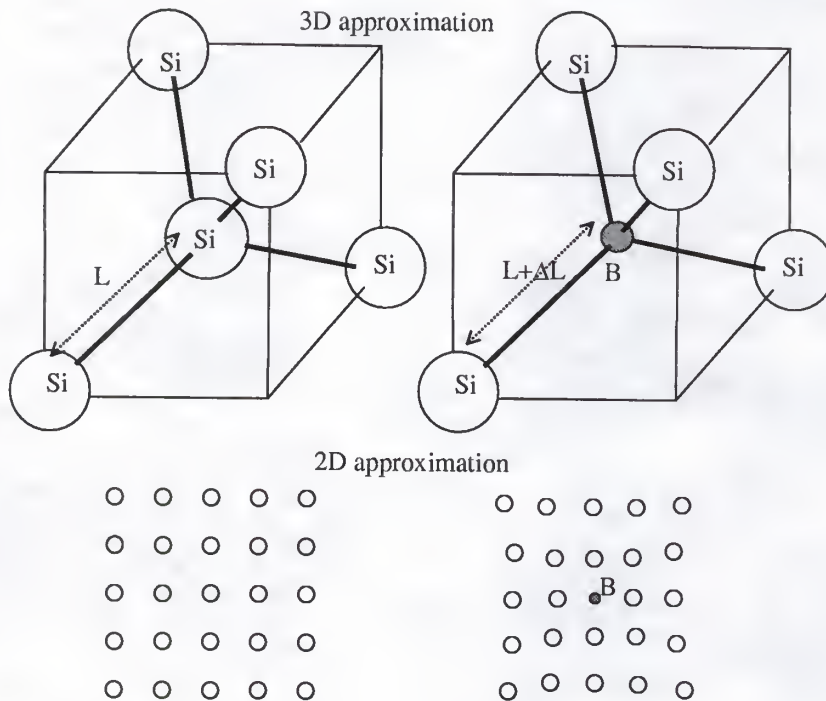


Figure 2-7 Two- and three-dimensional illustrations of lattice deformation due to boron substitution.

Densitometric studies have been done with boron doped silicon crystals. Horn measured the silicon lattice constant variation as a function of boron concentration [41]. From his measurements, the induced strain ( $\Delta a/a$ ) was extracted and given as function of boron concentration (Figure 2-8).

Boron-induced Strain Model. The empirical relationship introduced by Horn is used as the contribution of strain in silicon due to substitutional boron dopant. According to his measurements, 0.0141 Å of lattice contraction

results per percentage of B in Si at room temperature. Using this figure, the following relationship is derived:

$$\varepsilon_{xx} = \varepsilon_{yy} = \varepsilon_{zz} = \frac{\Delta a}{a_{Si}} = \frac{0.0141}{a_{Si}} \cdot \frac{C_B}{N_{Si}} \cdot 100 \quad (2-24)$$

where  $a_{Si}$  is the silicon lattice constant (5.4295Å at 25°C) and  $N_{Si}$  is the density of Si atoms ( $5.02 \times 10^{22} \text{ cm}^{-3}$ ). The average concentration of Boron ( $C_B$ ) is computed for each element from its node quantities. Dopant-induced strain is also hydrostatic (as in thermal mismatch strain) and again presents a problem in plane strain FEM formulations since the strain in one direction is set to zero. This problem will be addressed in section 2.3.

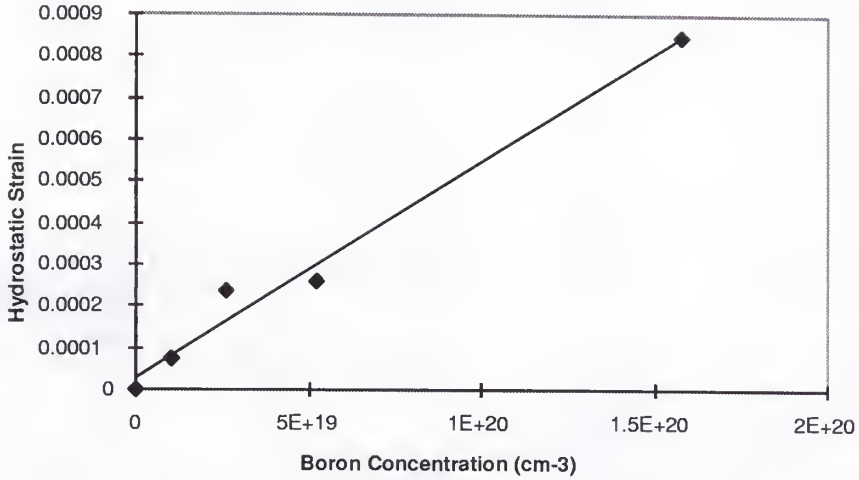


Figure 2-8 Hydrostatic strain as a linear function of boron concentration [41]

Other dopants. The strain contributions of other common dopants such as phosphorus and arsenic are not as great per atom as that due to boron. Because arsenic has a much larger atomic mass than silicon, one would tend to believe that arsenic would induce a large compressive strain in the silicon lattice. However, it has been reported that heavily doped arsenic ( $5 \times 10^{21} \text{ cm}^{-3}$ ) only induces a lattice compression ( $\Delta a/a_{\text{Si}}$ ) of approximately 0.0019 [42]. The atomic size of phosphorus is more closely matched to that of silicon and therefore the P-Si bond lengths are of the same magnitude as the Si-Si bond lengths.

### 2.2.3 Oxidation Volume Expansion

The oxidation process also induces strain in the substrate due to the net volume expansion of the oxidation reaction. It is well known that silicon oxidizes to a volume of oxide that is 2.2 times larger. For planar oxidation, this presents no problem since the newly acquired volume pushes the old oxide upward towards the unconstrained surface perpendicular to the interface. However, in nonplanar regions such as in trench corners and in constrained regions such as in LOCOS edges, this presents a problem. For these regions, the boundaries are constrained and therefore the newly acquired oxide volume compresses against the earlier grown oxide. Since the oxide has no place to move, large compressive strains build up in these regions. The strains are somewhat relaxed by applying pressure to the silicon

interface. The forces applied to the silicon are high enough to surpass the yield stress of silicon.

### 2.3 Strain Computation Methods

Two different finite element based methods are developed to solve and compute the previously described models of the various strain sources. These algorithms are developed in the process simulator FLOOPS [43] and are integrated with and derived from methods developed to model stress-dependent oxidation and silicidation [44].

Newton's second law of motion governing deformation is stated as the following [30]

$$\rho a_i = \frac{\partial \sigma_{ij}}{\partial x_j} + b_i \quad (2-25)$$

where  $\rho$  is the density of the body,  $a_i$  is the acceleration,  $\sigma_{ij}$  is the local stress tensor, and  $b_i$  is the body force.

The equivalent nodal force for each element ( $q^e$ ) may be represented as the following:

$$q^e = \int_{V^e} B^T \sigma \partial(vol) - \int_{V^e} N^T b \partial(vol) \quad (2-26)$$

where  $b$  represents local body forces (e.g. gravitational or electromagnetic forces), the  $B$  matrix relates the strain rate to the displacement rate (velocity) of element and  $N$  represents the shape functions of the element. This

statement is valid quite generally for any stress-strain relationships. The assumption of negligible body forces and negligible acceleration for each element allow the equivalent nodal force equation to reduce to the following:

$$q^e = \int_{V^e} B^T \sigma \partial(vol). \quad (2-27)$$

For mechanical equilibrium where the body is not under rigid body motion, net force is equal to zero.

An Hookean elastic element with the following constitutive relation

$$\sigma = D(\epsilon - \epsilon_0) + \sigma_0 \quad (2-28)$$

would be modeled by substituting the constitutive relation into the equivalent nodal forces equation:

$$q^e = \left[ \int_{V^e} B^T D \epsilon \partial(vol) \right] - \int_{V^e} B^T D \epsilon_0 \partial(vol) + \int_{V^e} B^T \sigma_0 \partial(vol). \quad (2-29)$$

The strain  $\epsilon$  is related to the unknown displacement  $\Delta a$  through the B matrix

$$\epsilon = B \Delta a^e \quad (2-30)$$

and may also be substituted into the elastic equivalent nodal force equation:

$$q^e = \left[ \int_{V^e} B^T D B \partial(vol) \right] \Delta a^e - \int_{V^e} B^T D \epsilon_0 \partial(vol) + \int_{V^e} B^T \sigma_0 \partial(vol). \quad (2-31)$$

Under mechanical equilibrium, the elastic equivalent nodal force equation reduces to the following discretized form:

$$[B^T D B \Delta] \Delta a^e = B^T D \epsilon_0 \Delta - B^T \sigma_0 \Delta \quad (2-32)$$



where  $\Delta$  is the area (volume in 3D) of the element. The left-hand side represents the stiffness matrix of the element. The right hand side represents the initial stress and strain state of the element. From this relation, the displacement  $\Delta a$  is solved for globally and the current stress and strain state can be derived from the displacement  $\Delta a$ .

A viscoelastic body is handled in the same manner. The Maxwell viscoelastic constitutive relation

$$\frac{\dot{\sigma}}{G} + \frac{\sigma}{\eta} = \dot{\epsilon} \quad (2-33)$$

has the following solution for the stress  $\sigma$ :

$$\sigma = \eta \left[ 1 - \exp\left(\frac{-\Delta t}{\tau}\right) \right] \dot{\epsilon} + \sigma_0 \exp\left(\frac{-\Delta t}{\tau}\right) \quad (2-34)$$

where  $\tau$  is the relaxation time constant and is the ratio of the viscosity  $\eta$  to the elastic modulus  $G$

$$\tau = \frac{\eta}{G}. \quad (2-35)$$

The Maxwellian viscoelastic constitutive relation can then be substituted into the equivalent nodal force equation:

$$q^e = \left[ \int_{v^e} B^T \left\{ \eta \left[ 1 - \exp\left(\frac{-\Delta t}{\tau}\right) \right] \right\} D \dot{\epsilon} \partial(vol) \right] + \int_{v^e} B^T \sigma_0 \exp\left(\frac{-\Delta t}{\tau}\right) \partial(vol). \quad (2-36)$$

The strain rate  $\dot{\epsilon}$  is related to the unknown change in velocity  $\Delta v$  through the  $B$  matrix



$$\dot{\epsilon} = B\Delta v^e \quad (2-37)$$

and may also be substituted into the viscoelastic equivalent nodal force equation:

$$q^e = \left[ \int_{v^e} B^T \left\{ \eta \left[ 1 - \exp\left(\frac{-\Delta t}{\tau}\right) \right] \right\} DB \partial(vol) \right] \Delta v^e + \int_{v^e} B^T \sigma_0 \exp\left(\frac{-\Delta t}{\tau}\right) \partial(vol). \quad (2-38)$$

Under mechanical equilibrium, the viscoelastic equivalent nodal force equation reduces to the following discretized form:

$$\left[ B^T \left\{ \eta \left[ 1 - \exp\left(\frac{-\Delta t}{\tau}\right) \right] \right\} DB \Delta \right] \Delta v^e = -B^T \sigma_0 \exp\left(\frac{-\Delta t}{\tau}\right) \Delta \quad (2-39)$$

where  $\Delta$  is the area (volume in 3D) of the element. The left-hand side represents the stiffness matrix of the element. The right-hand side represents the initial stress and strain state of the element. From this relation, the unknown change in velocity  $\Delta v$  is solved for globally and the current stress and strain rate can then be derived from the new velocity change  $\Delta v$ .

The viscoelastic formulation reduces to the elastic formulation for large relaxation time constant  $\tau$ . If  $\tau \gg \Delta t$ , then

$$\exp\left(\frac{-\Delta t}{\tau}\right) = 1 - \frac{\Delta t}{\tau}. \quad (2-40)$$

The viscoelastic formulation then becomes

$$\left[ B^T \left\{ \eta \frac{\Delta t}{\tau} \right\} DB \Delta \right] \Delta v^e = -B^T \sigma_0 \left( 1 - \frac{\Delta t}{\tau} \right) \Delta \quad (2-41)$$

and reduces to the elastic formulation by allowing  $\Delta t \Delta v^e = \Delta \alpha^e$ .

To model two-dimensional problems, the plane strain formulation is used. This formulation can be used for problems where the strain component in the  $z$ -direction is zero or negligible [28]:

$$\varepsilon_{zz} = \varepsilon_{zx} = \varepsilon_{yz} = 0. \quad (2-42)$$

This can be approximated solving problems with infinitely long dimensions in the  $z$ -direction. Therefore, the strain in the  $z$ -direction will approach zero. As was mentioned before in the earlier sections, a problem arises using the plane strain approximation while computing thermal mismatch and dopant induced stress. These sources include a hydrostatic strain field  $\varepsilon_0$  described as the following:

$$\varepsilon_0 = \begin{bmatrix} \varepsilon_{xx} \\ \varepsilon_{yy} \\ \varepsilon_{zz} \end{bmatrix} = \begin{bmatrix} \varepsilon \\ \varepsilon \\ \varepsilon \end{bmatrix}. \quad (2-43)$$

Then plane strain presumption implies that stresses in the  $z$ -direction will still occur even if there is no  $z$ -component of strain. These stresses occur due to dopant and thermal expansion and are affected by the elastic constants. To account for this using a plane strain approximation, the following expression is used instead for an elastic relationship [28]:

$$\varepsilon_0 = \begin{bmatrix} \varepsilon_{xx} \\ \varepsilon_{yy} \\ \varepsilon_{zz} \end{bmatrix} = (1 + \nu) \begin{bmatrix} \varepsilon \\ \varepsilon \\ 0 \end{bmatrix} \quad (2-44)$$

where  $\nu$  is the Poisson's ratio.

The FEM formulation uses three noded triangular elements called 'faces' for two-dimensional applications and four noded tetrahedral elements called 'volumes' for three-dimensional applications. Linear shape functions are used for interpolation of the strain solution within each element.

Reflecting boundary conditions are used to handle the strain solution at the boundary of the simulation field. The normal component of the velocity field or displacement rate is set to zero across this interface. Physically this corresponds to a 'mirror reflected' symmetrical structure across the boundary.

### 2.3.1 Boundary Loading Method

The boundary loading method (BL) uses the strain solution calculated during the oxidation to drive the elastic solution in the silicon. This technique has been used in the SUPREM IV process simulator to calculate the elastic strain in silicon due to oxidation [2]. Chidambarrao also used this technique to investigate strains resulting from isolation trenches [45]. It is fully decoupled and is performed in two sequential steps. This is demonstrated in Figure 2-9. In the first step, the nonlinear viscoelastic oxide flow is computed with the surface films modeled as viscoelastic materials and with silicon acting as a rigid body [44]. This assumption allows for a more efficient technique for solving the oxide growth, since only the surface films are iterated over in the nonlinear stress dependent oxidation solution.

The stress tensor in the silicon dioxide elements along the silicon - silicon dioxide interface are averaged to interface nodes. The averaged node

Step 1- Calculate the stress in the upper surface films to compute the stress-dependent oxidation growth



Step 2- Calculate the stress induced in the substrate due to the forces generated during oxidation and strain generated from dopants.

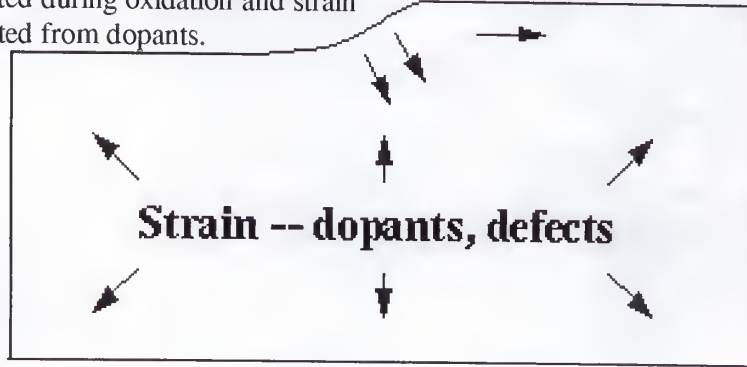


Figure 2-9 The boundary loading method is composed of two separate steps for computing the strain in silicon.

stresses are then converted into boundary forces along the interface. The boundary forces are simply the product of the stress tensor with the unit surface normal of each node:

$$\begin{bmatrix} F_x \\ F_y \\ F_z \end{bmatrix} = \begin{bmatrix} \sigma_{xx} & \sigma_{xy} & \sigma_{zx} \\ \sigma_{xy} & \sigma_{yy} & \sigma_{yz} \\ \sigma_{zx} & \sigma_{yz} & \sigma_{zz} \end{bmatrix} \cdot \begin{bmatrix} \hat{n}_x \\ \hat{n}_y \\ \hat{n}_z \end{bmatrix} \quad (2-45)$$

These forces are then input as boundary loading forces that drive the calculation of the elastic substrate strain solution. Silicon is modeled as an



isotropic elastic material in the second step. Strain may be included that is exerted from dopants and defects within the silicon for this solution.

### 2.3.2 Fully-Integrated Method

The other technique developed to investigate the strain in silicon is similar to the finite element method implemented by Senez [46]. This fully-integrated method couples the strain solution in the silicon along with the surface films to compute the oxidation growth. This method allows for the oxide stresses to relax by exerting forces on the silicon substrate. In the BL method, oxide stresses can't relax due to the rigid body boundary condition imposed on the silicon. Therefore, lower magnitudes of stresses are expected in using this method. This method is extended to include strains from other sources simultaneously (Figure 2-10).

This technique becomes very computationally intensive because the silicon elements are also assembled into the nonlinear oxidation equation. This usually results in an order of magnitude more elements included to adequately define the substrate and reduce the effect of the reflecting boundaries on the solution. Therefore, the FI method's Newton iteration involves a much larger matrix than the BL method and results in much slower performance overall.

As in the previously described method, the surface films are modeled as viscoelastic bodies and the silicon substrate is modeled as an isotropic elastic material. The boundary condition at the oxidant reaction interface is

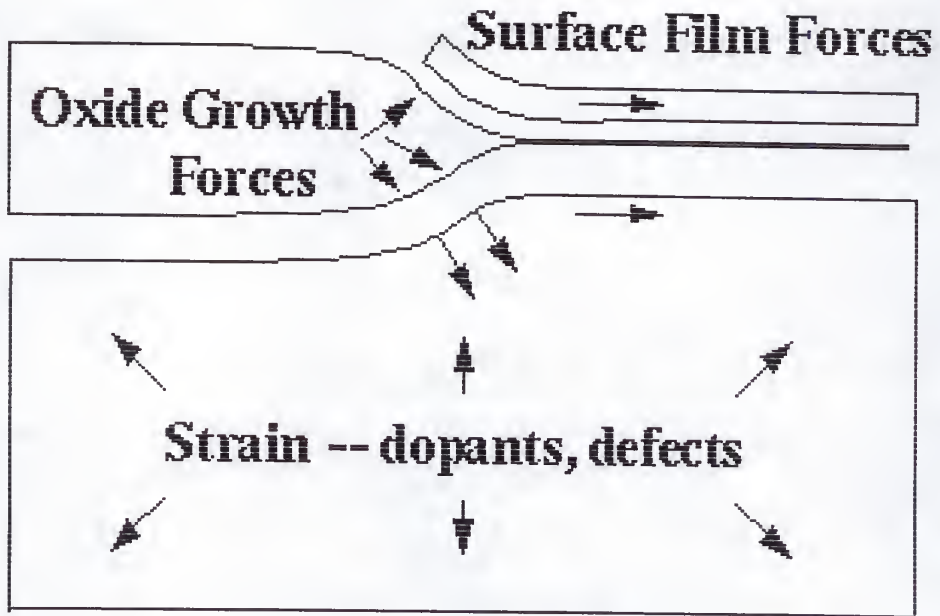


Figure 2-10 The fully integrated method couples the solutions of strain in the upper films along with the substrate simultaneously.

similar to a polysilicon boundary condition: the silicon flows and is consumed. Additionally, strain from dopants and intrinsic film stress may be exerted in the silicon substrate and also is included as a stress source in this method.

## 2.4 Summary

One of the goals of this work are to develop a system where strain can be computed from multiple sources independently and simultaneously. In this chapter, a brief review of continuum mechanics was first provided to refresh the reader with the necessary terminology. Next the individual strain sources and the algorithms used to model the mechanical strain generated



from each source were described. Finally the boundary loading (BL) and fully-integrated (FI) finite element were introduced and discussed for modeling the strain due to oxidation volume dilation. The optimized BL method enforces a rigid body assumption for silicon. This allows it to be useful for analyzing oxidation-induced strains in three-dimensions, as will be discussed in the chapter three. However, this assumption may produce influences in the oxide growth and stress solutions. Therefore, in chapter three, the two methods will be analyzed for several applications to find if and when there are influences. Also, in chapter three, applications using the film-induced and boron-induced strain models are demonstrated and they are compared and validated with experimental studies.

## CHAPTER 3

### APPLICATION EXAMPLES AND COMPARISONS

Due to the fully integrated method's computational intensiveness, the boundary loading method is more commonly used. This brings into question how well the solution from each method agrees. Comparisons are performed between each method for computing the oxidation-induced stresses for different processes in silicon fabrication. Next, solutions of nitride film-induced stresses are compared with micro-Raman spectroscopy investigations. Afterwards, boron-induced cantilever bending simulations are performed and compared with previous experiments. Finally, a three-dimensional example is demonstrated for simulating oxidation-induced stress using the boundary loading method.

#### 3.1 FEM Comparisons

To compare the two methods for computing oxidation-induced stress, two different oxidation processes are analyzed. The first is a standard LOCOS process. The second is a re-oxidation process over an oxide filled shallow trench. These examples detail when the boundary loading method

solutions fail to match the solutions computed by the fully-integrated method.

Each of the following simulations is two-dimensional and use the plane strain approximation with reflecting boundary conditions. This means that the dimensions in the z-direction (which extends outward perpendicular to the plane of the page) are infinitely long. The reflecting boundary conditions indicate that the structure is periodic along the right and left boundaries of the field.

Hydrostatic pressure contours are plotted for each process to compare solutions computed by each method. This allows for a scalar interpretation of the stress tensor's variation in the two-dimensional field. The hydrostatic pressure definition used is simply the negative average of the normal components or negative one-third of the trace of the stress tensor:

$$P = -\frac{1}{3} \begin{bmatrix} \sigma_{xx} & 0 & 0 \\ 0 & \sigma_{yy} & 0 \\ 0 & 0 & \sigma_{zz} \end{bmatrix}. \quad (3-1)$$

For each wet ambient simulation, material properties calibrated at 1000°C by Cea and Senez [44, 46] are utilized. These parameters are listed in Table 3-1.

For the STI simulations where dry oxidations are also performed, the oxide material properties were calibrated to Kao's dry oxidation cylinder

Table 3-1 Material coefficients at 1000°C [44, 46]

material	Elastic Parameters		Viscosity Parameters	
	Elastic Modulus (Dyn/cm <sup>2</sup> )	Poisson's Ratio	Viscosity (Dyn/cm <sup>2</sup> )	V <sub>0</sub>
oxide	6.6e11	0.17	2.0e14	450e-24
nitride	3.89e12	0.3	7.0e14	100e-24
silicon	1.7e12	0.3	-	-

experiments [13], similarly to how the wet oxidation parameters were calibrated [44].

In Kao's experiment, cylinders and holes of varying radii were oxidized to grow approximately 3500Å at various temperatures in a dry ambient. In both the cylinders and holes the oxide growth was retarded when compared to plane wafer oxide growth. It was concluded that this decrease in oxide growth was due to the stress dependence on the diffusivity of oxidant reactant, reaction rate, and viscosity of oxide. As the radii of the cylinders and holes decrease, the amount of oxide growth also decreases. A standard calibration procedure adopted by Rafferty [2] and Cea [44] is used to obtain the oxide parameters that fit the curves for each temperature and radius geometry. The results of the cylinder and hole simulations are plotted in Figure 3-1. The dry oxide parameters obtained from the calibration simulations are listed in Table 3-2 along with the wet oxide parameters obtained by Cea [44].

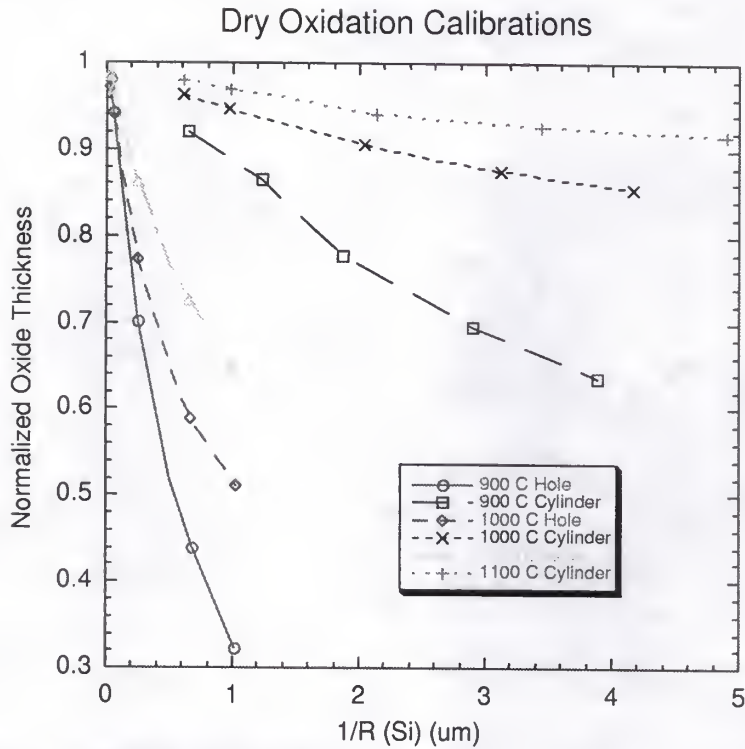


Figure 3-1 Results of dry oxidation calibrations for holes and cylinders calibrated to Kao's measurements [13]

The calibrated low stress viscosity of dry oxide is plotted over temperature in Figure 3-2 along with the wet oxide viscosities calibrated by Cea [44]. It can be seen that the dry oxide low stress viscosities are about an order of magnitude less than the corresponding viscosity at each temperature. This is expected since dry oxidations produce a denser oxide. Also, the viscosities follow along the same slope in the Arrhenous plot with similar activation energies.



Table 3-2 Calibrated dry and wet [44] oxide parameters.

T(C)	Oxide Viscosity Parameters		Diffusivity and Reaction Rate Parameters	
	$\eta_0$ (dyn/cm <sup>2</sup> )	$V_0$ (Å <sup>3</sup> )	$V_D$ (Å <sup>3</sup> )	$V_K$ (Å <sup>3</sup> )
1100 W	3.3e13	1100	75	10
1000 W	2.0e14	450	"	"
900 W	1.5e15	300	"	"
1100 D	3.5e14	250	"	"
1000 D	2.2e15	150	"	"
900 D	2.5e16	6.25	"	"

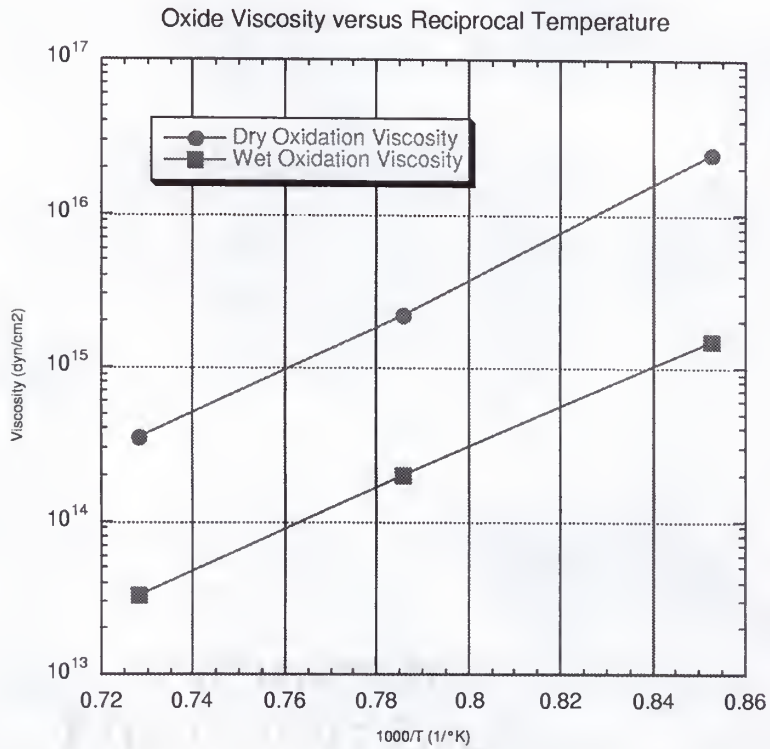


Figure 3-2 Calibrated dry oxide viscosity compared with the wet oxide viscosity calibrated by Cea [44].



### 3.1.1 LOCOS

The LOCOS process is simulated to compare between two-dimensional stress solutions computed by each method. Figure 3-3 exemplifies simulations of a 1000°C eighty-minute wet oxidation process at atmospheric pressure. A 180nm thick nitride film with a two-micron linewidth is patterned over a 20nm thick pad oxide. The grid spacing used for the simulations is 0.05 $\mu$ m at nitride edge, 0.15 $\mu$ m at the left and right side boundaries, and 0.25 $\mu$ m at the bottom boundary.

Figure 3-3 displays the stress solution for each method. By analyzing the average pressure contours displayed, it is observed that there is qualitative agreement between the two methods for this particular LOCOS process and geometry. Corresponding regions are in tension (negative pressure) and in compression (positive pressure). However the relative areas occupied by the corresponding pressure contours indicate that their magnitudes disagree. This is expected since the fully integrated method allows for some stress relaxation through a 'flexible' silicon base. The boundary loading method does not allow oxide stress relaxation through the silicon because the silicon is modeled as a rigid body. The presence of both compressive and tensile regions in the silicon is due to its elastic behavior. When a compressive force is applied to an elastic body (such as at the bird's beak in silicon), a neighboring region in the material tends to deform in tension due to the Poisson's ratio effect.

The solutions in the oxide agree more closely in magnitude than in the silicon. It is for this reason that the bird's beak heights (BBH) are almost identical as can be seen in Figure 3-4. This indicates that the rigid body boundary condition used for computing the oxide growth, as modeled in [44], does not affect the oxide stress solution enough to alter the oxide growth significantly at longer nitride linewidths. However at shorter linewidths, it becomes evident that the BB curvature underneath the nitride edge is influenced by the strain computing method. In Figure 3-4, an overlay of simulations using both strain computing methods is shown. The FI method solution shows a little more oxidation under the nitride edge. This indicates that the BL method computed a higher stress in this region that retarded the oxide growth. A matrix of LOCOS simulations is performed to analyze the differences of the stress and oxide growth solutions for shorter nitride linewidth simulations using each FEM method.

Table 3-3 represents a matrix of simulations with varying nitride linewidths. The first set with linewidth of  $2\mu\text{m}$  is demonstrated in Figure 3-3. Depending on the amount of elements in the field, the boundary loading method is about two to three times faster than the fully integrated method. Table 3-3 demonstrates that the oxide thickness and BBH is consistent between the two methods and the variation in oxide shape is small until the nitride linewidth decreases to  $0.5\mu\text{m}$ . Below this linewidth, the oxide punch-through effect begins to occur and the BBH varies more significantly

depending on the strain computing method used. The maximum tensile and compressive stress magnitudes in the silicon are also noted for each simulation and tend agree.

Table 3-3 Matrix of LOCOS simulations depicting how the two FEM solutions correlate with decreasing nitride linewidth.

linewidth ( $\mu\text{m}$ )		BBH ( $\mu\text{m}$ )	Max Oxide Growth ( $\mu\text{m}$ )	Max Tension	Max Compression	CPU time (s)
2.0	FI	0.276	0.499	-1.5e9	4.9e9	1077.4
	BL	0.268	0.499	-3e9	5e9	633.9
1.0	FI	0.233	0.453	-3.7e9	7.5e9	1638.5
	BL	0.235	0.46	-3.4e9	5.1e9	552.5
0.7	FI	0.215	0.415	-6.5e9	6.9e9	895.6
	BL	0.215	0.42	-8e9	5e9	343.0
0.5	FI	0.179	0.367	-5e8	8e9	821.6
	BL	0.190	0.368	-5e8	8e9	300.2

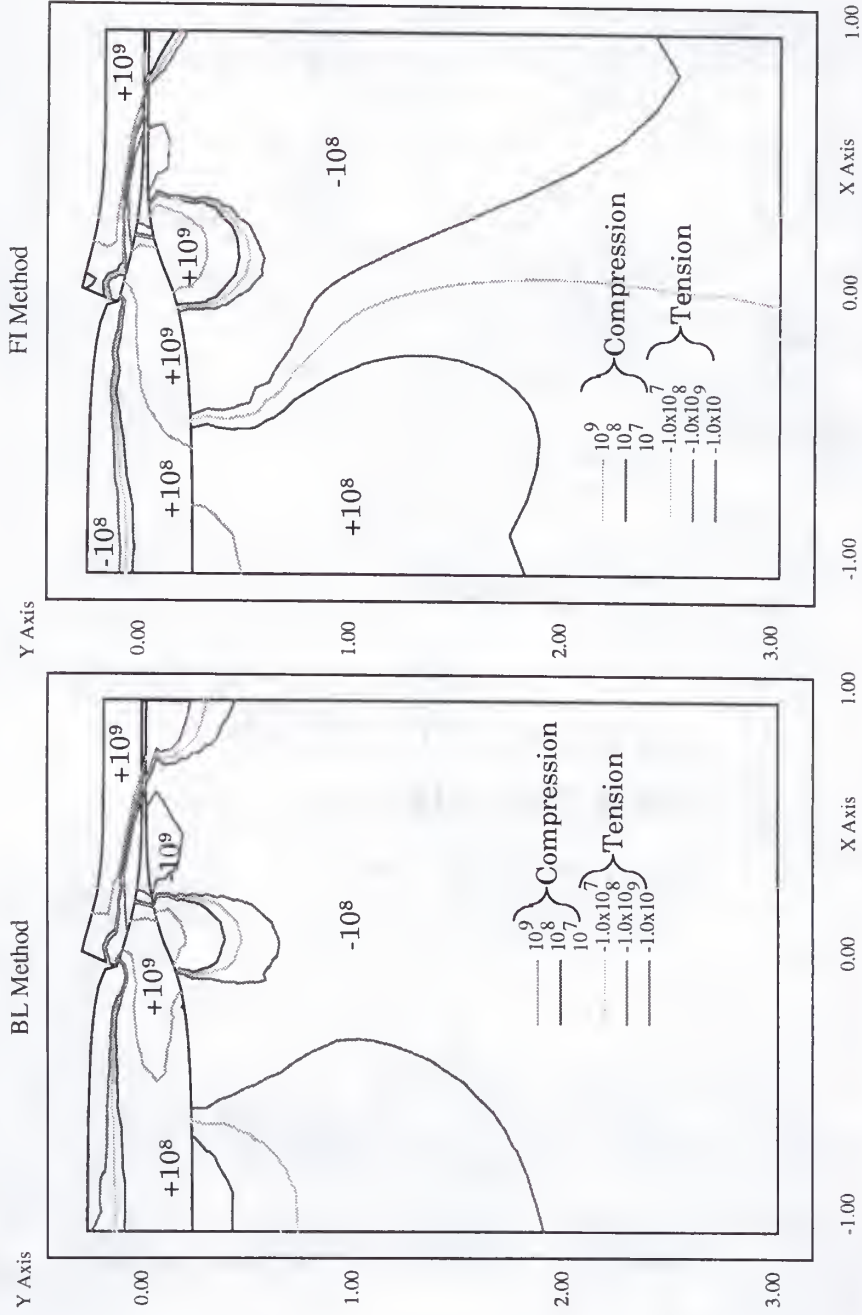


Figure 3-3 Comparisons for a LOCOS-induced stress computed by the boundary loading method (left) and the fully-integrated method (right).

x in microns

## Oxide Shape Comparisons

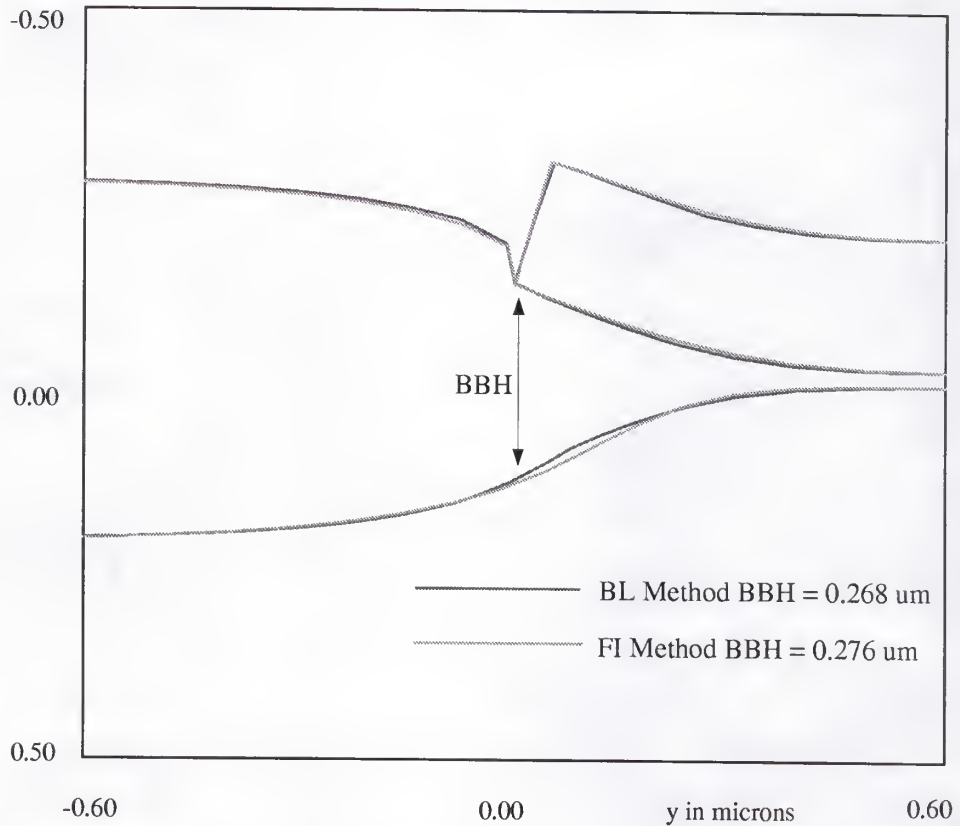


Figure 3-4 Overlaying oxide shape solutions comparisons between the BL method and FI method for an example LOCOS simulation with 2 $\mu$ m nitride linewidth.

### 3.1.2 Post-STI Process Re-Oxidation

Strain Solution Comparisons. An oxidation process over a previously processed oxide filled shallow trench isolation (STI) is simulated to compare between two-dimensional stress solutions computed by each method. Figure 3-5 exemplifies a simulation of a 1000°C three-minute wet oxidation at atmospheric pressure. The trench with 0.5 $\mu$ m depth and 0.5 $\mu$ m width is filled



with deposited oxide. The nitride mask in this simulation has been previously stripped as in a CMP process. The grid spacing used for the simulation is  $0.02\mu\text{m}$  at the trench edges,  $0.20\mu\text{m}$  at the left and right side boundaries, and  $0.10\mu\text{m}$  at the bottom boundary. The initial field stress solution is set to zero to compare the stress induced by the oxidation alone.

Figure 3-5 is an example of a 'wedge driving effect' that is an oxidation performed over a fabricated trench that is not masked. A vertical bird's beak forms at the upper corners of the trench due to reactant diffusion into the trench. This produces a very high compressive stress in the silicon substrate along the side of the trench as oxide is grown on the trench sidewall. Therefore this is analogous to a wedge being driven in at the trench sidewall.

By observing the average pressure contours displayed, it is observed that there is qualitative agreement between the two methods for this process. The tensile and compressive regions again correspond between the two method's solutions. The relative areas occupied by the corresponding pressure contours indicate that their intensity variations disagree. The BL method computes that the entire field is in compression with the exception of the silicon at the bottom trench corner. Therefore, the two methods agree qualitatively in the strain solution computed for this process. However, for STI re-oxidation processes the strain solution is only part of the concern.

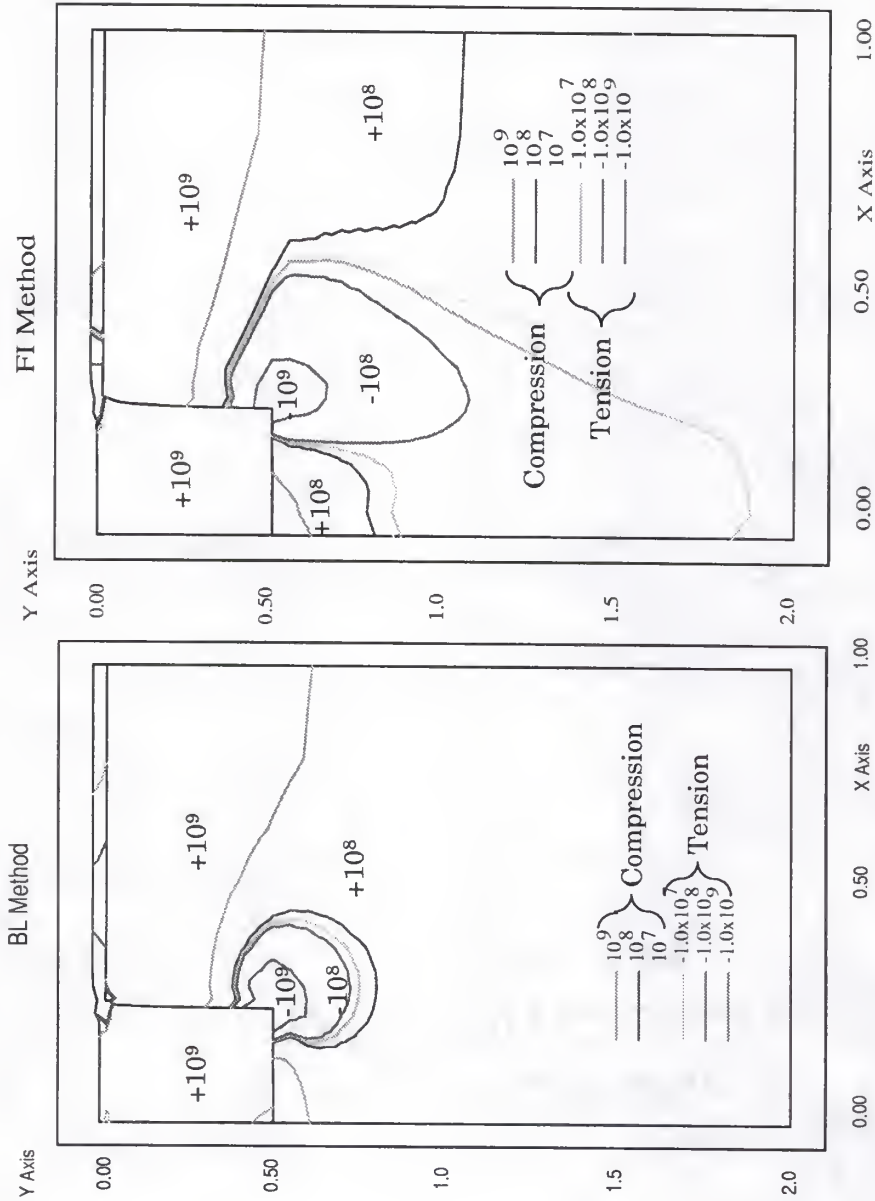


Figure 3-5 Comparisons for post STI process-induced stress computed by the boundary loading method (left) and the fully-integrated method (right).

Corner Rounding Comparisons. One of the most critical design aspects of the STI is the top corner shape. It is desirable for the top corners to be rounded for several reasons. The most important being that sharp corners lead to high electric fields and result in undesirable electrical characteristics [47, 48]. Another reason for avoiding sharp corners is they lead to higher mechanical stress magnitudes that generate dislocations also deleterious to device operation [7].

Re-oxidation after fabrication of the STI has been introduced as a method to round the upper trench corners [48]. The increased radius of curvature at the upper corners alleviates these problems. Selecting the most appropriate oxidation process for this technique can be simplified through oxidation process simulation [49].

Viscoelastic flow models are used for the grown and deposited films during the re-oxidation process [44]. Stress-dependent models for oxide viscosity, reaction rate, and diffusivity are utilized for simulating the re-oxidation anneals. Two-dimensional plane strain simulations are performed for a re-oxidation process to study the evolution of the radius of curvature of the upper STI corners. The re-oxidation occurs after the planarization step of the STI process. Therefore the oxide fills the trench up to the surface of the nitride film (Figure 3-6). The STI dimensions have a depth of 300nm and a width of 400nm. A series of re-oxidation simulations is performed varying the nitride thickness from 70nm to 180nm over a 30nm pad oxide. The re-

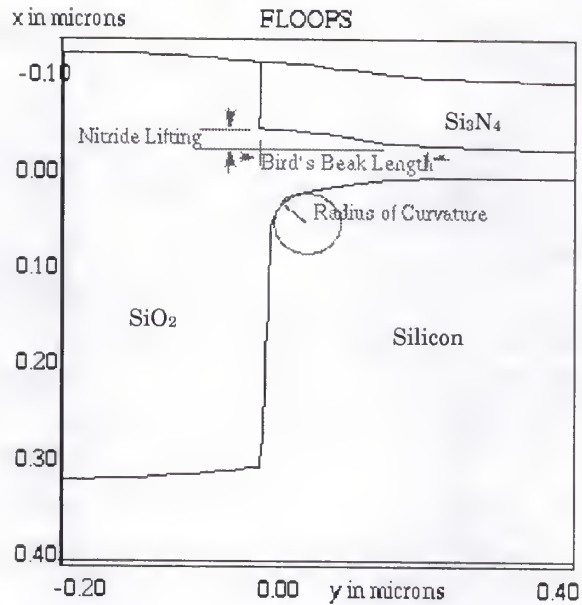


Figure 3-6 1000°C 300 minute dry re-oxidation simulation.

oxidation processes simulated and analyzed are a 300 minute 1000°C dry anneal, 100 minute 1100°C dry anneal, and a 30 minute 950°C wet anneal. The oxidation processes result in about 150nm of oxide grown on a blank wafer. Each process is examined for each of the nitride film thicknesses.

The radius of curvature relationship to nitride thickness is consistent with the experimental results of Chang [48] (Figure 3-7). The amount of nitride lifting also varies linearly with the nitride thickness. The bird's beak lengths are fairly constant over this range so there is little trade-off against the thinner nitride process.

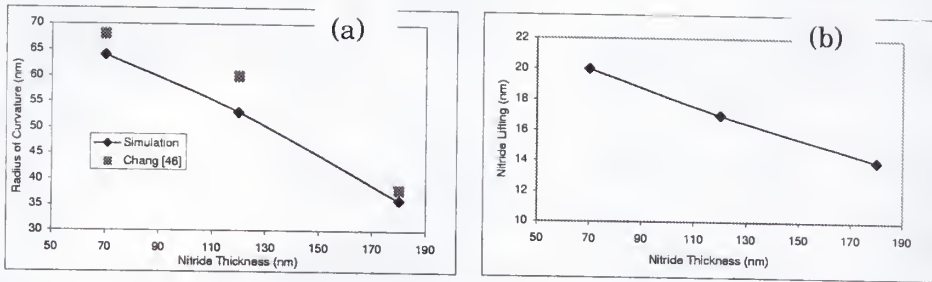


Figure 3-7 (a) The radius of curvature of the upper STI corner and (b) nitride lifting at the bird's beak increases with decreasing nitride mask thickness for the 1100°C dry oxidation.

Figure 3-8 depicts how the various process simulations examined resulted for a given nitride thickness using each oxidation strain computation method. It can be seen that for the higher temperature 1100°C dry oxidation resulted in the greatest amount of corner rounding and stress relaxation.

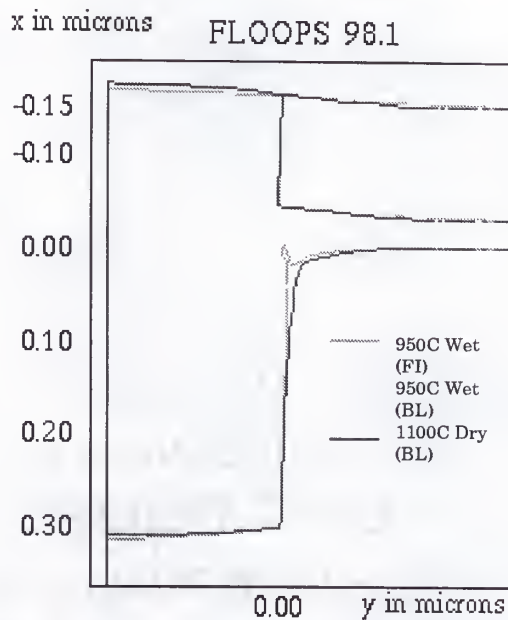


Figure 3-8 Overlay of the re-oxidation profiles for each anneal process with 120nm nitride film thickness.



Also, due to less stress relaxation in the lower temperature 950°C wet oxidation, less corner rounding is resulted by the BL method and an overhang results by the FI method. The overhang also agrees with re-oxidation experiments [48]. However its shape is different since the simulated shape may be locally grid dependent. The higher stresses reduce the oxidation rate at the upper silicon corner just below the nitride edge and result in excessive compressive stress magnitudes in the neighboring silicon region.

From this application, it is found that for the low temperature wet re-oxidation simulations, the FI method results in an overhang at the trench corner due to the severe oxide growth retardation. However for the same simulation, the BL method returns a rounded corner. Since in experiment [48], this process does result in a slight overhang, it is believed that including the silicon deformation while calculating the oxide growth plays an important role in modeling this effect at the trench corner.

### 3.2 Raman Spectroscopy Measurements and Comparisons

In the previous section qualitative comparisons were performed for different oxidation processes between the two FEM methods implemented. In this section, efforts are made to compare the nitride film edge-induced stress with measured strain data. Currently, the best method for measuring local

process-induced mechanical strains in the substrate at sub-micron dimensions is micro-Raman spectroscopy [26].

Raman spectroscopy is most commonly utilized for crystallographic and chemical composition analysis. Mechanical strain or stress affects the frequencies of the Raman modes of the crystal. The Raman spectrum of the silicon crystal is sensitive to strain in the lattice and therefore has been used to measure the stress state induced by microelectronics fabrication processes [50]. Micro-Raman stress measurements involve focusing laser light onto a sample. The scattered light of the sample is then collected and analyzed. The light scattered from a (100) unstressed silicon sample has a Raman peak frequency of about  $520 \text{ Rcm}^{-1}$ . Stressed samples will influence a shift in the Raman peak. The amount and direction of the shift corresponds to the magnitude and sign (compressive or tensile) of the stress in the laser spot region of the sample. A negative shift corresponds to a tensile stress and a positive shift indicates a compressive stress.

### 3.2.1 Raman Simulation Method

A method for determining the expected frequency shift in Raman modes due to process-induced strain was introduced by Jones [51] and De Wolf [52]. This method is implemented here to validate the stress solution from the nitride film edge-induced stress model with micro-Raman measurement data. The method involves first evaluating the shift in Raman

modes for a given strain tensor solution. For an elastic material, the strain tensor is related to the stress tensor through the compliance tensor  $s_{ijkl}$ :

$$\epsilon_{ij} = s_{ijkl} \sigma_{kl}. \quad (3-2)$$

The compliance tensor  $s_{ijkl}$  is simply the inverse of the stiffness tensor  $c_{ijkl}$  introduced in chapter two. Once the strain solution is known, the three Raman mode shifts ( $\Delta\omega_1$ ,  $\Delta\omega_2$ ,  $\Delta\omega_3$ ) are computed by solving the following eigenvalue problem [52]:

$$\begin{vmatrix} p\epsilon_{11} + q'\epsilon_{22} + q\epsilon_{33} - \lambda & (p-q)\epsilon_{12} & 2r\epsilon_{13} \\ (p-q)\epsilon_{12} & p'\epsilon_{22} + q\epsilon_{33} + q'\epsilon_{11} - \lambda & 2r\epsilon_{23} \\ 2r\epsilon_{13} & 2r\epsilon_{23} & p\epsilon_{33} + q(\epsilon_{11} + \epsilon_{22}) - \lambda \end{vmatrix} = 0 \quad (3-3)$$

where  $\Delta\omega = \lambda/2\omega_0$ .

Next, the Raman mode shifts are convoluted to account for the penetration of the laser light into the silicon crystal and the width of the laser spot. An exponential decay of light intensity and gaussian intensity distribution over the spotwidth is assumed. These corrections average the Raman mode shifts over a volume of the crystal corresponding to each spot reading.

### 3.2.2 Nitride Film Edge-Induced Stress

A simulation of the stress induced by a nitride-poly stack is used to compare with a Raman measurement experiment. A 0.24 $\mu\text{m}$  thick nitride film with intrinsic stress of 1.2e10 dyn/cm<sup>2</sup> is deposited over a 0.05 $\mu\text{m}$  poly film with intrinsic stress of -3e9 dyn/cm<sup>2</sup>. The stack rests over a 0.01 $\mu\text{m}$  pad

oxide and is then patterned for a linewidth of five microns. The stress induced by the film edges is then solved for and illustrated in Figure 3-9 by stress contours of hydrostatic pressure. This represents the stress state of a Poly-Buffered LOCOS structure before oxidation. Finally using the method described in the previous section the three Raman mode shifts are solved for and are displayed in Figure 3-10.

This simulation is then compared to Raman measurement data introduced by De Wolf [52] for the same process. Since the magnitudes of the

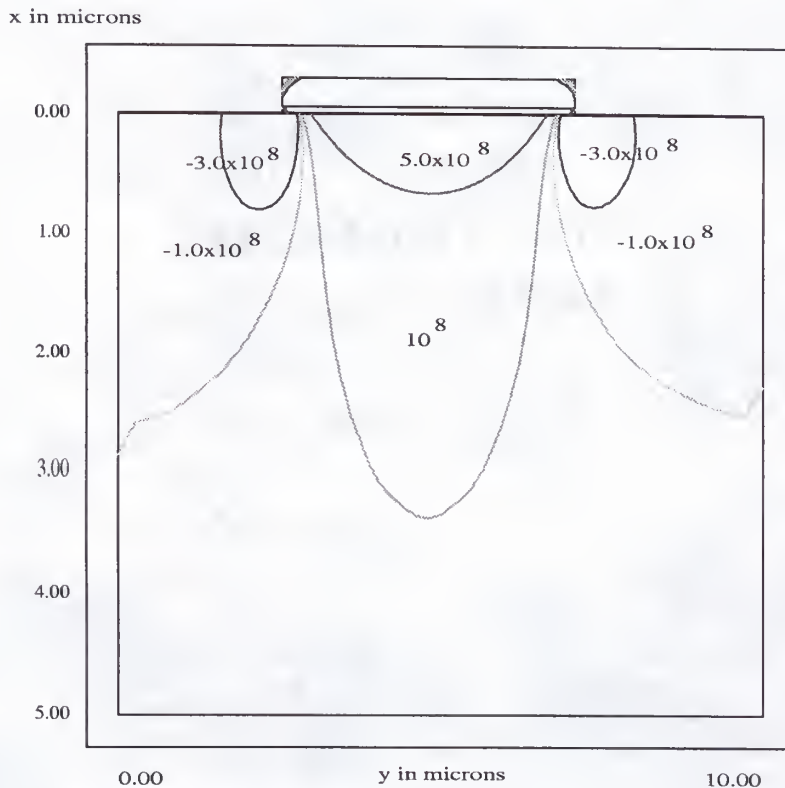


Figure 3-9 Simulation of the stress induced by the intrinsic stress of a nitride poly stack for a linewidth of  $5\mu\text{m}$ . Units are in  $\text{Dyn/cm}^2$ .



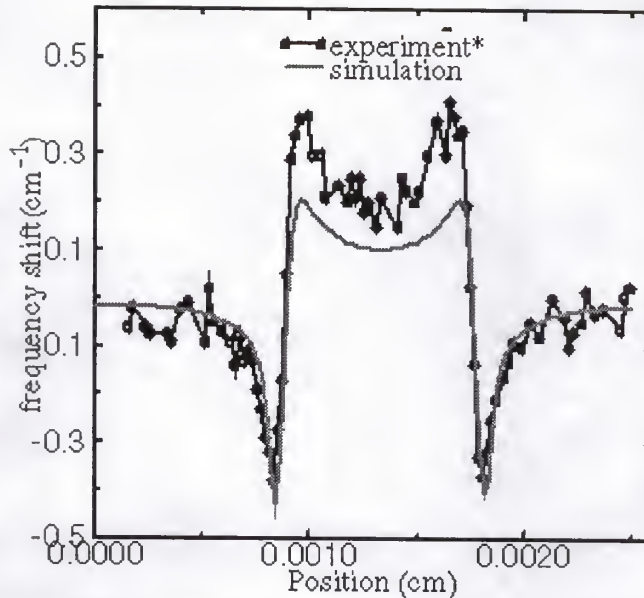


Figure 3-10 Frequency shift simulation for the three Raman modes due to nitride-poly stack edge induced strain compared with Raman measurement [52].

Raman mode shifts are small, only one shift can be recovered in experiment, which is an averaged function of the three Raman mode shifts. This simulated Raman shift is plotted along with the measured Raman shift [52] in Figure 3-10. It is noticeable that frequency shift predicted correlates well with the De Wolf's measurements. The resulting compressive strain induced shift is consistently lower than the measured Raman shifts. This indicates that the compressive strain magnitudes under the nitride film may be under-predicted. Other reasons for the discrepancy may be film-related effects on the incident signal reflection, or convolution averaging errors due to light intensity decay and spot width averaging.



### 3.3 Boron-Doped Cantilever Bending Comparisons

Next, an application using the boron-induced strain model is presented in order to validate its solutions. The strain-induced bending of boron doped cantilevers are simulated and compared with previous experimental investigations.

#### 3.3.1 Silicon Bulk Micro-Machining

Silicon bulk micro-machining is important for fabricating silicon-based sensors and transducers. Silicon sensors are often composed of thin membranes, bridges, cantilevers, and beams. These structures can be fabricated by various bulk micro-machining methods. Anisotropic wet chemical etching is often used to develop sensor structures due to its simplicity and convenience as well as providing very accurate dimensional control [18].

Boron etch stops are often used as a method for controlling etch depth in silicon substrates. Thin silicon film structures can be fabricated by thermally diffusing or implanting boron on one surface of the silicon wafer and then by etching through a mask window on the other side of the wafer. For wet chemical etchants such as KOH, the etch rate decreases significantly as the etch front approaches boron concentrations greater than  $7 \times 10^{19} \text{ cm}^{-3}$ . It is believed that the strong B-Si bond tends to bind the crystal more stringently, therefore requiring more energy to release the silicon atom [53].

It is then possible to design thin silicon film structures with the desired thickness by controlling the diffusion of the boron dopant profile so that the etch stop will occur at depth where the boron concentration approaches  $\sim 7 \times 10^{19} \text{ cm}^{-3}$ . However due to these levels of boron concentration, high levels of residual stress are generated. Since micro-machined thin membranes are critical components of silicon sensors and transducers, residual stresses in these structures may lead to mechanical failure of the device and/or deteriorate its performance. Figure 3-11 illustrates the bulk micro-machining process performed by Yang [39].

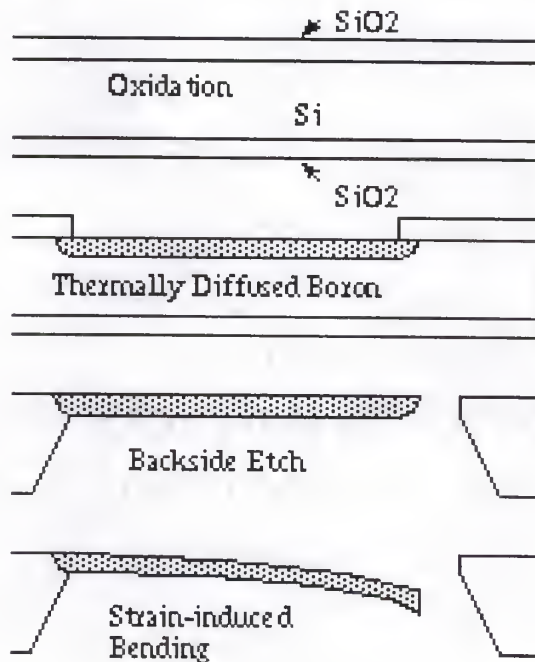


Figure 3-11 Bulk micro-machining process flow for fabrication of the cantilever.

First boron is introduced by thermal diffusion and is masked by an oxide layer on the backside of the wafer. Next the front side is masked and the backside is chemically etched. The etch slows as the surface approaches the high concentration of boron ( $\sim 6 \times 10^{19} \text{ cm}^{-3}$ ). Next the front side mask is stripped off and the cantilever is developed. In Yang's experiment, a series of front side etches then performed to study the bending behavior of cantilevers of different thicknesses doped with the same boron profile. The relative depth of the peak of the boron profile then shifts for each cantilever etch.

The high concentrations of boron necessary to produce the etch stop behavior results in residual tensile stress with magnitudes approaching and exceeding levels of  $1 \times 10^9 \text{ dyn/cm}^2$ . To relieve these high levels of stress the silicon crystal yields and may generate dislocations that may be deleterious to device and sensor performance [8]. This is one of the main reasons for studying residual stress and its origins.

The residual stress resulting is dependent on the gradient and maximum magnitude of the boron dopant profile as well as the thickness of the cantilever resulting after the backside etch. Since the boron dopant profile is not uniform the stress distribution varies with depth causing the cantilever to bend in order to relieve the resulting residual stress. This is evident in previous studies analyzing positive and negative bending of boron-doped cantilevers under varying diffusion conditions [39, 40].

### 3.3.2 Cantilever Bending Simulations

Simulations are performed using the finite element models previously described for the cantilever process described in Figure 3-11 [54]. First boron is introduced by thermal diffusion. The resulting profile has a peak concentration of  $8 \times 10^{19} \text{ cm}^{-3}$  (Figure 3-12). A backside wet chemical etch is then performed. A boron concentration of  $6 \times 10^{19} \text{ cm}^{-3}$  is chosen as the stop for this etch. The resulting cantilever thickness is about  $1.4 \mu\text{m}$ .

Next a series of 2d plane strain and 3d elastic deformation simulations is performed for the resulting boron-doped cantilever structures. The 2d cantilever has a length of  $50 \mu\text{m}$ . The grid spacing in the x-direction is  $0.05 \mu\text{m}$  and in the y-direction is  $0.5 \mu\text{m}$ . Since the x-direction spacing is limited by the necessary resolution to represent the boron profile, it becomes a challenge to preserve element quality as the cantilever length is increased while

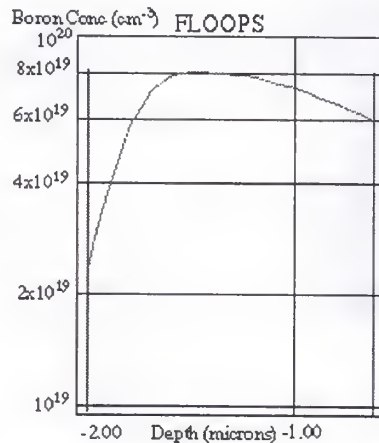


Figure 3-12 Resulting cantilever boron profile with a thickness of  $1.4 \mu\text{m}$ .



maintaining the number of elements constant. The element aspect ratio problem is magnified further in three dimensions. The 3d cantilever has dimensions of  $1\mu\text{m}$  width and  $10\mu\text{m}$  length. The 3d cantilever grid spacing is  $0.3\mu\text{m}$  in the z-direction (width),  $0.5\mu\text{m}$  in the y-direction (length), and  $0.1\mu\text{m}$  in the x-direction (thickness).

The following mechanical material properties were utilized for all simulations performed: Young's modulus ( $E_{p+Si} = 1.22 \times 10^{12} \text{ dyn/cm}^2$ ) [55], Poisson's ratio ( $\nu = 0.3$ ).

A series of varying front side etch simulations were performed to analyze how the shift in boron profile and decrease in thickness of the cantilever affected the deflection solution. These series of etch simulations model the experiment performed by Yang [39].

The results of the 2d plane strain simulations are displayed in Figure 3-13a. An example of the deflection simulation for the  $0.62\mu\text{m}$  thickness beam is shown in Figure 3-14. The structure is regrided after the nodal displacements are solved for. Figure 3-13 displays the nodal displacements along the top surface of each cantilever structure simulated. The differences between each structure thickness relates to the amount etched off the top surface. Notice that all the cantilever beams except the thickest deflected in the negative x- direction (upward in Figure 3-14). Generally as the cantilevers were etched thinner, the amount of deflection increased.



A 3d simulation for the  $1.37\mu\text{m}$  thickness cantilever is demonstrated in Figure 3-15. It is more difficult to examine the deflection visually in the 3d simulations due to the shorter length of the cantilevers. The deflection solution plot for the 3d simulations is displayed in Figure 3-13b. The same general trend also results.

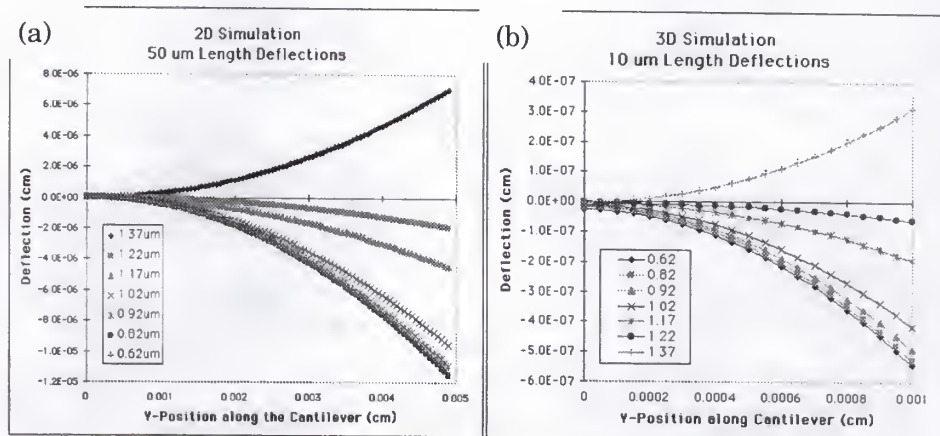


Figure 3-13 (a) Two- and (b) Three-dimensional simulation results for deflection curves for cantilevers of varying thickness.

The simulation lengths of the cantilever beams are much shorter than those fabricated in various experiments [39, 40]. Typically cantilever beams are fabricated with lengths up to 1mm in order to have an accurate measurement of the deflection. The element quality problem limits the length of the cantilevers simulated before a significant error is resulted in the elastic solution.

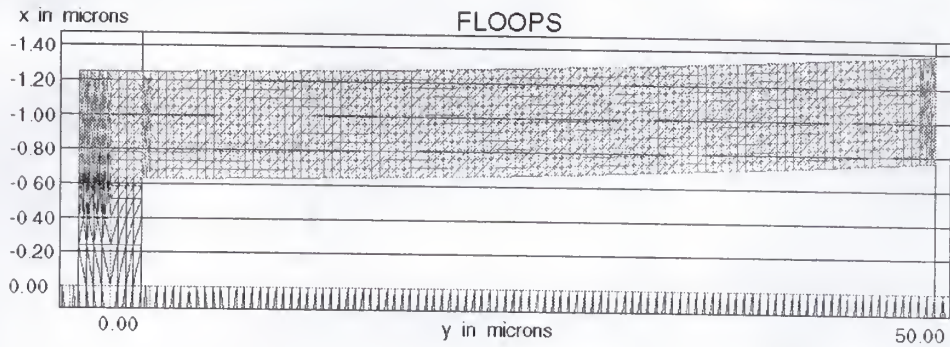


Figure 3-14 Two-dimensional plane strain simulation of the boron strain induced bending of a cantilever with thickness  $0.62\mu\text{m}$ .

To compare the simulations performed with experiments in the literature, a parabolic curve fit was used to extrapolate the expected deflections for longer cantilever beams. This is possible because beams processed the same with varying lengths would all have the same bending

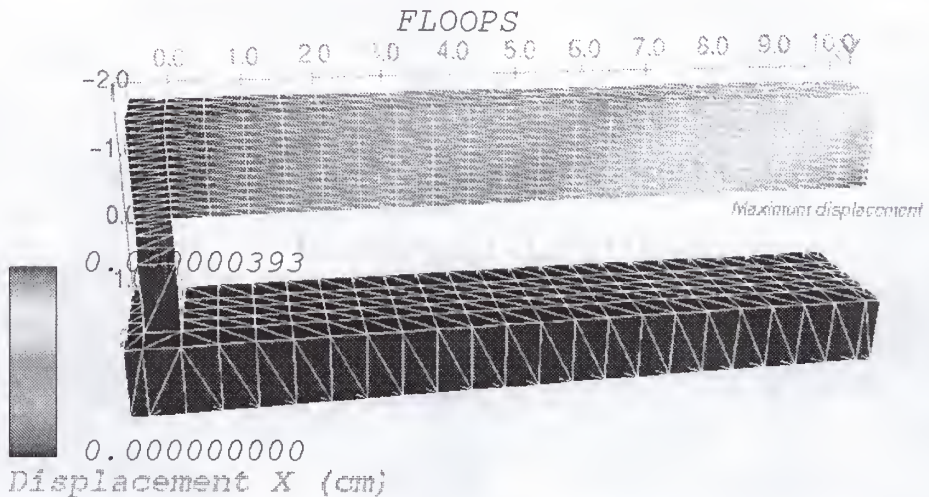


Figure 3-15 Three-dimensional simulation of the bending of  $1.37\mu\text{m}$  thickness cantilever. The maximum deflection is at the bottom corner of the cantilever beam.

moment [40]. Therefore, the cantilever deflection simulation results are then extrapolated to amounts corresponding to  $1250\mu\text{m}$  to compare with experiments performed by Yang [39]. These results are presented in the histogram shown in Figure 3-16.

Several points can be deduced from the results obtained. First is the 2d and 3d simulations resulted in roughly the same amount of deflection. This confirms that the plane strain approximation does not affect the result of the simulation and that cantilever width is not a factor in the stress solution. Second, both the simulations agree with the published experiment in the direction of the deflection for each beam thickness. However the measured

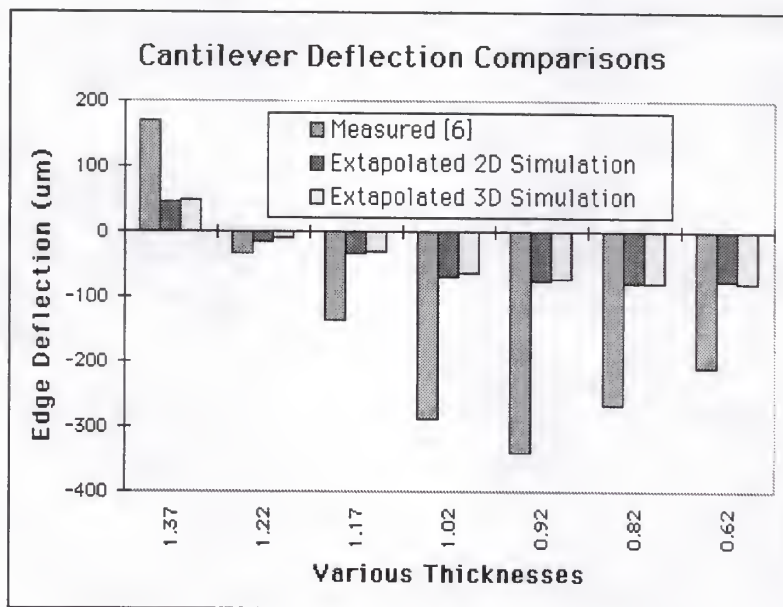


Figure 3-16 Results of both sets of simulations compared with Yang experiment [39].

deflection results are consistently about two to three times the magnitude of the simulations. Also the measured quantities have a relative maximum negative deflection for the 0.92 $\mu\text{m}$  thick beams, while the simulations showed relatively constant deflections for cantilevers of less thickness. It is believed that these differences are due to errors in the boron profile and a variation in the lattice strain coefficient.

Cantilever self-loading (due to its weight) has also been suggested as a possible source of extra strain. However the maximum bending moment due to a constant distributed load on a cantilever supported on one end is described as the following relationship [56]:

$$M_{\text{max}} = \frac{WL^2}{2} \quad (3-4)$$

where  $L$  is the length of the cantilever and  $W$  is the uniformly distributed load per unit length. For a body force such as gravity,  $W$  is represented as the following:

$$W = A\rho g \quad (3-5)$$

where  $A$  is the cross-sectional area of the cantilever,  $\rho$  is the density of silicon (2.33 gm/cm<sup>3</sup> for 5e19cm<sup>-3</sup> boron-doped silicon [41]) and  $g$  is gravitational acceleration constant. For a cantilever with rectangular cross section and thickness  $t$ , the longitudinal stress  $\sigma$  is proportional to  $M$  by the following relationship:



$$\sigma = \frac{6M}{At}. \quad (3-6)$$

The following gravity-induced stress relationship then results by substituting (3-4) and (3-5) into (3-6):

$$\sigma = \frac{3\rho g L^2}{t}. \quad (3-7)$$

It can then be shown that for a cantilever of 1000 $\mu$ m length and 1 $\mu$ m thickness, the maximum stress produced is about 7e5 dyn/cm<sup>2</sup>, which is at least three orders of magnitude less than the stress magnitudes induced by a concentration of boron at 5e19cm<sup>-3</sup>.

The most probable cause for the difference between the simulations and experiment is differences in the boron profile and lattice strain parameter. Since the strain is computed directly from the local concentration of boron and the lattice strain parameter, a shift in these results in a linear shift in the strain and therefore the stress. Therefore scaling the lattice parameter by a factor of three results in much closer agreement with the deflection magnitudes in Yang's experiment. This also results if the boron concentration is scaled by the same factor. It is therefore believed that the differences in both factors result in the observed disagreement in deflection magnitudes. This is highly probable since the accuracy in the concentration of boron reduces as the depth increases and the lattice parameter may be different for the thermally diffused case.



Another method to estimate the lattice contraction parameter, is to subtract the covalent radius of boron (0.88Å) from that of silicon (1.17Å) and then normalizing the difference to the silicon atomic radius. This results in an estimate of the normal radius contraction when a boron atom substitutes for a silicon atom:

$$\delta_{Si-B} = \frac{R_{Si} - R_B}{R_{Si}} = \frac{1.17 - 0.88}{1.17} = 0.248. \quad (3-8)$$

This lattice contraction parameter results very close to that extracted from Horn's measurements [41] (0.014Å/5.43Å)\*(100).

### 3.4 3D Boundary Loading Method Example (LOCOS)

The computational advantage of the boundary loading technique allows for less CPU intensive three-dimensional strain simulations. For two dimensional oxidation simulations, the BL method averaged 2-5 times faster depending on the number of elements in the silicon. This time savings is even much greater for three-dimensional simulations since the number of elements for a typical 3D simulation is an order of magnitude greater than in 2D.

Figure 3-17 illustrates a three-dimensional simulation of the stress induced in a LOCOS process computed by the boundary loading method. The process underwent a 1000°C wet oxidation for 15 minutes at atmospheric pressure. The pad oxide thickness is 10nm and the dimensions of the nitride

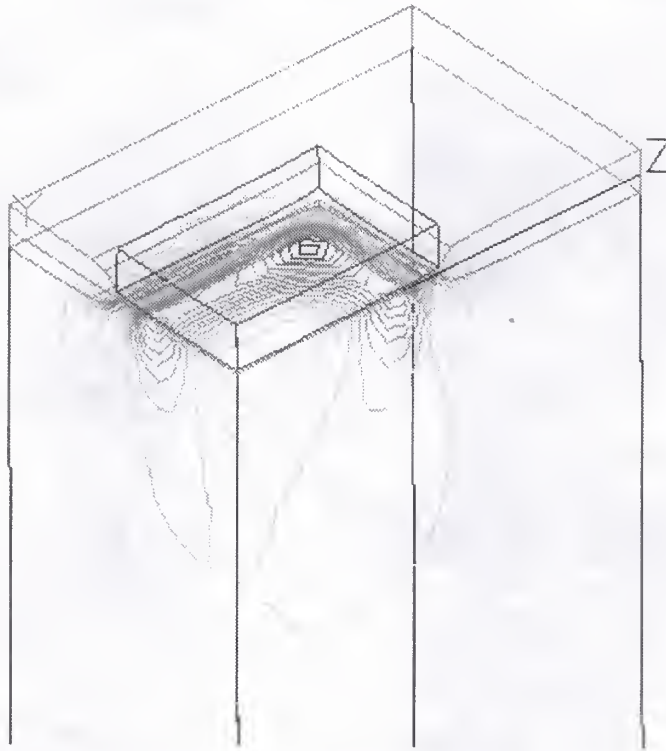


Figure 3-17 Three-dimensional simulation of LOCOS-induced stress in the substrate.

film are  $1.0\mu\text{m} \times 1.5\mu\text{m} \times 0.15\mu\text{m}$ . The iso-stress contour lines demonstrate how the stress levels are dependent on the geometry of the nitride film. In the  $1.5\mu\text{m}$  length dimension the stress level is greater than in the  $1.0\mu\text{m}$  dimension. This is evident by comparing the area occupied by corresponding iso-contour lines.

Figure 3-18 and Figure 3-19 are top views of the same simulation. The stress tensor component in the x-direction (directed normal to the surface) is

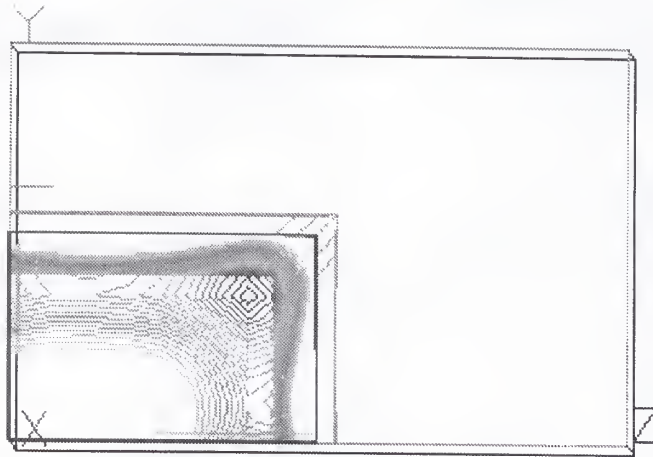


Figure 3-18 YZ plane view of the tensile  $\sigma_{xx}$  component of stress induced during LOCOS oxidation.

plotted as contour lines. Figure 3-18 demonstrates that the maximum tensile stress is at the corner of the nitride film. Figure 3-19 demonstrates that the maximum compressive stress is located at the edges of the nitride film and is greatest along the longer  $1.5\mu\text{m}$  side of the nitride film.

### 3.5 Summary

The purpose of this chapter was to demonstrate through application examples the capabilities of the strain models described in chapter two. Another intention was to validate the results of various simulations with experiments that have been reported. In the first section of this chapter, solutions of oxidation-induced stress computed by the BL method and FI

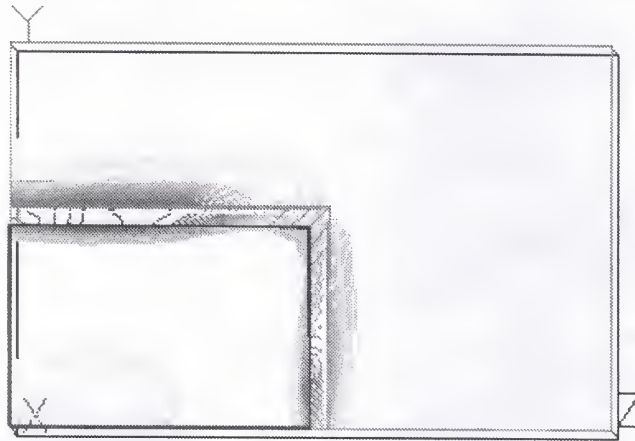


Figure 3-19 YZ plane view of the compressive  $\sigma_{xx}$  component of stress induced during LOCOS oxidation.

method were analyzed The LOCOS simulation example applications showed that at higher nitride linewidths, the two method's solutions agreed. However, at short linewidths, the two method's solutions began to disagree. This lead to believe that the stress relaxation in the silicon becomes a critical factor in solving for the strain as dimensions are scaled. Also, by analyzing the re-oxidation simulations it was found that the simulations performed with the FI method computed an overhang in the low temperature wet process at the trench corner. The BL method simulation did not. Since in experiment it was found that an overhang is resulted, it is believed that the stain solution computed using the FI method was more accurate in retarding the growth for that process.

Next, an application solving for the film edge-induced stress of a nitride poly stack was demonstrated. The results of these simulations were then used to predict the Raman signal measured over the nitride-poly stack structure using a method outlined by De Wolf [52]. The expected frequency shift in Raman modes then agreed both qualitatively and quantitatively with Raman measurement experiments for the same structure.

Next, the boron-induced strain model was used to simulate the bending of boron-doped cantilevers due to their boron-induced residual stress. The simulations were then compared with studies of this effect and produced qualitatively favorable results. The simulations agreed with experiment in comparative bending between the different thickness cantilevers. The difference in deflection magnitudes can be attributed to the lattice strain parameter used in the model. By simply scaling this parameter, simulation deflection magnitudes would coincide better with the measurements. One possible explanation may be that the lattice strain parameter used may not apply since it was measured in bulk silicon and may have a cantilever thickness dependence.

Finally, three-dimensional simulations of oxidation induced stress were demonstrated for a LOCOS process using the BL method. The BL method's efficiency allows for three dimensional strain simulations to be performed rapidly.



## CHAPTER 4

### KELVIN PROBE FORCE STI EXPERIMENT

In the previous chapter, several applications were simulated using the strain models described in chapter two. Those applications analyzed individual sources of mechanical stress and how the modeled strain fields compared with various experimental studies. In this chapter, the strain field due to the shallow trench isolation (STI) process sequence is investigated.

STI has become an essential isolation scheme as CMOS technologies are scaled down below the 0.25 $\mu\text{m}$  generation. However the basic STI process sequence involves several sources of mechanically straining the enclosed silicon region. Such sources include the thermal mismatch strain between the isolation dielectric and the silicon substrate, intrinsic stress of the nitride mask, and volume expansion-induced stress of the sidewall oxidation (Figure 4-1). It is therefore important to study each source and their combined strain influences. As pitch lengths continue to scale, the distance between transistor active areas and the STI sidewall also narrows. Therefore they continue to approach the more highly stressed regions at the sidewall interface. This in turn influences the device characteristics such as leakage through higher dislocation densities and band gap deformation. Therefore for next

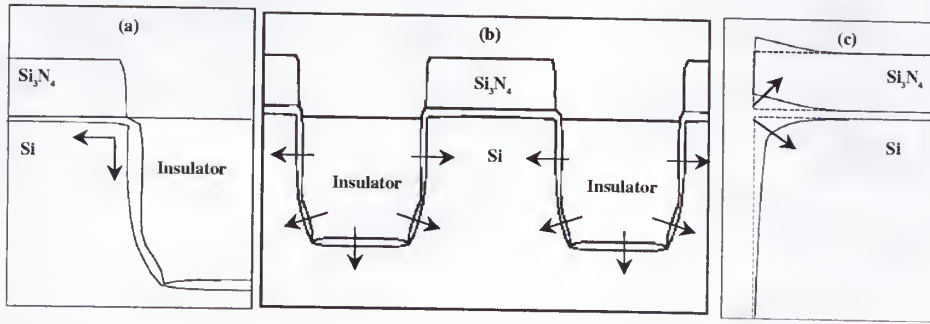


Figure 4-1 Major sources of stress in STI fabrication include the following: (a) Nitride film edge-induced, (b) Insulator thermal expansion mismatch-induced, and (c) Sidewall oxidation volume expansion-induced stress. Arrows indicate force vectors.

generation process design, methods are needed to measure the stress quantitatively. Up until now, micro-Raman spectroscopy has been the most suitable method for investigating the stress [26]. But as technologies continue to scale towards the  $0.1\mu\text{m}$  generation, this may even surpass micro-Raman's spatial resolution limits. In this chapter, scanning Kelvin probe force microscopy (SKPM) is investigated as a new method for measuring stress-induced influences in the silicon work function  $\Delta\phi$  and for inferring the stress magnitudes through coupling with mechanical strain simulation.

#### 4.1 Scanning Kelvin Probe Force Microscopy

Scanning Kelvin probe force microscopy (SKPM) has previously been researched as method for profiling 2D dopant concentration [57-62]. This has been achieved by detecting the electrostatic potential difference (EPD)

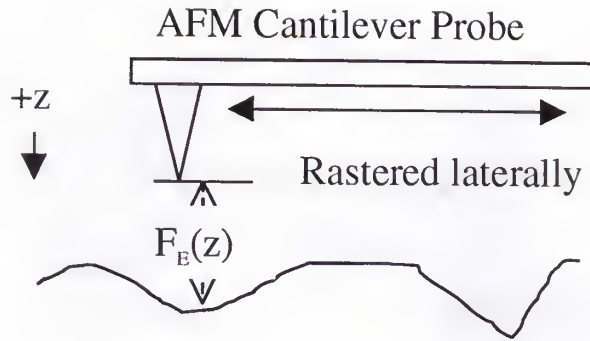


Figure 4-2 Cross-sectional sketch of SKPM measurement.

between the SKP tip and sample (Figure 4-2) through their electrostatic and van der Waals force interaction.

The method involves rastering a cantilever probe over a cross-sectional surface of the sample. At each step, both a surface topography measurement and a surface work function measurement is performed. For measuring surface topography the technique simply works as an atomic force microscope (AFM). Under the AFM mode of operation, the mean distance between cantilever probe and sample is kept constant over each step position. The cantilever probe then is oscillated mechanically at a particular frequency [58]. As the cantilever-sample mean distance changes, the van der Waals force also changes causing a change in the oscillation amplitude. The cantilever position is then corrected in the z-direction to return the cantilever to its original oscillation amplitude. The corrected cantilever position is then recorded as the cantilever is rastered across the sample and therefore maps the surface topography as demonstrated in Figure 4-2.

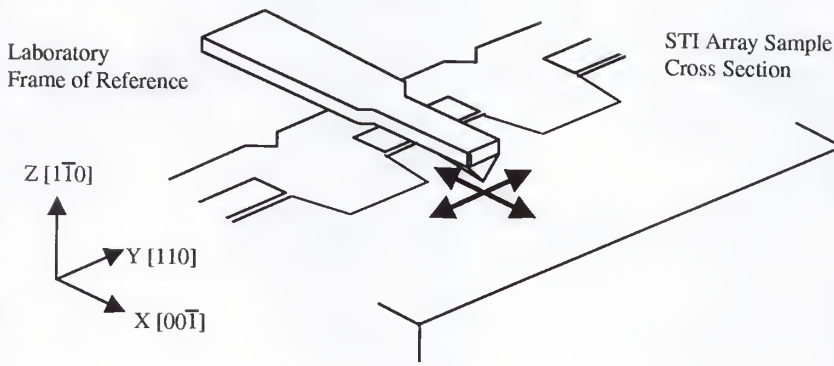


Figure 4-3 Sketch of Kelvin probe scanning laterally (y-direction) and in depth (x-direction). Variation in work function (EPD) is measured by monitoring the electrostatic force contribution to the cantilever deflection.

Surface work function measurement is performed under the SKPM mode of operation. First, an AC bias is also applied to the cantilever along with the mechanical oscillation. An electrostatic force then results between the cantilever tip and sample. A DC flat-band voltage bias is then applied to the cantilever probe to null the electrostatic force. This DC bias is proportional to EPD of the cantilever-sample system. The DC flat-band voltage is then recorded at each raster step and provides a two-dimensional map of the work function variation of the sample (Figure 4-3).

## 4.2 Work Function Influence

The EPD scanned by the SKPM method is a measure of the difference in work functions of the cantilever tip and sample. This can best be described with the energy band diagram of the system (Figure 4-4). It is similar to that of a metal-insulator-semiconductor (MIS) device band diagram, with the

airspace between the cantilever and sample representing the insulator. In this application, the cantilever tip is constituted of silicon with a layer of titanium silicide grown on the surface for improved signal detection. When the tip and sample are electrically connected, their Fermi levels become aligned. The existing electrostatic force between the tip and the sample causes the silicon bands to bend at the surface. Additional band bending is also due to the presence of surface states and charges on the semiconductor surface.

In SKPM mode, a DC flat-band bias is applied to null the electrostatic force (Figure 4-5). This applied bias represents the EPD at each rastered

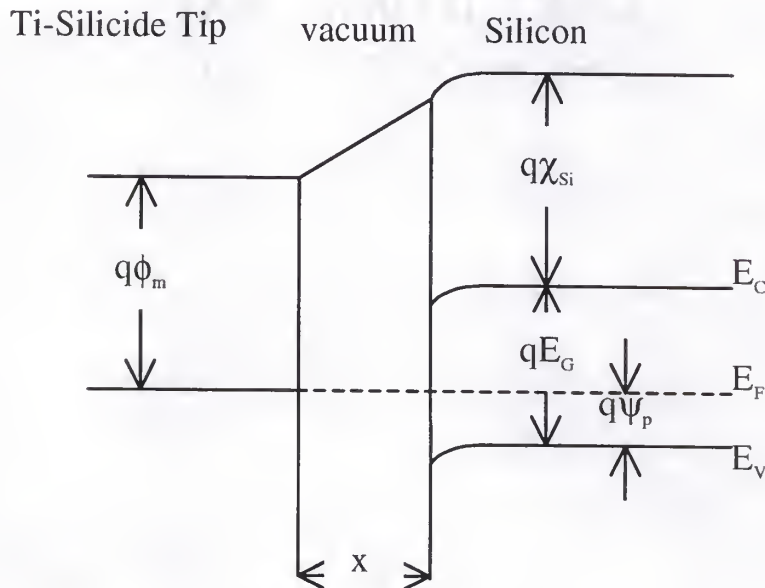


Figure 4-4 Energy band diagram of the cantilever-sample system at zero applied DC bias.



point along the cross-sectional surface of the sample. The measured  $V_{EPD}$  can then be expressed as the sum of the flat-band correcting voltage  $V_{FB}$  and surface potential terms [61]:

$$V_{EPD} = V_{fb} + \psi_s + \frac{x}{\epsilon_{ins}} \epsilon_{Si} E_s [\psi_s]. \quad (4-1)$$

The flat-band voltage is the difference between the work functions of the tip and sample:

$$V_{fb} = \phi_{Ti-Si} - \phi_{Si}. \quad (4-2)$$

The work function of the sample  $\phi_{Si}$  is the energy difference between the vacuum level and the Fermi level:

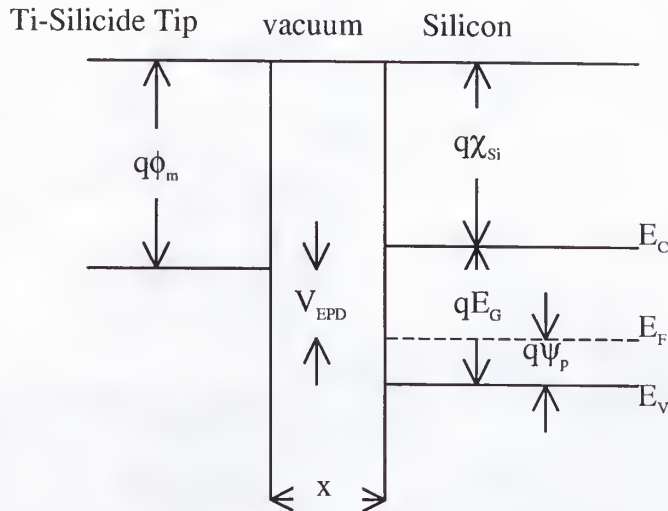


Figure 4-5 Energy band diagram after  $V_{EPD}$  is applied and the electrostatic force is nulled.

$$\phi_{Si} = \chi_{Si} + E_G - \psi_P. \quad (4-3)$$

The chemical potential  $\psi_P$  represents the energy difference between the Fermi level and the valence level of a p-doped semiconductor and is a function of the crystal properties such as dopant concentration and the energy band structure:

$$\psi_P = -kT \ln \left[ \frac{N_A}{N_V} \right]. \quad (4-4)$$

Variations in the dopant concentration  $N_A$  or the energy band structure  $E_G$  influence a variation in the silicon work function  $\Delta\phi_{Si}$ . In previous SKPM investigations [57-62], the focus was to correlate influences in  $\Delta\phi_{Si}$  to variations in dopant concentration  $N_A$  and  $N_D$ . For characterizing strain in the silicon, the dopant concentration  $N_A$  is kept constant and variations in energy band structure  $E_G$  are detected.

In chapter one, it was introduced that mechanical strain affects device characteristics through influences in the energy band of the semiconductor. Through quantum mechanical calculations [19, 21] and experiment [10, 63], it has been recognized that both hydrostatic and anisotropic stresses induce shifts and splits in the energy bands of silicon. The outcome of these investigations were deformation potential constants  $\Xi$  that characterize the magnitude of the shifts with respect to the strain applied:

$$\Delta E_{c,v} \approx \Xi \epsilon_{ij}. \quad (4-5)$$

Wortman [10] tabulated the deformation potentials that Goroff and Kleinman calculated [19, 21]. These constants are utilized to model the influence of a general strain tensor  $\epsilon_{ij}$  on the conduction and valence band levels of silicon and are summarized in Table 4-1.

The strain tensor in Table 4-1 is described in the crystal lattice frame of reference and the normal x-, y-, and z-components are oriented along the  $\langle 100 \rangle$ ,  $\langle 010 \rangle$ , and  $\langle 001 \rangle$  crystal directions respectively. This is important to note when comparing with finite element simulations, since the modeled strain tensor is described in the laboratory frame of reference (Figure 4-3) and is oriented in the  $\langle 001 \rangle$ ,  $\langle 110 \rangle$ , and  $\langle 1\bar{1}0 \rangle$  crystal directions. Therefore,

Table 4-1 Deformation potential constants for the conduction and valence energy band levels in silicon [10] [19, 21].

Energy Band influence		Energy shift (eV)
$\Delta E_v$	$\Delta \Gamma_{25}(j=1/2)$	$[\epsilon_{11} + \epsilon_{22} + \epsilon_{33}](-2.09)$
	$\Delta \Gamma_{25}(j=3/2)$	$[\epsilon_{11} + \epsilon_{22} + \epsilon_{33}](-2.09) + [\epsilon_{11} - \epsilon_{33}](\pm 2.49) + [\epsilon_{22} - \epsilon_{33}](\pm 2.49) + [\epsilon_{23}](\pm 3.28) + [\epsilon_{13}](\pm 3.28) + [\epsilon_{12}](\pm 3.28)$
$\Delta E_c$	$\Delta X_1([100])$	$[\epsilon_{11} + \epsilon_{22} + \epsilon_{33}](-1.8) + [\epsilon_{11} - \epsilon_{33}](6.38) + [\epsilon_{22} - \epsilon_{33}](-3.19) + [\epsilon_{23}](\pm 15.7) + [\epsilon_{13}](0) + [\epsilon_{12}](0)$
	$\Delta X_1([010])$	$[\epsilon_{11} + \epsilon_{22} + \epsilon_{33}](-1.8) + [\epsilon_{11} - \epsilon_{33}](-3.19) + [\epsilon_{22} - \epsilon_{33}](6.38) + [\epsilon_{23}](0) + [\epsilon_{13}](\pm 15.7) + [\epsilon_{12}](0)$
	$\Delta X_1([001])$	$[\epsilon_{11} + \epsilon_{22} + \epsilon_{33}](-1.8) + [\epsilon_{11} - \epsilon_{33}](-3.19) + [\epsilon_{22} - \epsilon_{33}](-3.19) + [\epsilon_{23}](0) + [\epsilon_{13}](0) + [\epsilon_{12}](\pm 15.7)$

a transformation of axis [31] is necessary for the strain tensor components when calculating the energy band shifts from the modeled strain tensor.

The energy band influences have deformation potential constants with a choice in sign, indicating that the level is split under the corresponding strain component. When this occurs, the minimum of the conduction levels  $\Delta X_1$  and the maximum of the valence energy levels  $\Delta \Gamma_{25}$  is chosen. Since the conduction level influence is direction dependent, the average of the minimums of the three conduction level influences  $\Delta X_1$  is computed for the  $\Delta E_c$  influence.

### 4.3 STI Experiment

The STI process outlined in Figure 4-6 is performed. The densification anneal is done in both dry oxygen and nitrogen ambients for 5 minutes at

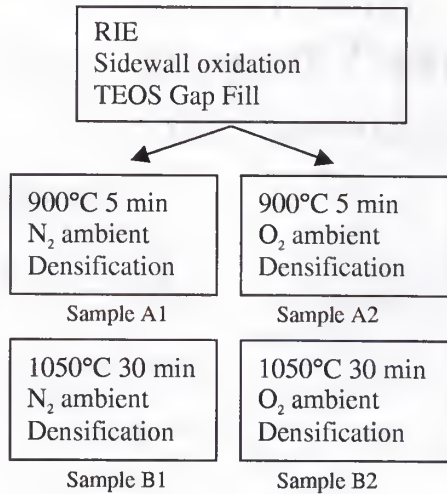


Figure 4-6 Four densification anneals are performed to investigate differences in the stress state due to each.

900°C and 30 minutes at 1050°C. The contribution of stress due to the oxidation volume expansion is then investigated and compared to a process that underwent the same thermal densification cycle. Also, the stress differences between a short densification and a long densification anneal can be studied.

Dopants have not been introduced by either implantation or thermal diffusion before the STI process. Therefore it is assumed that the boron concentrations are at the constant background levels found in the prefabricated wafer. Under these conditions it is postulated that influences in the silicon work function due to dopant concentration are constant over the scanned area. The substrate is lightly boron doped ( $\sim 1 \times 10^{16} \text{ cm}^{-3}$ ). The SKP used is a Digital Instruments Nanoscope III AFM outfitted for Kelvin measurement and the silicon probe tips have been coated with titanium silicide for improved signal detection. Samples are prepared by polishing the cross-sections of a DRAM STI array [64].

#### 4.4 SKPM Measurements

Topographical AFM images and SKPM images are scanned for each sample. An example of each is shown in Figure 4-7 for sample B1. The AFM scan is first performed to locate the desired region to be Kelvin scanned. Figure 4-7a is an example of a topographical scan. During sample preparation, the different materials in the sample are polished to different



depths. The variation for a good sample are within a few nanometers. The AFM scan is then able to detect the different material's locations from the topography without undergoing a selective etch. In Figure 4-7a regions with shallower topography show up with darker intensity such as the silicon. Regions such as the oxide between the silicon and the nitride above the silicon image with lighter intensity. A selective etch would improve the contrast and decorate the interfaces but would add another source for altering the EPD signal by removing more material that would change the stress state.

Once the desired region to be studied is located, an SKPM scan is performed over the same region as in Figure 4-7b. This image represents the detected EPD signal over the scanned region. In the SKPM image, only the EPD signal measured in the silicon region is of interest since we are concerned with a strain-induced variation in the work function. The work functions of the oxide and nitride are different in magnitude than that of silicon and therefore their EPD measurements result with a darker intensity.

The most interesting observation from Figure 4-7b is that the EPD signal in the silicon region between the STIs (Si active area) results with a higher intensity than that below the STI region. This indicates that the work function in this region varies from that in the silicon below. This behavior is more apparent when viewing the SKPM image as a perspective EPD plot

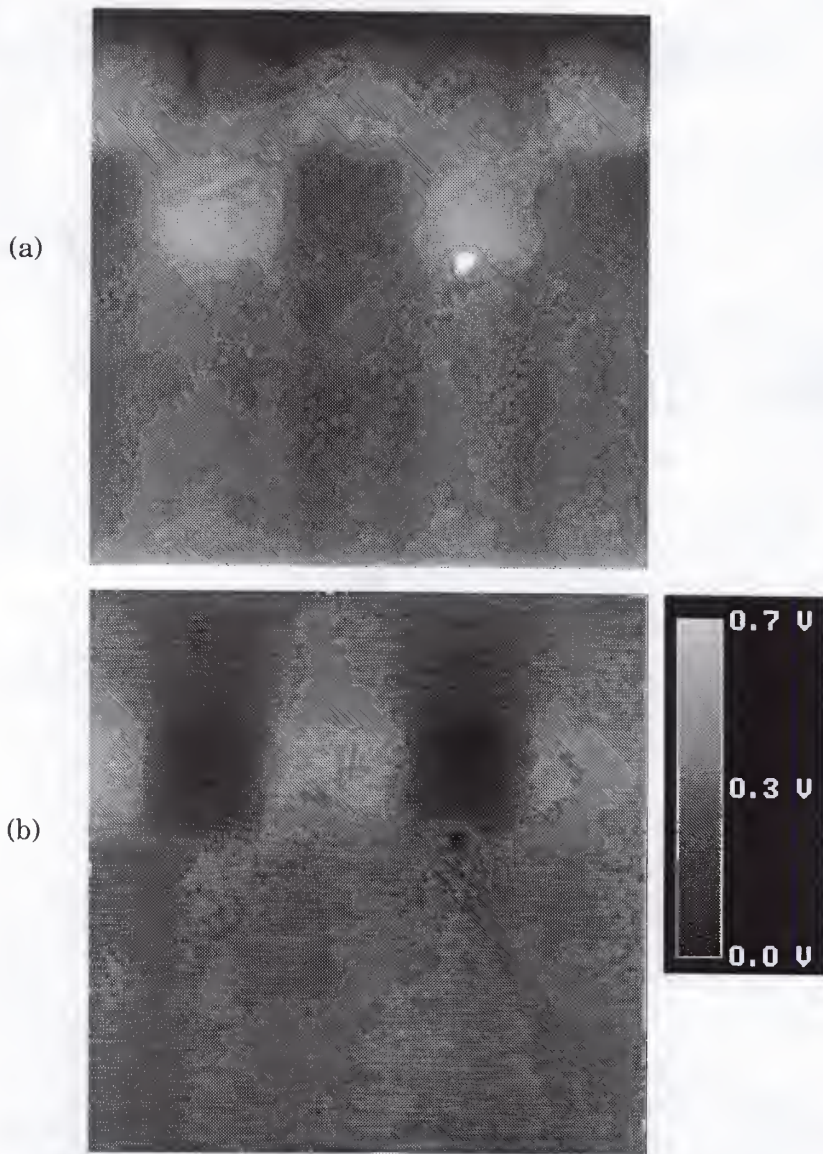


Figure 4-7 (a) AFM topographical image of STI array cross-section of sample B1, and (b) corresponding SKPM scan

The same signal pattern was observed among the four samples as that measured for sample A1 in Figure 4-8. This indicates that for each

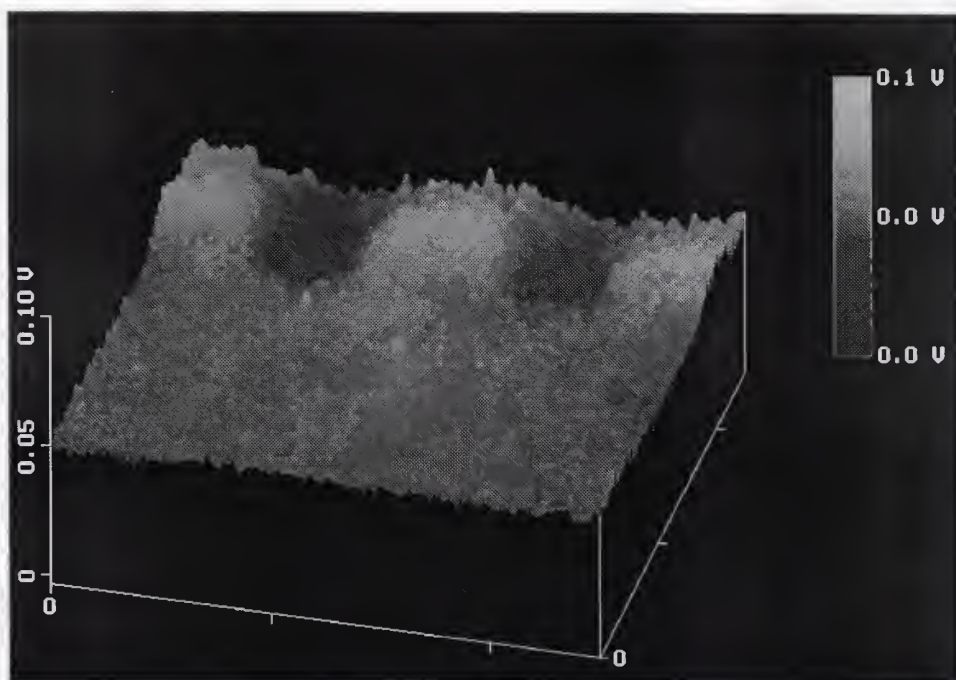


Figure 4-8 SKPM perspective EPD plot for Sample A1

densification anneal process, the silicon active area was the most highly strained region. Next the work function variations are compared for each sample. This is done by comparing cross-sectional line profiles of the EPD signal for each sample at the middle of the silicon active area (Figure 4-9). For samples A1 and A2, the difference in maximum and minimum EPD in silicon is less than 0.03V. For samples B1 and B2, the difference in maximum and minimum EPD in silicon is on the order of 0.2V. The peak influence in EPD signals is at the top surface of the silicon just below the nitride mask.



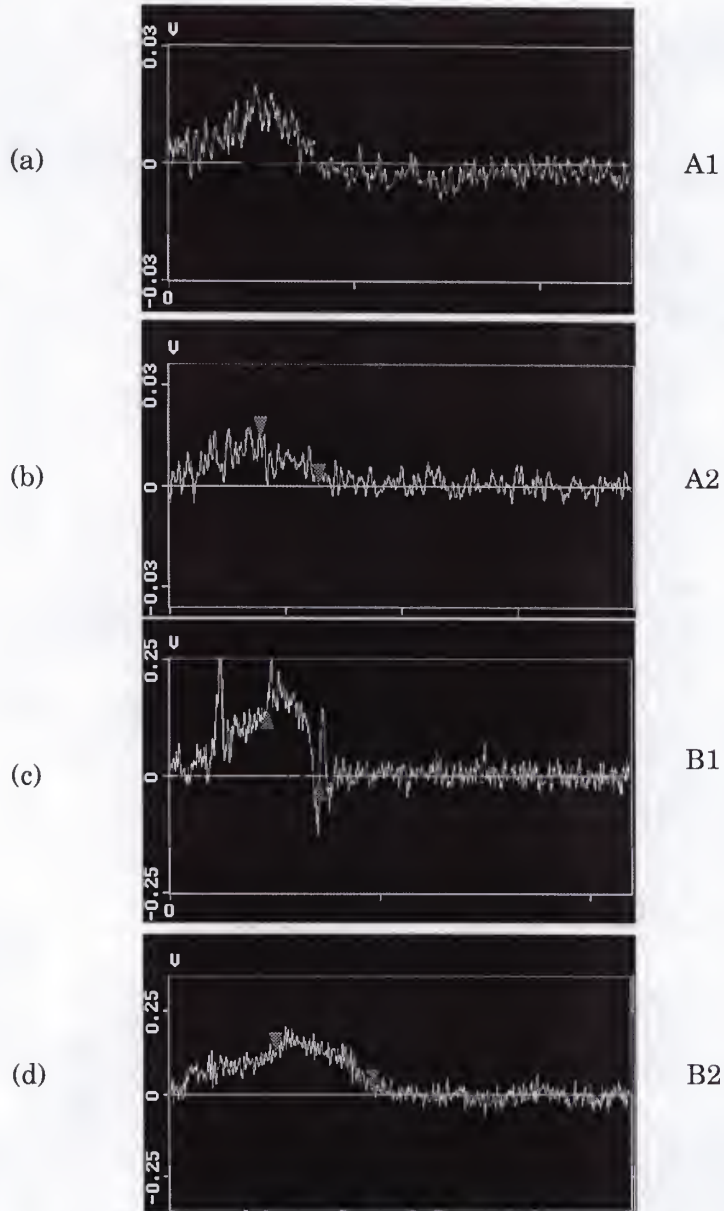


Figure 4-9 Cross-sectional profiles of EPD measurements by SKPM in the silicon active area for each sample. Arrows indicate the region of silicon enclosed by STIs.

#### 4.5 STI Strain Simulations

A quantitative relationship between the EPD measurements and theoretical strain calculations is then determined. Silicon strain calculations are determined through 2D plane strain finite element analysis implemented in the process simulator FLOOPS with the models discussed in chapter two. Materials are modeled isotropic elastic for the low temperature nitride edge-induced strain and thermal expansion mismatch-induced strain conditions. The surface films are modeled Maxwell viscoelastic for the higher temperature oxidation-induced strains. The FI method is utilized for computing the strain due to thermal oxidation.

Simulations of the stress induced by each of the STI stress sources are demonstrated in Figure 4-10. The stress due to the nitride film edge, thermal

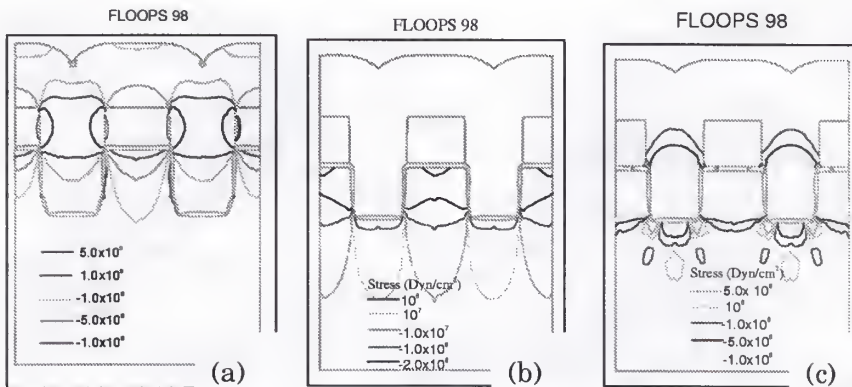


Figure 4-10 (a) Calculated lateral stress due to edges of nitride film w/ intrinsic stress  $1.4 \times 10^{10}$  dyn/cm<sup>2</sup>. (b) Calculated lateral stress due to thermal mismatch of TEOS for 600°C temperature difference. (c) Calculated lateral stress due to oxidation-volume expansion by the 1050°C dry O<sub>2</sub> 30 minute anneal.



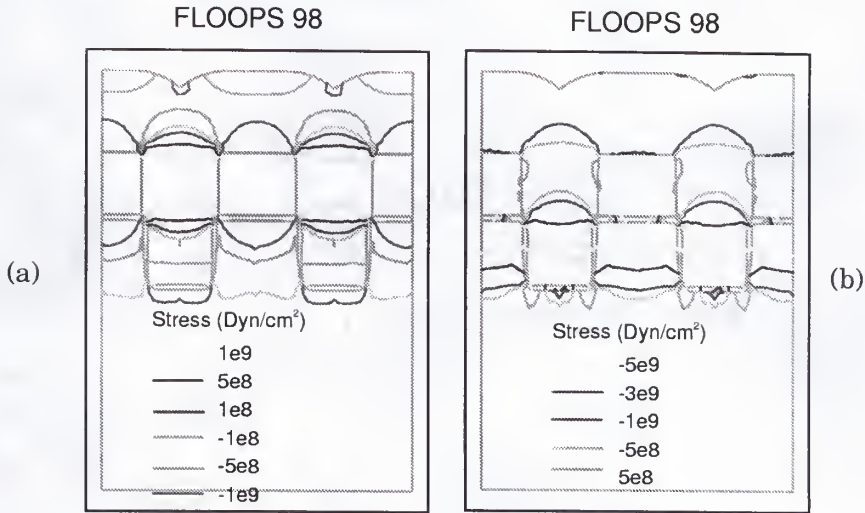


Figure 4-11 Resulting lateral stress after superposition of the solutions due to (a) nitride film edge and thermal expansion mismatch and due to (b) nitride film edge, thermal expansion mismatch, and thermal oxidation.

expansion mismatch of the insulator, and oxidation-volume expansion each provides a compressive lateral stress in the isolated silicon active area.

The final strain state is then computed by the superposition of each applicable individual solution previously mentioned in the STI process (Figure 4-11). The computed strain tensor is oriented in the laboratory frame

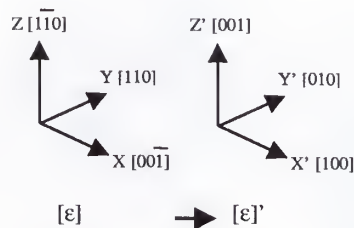


Figure 4-12 Strain referenced in laboratory frame is transformed into the crystal lattice frame.

of reference. This strain tensor is then transformed into the lattice frame (Figure 4-12) so that its influence on the valence and conduction levels can be evaluated (Figure 4-13). Calculated deformation potentials  $\Xi$  relate the lattice strain tensor to the crystal energy band shifts. A 2D distribution of the predicted EPD signal is resulted from the simulated general strain solution. The calculated work function influence can then be compared with the SKPM measured influence to verify the strain simulations and learn what magnitudes of stress may be present for each STI process.

#### 4.6 Results and Discussion

The results of the SKPM measurements of EPD are encouraging. The resulting EPD signal correlates well qualitatively with strain-influenced EPD simulations. Each results with the highest magnitude work function influence at the silicon active area between the STIs. The SKPM measurements of samples B1 and B2 resulted with higher magnitude EPD influences than those of A1 and A2. This may be due to the greater amount of densification of the TEOS resulting in these samples. However, the magnitude measured is too great to be correlated solely due to influences in the local band gap. It is believed that certain artifacts such as surface states and differences in AC signal biases between each sample measurement may cause difficulties in extracting consistent EPD measurements. However, even though these difficulties may present problems in sample to sample

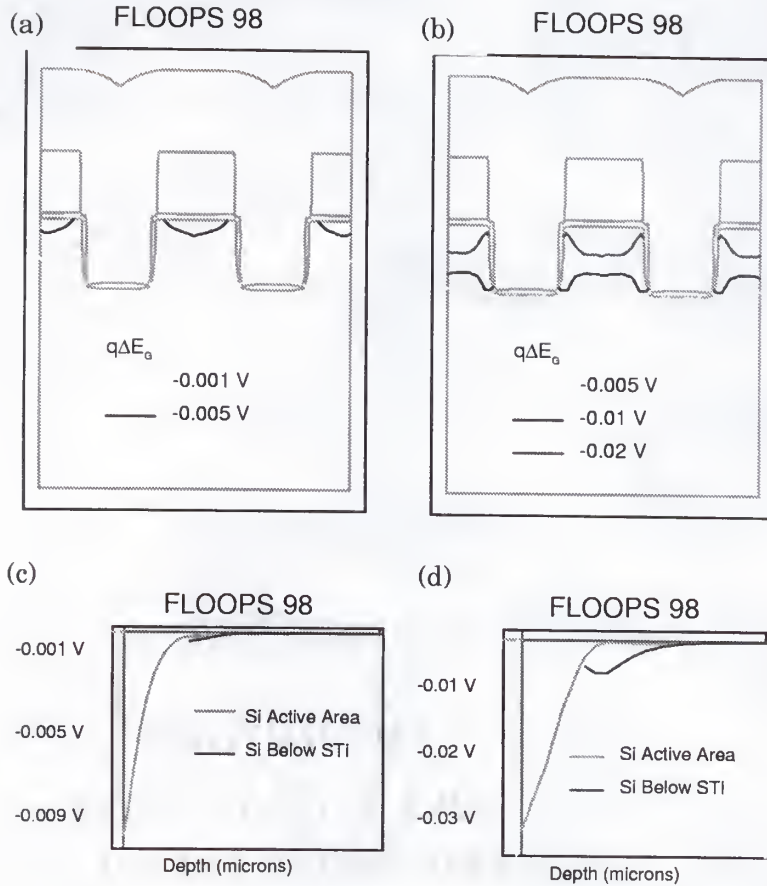


Figure 4-13 Resulting band gap variations due to (a) nitride film edge and thermal expansion mismatch and due to (b) nitride film edge, thermal expansion mismatch, and thermal oxidation. (c) and (d) represent one-dimensional cuts through the silicon active areas and below the STIs for (a) and (b) respectively.

quantitative comparisons, this technique allows for a qualitative analysis of strain over different regions of the same sample.

Figure 4-14 demonstrates a comparison for sample A1 between the SKPM measured EPD and the simulated EPD influence due to the strain induced by the STI process. The strain is first computed due to the sum of

thermal expansion mismatch of TEOS and silicon for a 900°C temperature difference and the intrinsic stress of the nitride film. The EPD is then calculated from the band gap influence that is due to the resulting strain state. Figure 4-15 illustrates a corresponding comparison for sample A2. This simulation also includes the strain due to the 5 minute 900°C dry oxidation.

The EPD measurements for A1 have been scaled so that the peak influence corresponds with the simulated maximum. This allows for a qualitative comparison. The peak influence occurs at the top silicon interface

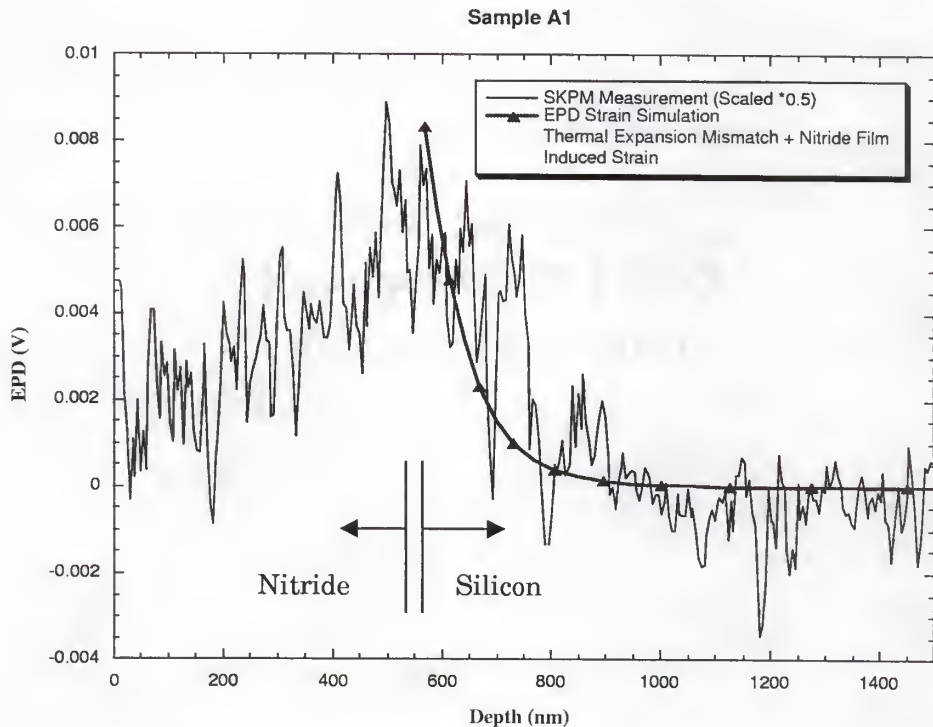


Figure 4-14 Scaled profile of EPD through the active area of Sample A1 overlaid with simulated strain-induced EPD profile.

just below the nitride and pad oxide. It then decays as the depth increases. This trend is also observed in the simulations. The magnitude of the EPD measurements does not agree for simulations of sample A1 but does agree for A2. It is believed that for A1, measurement problems discussed earlier were a greater influence than in A2. Another theory may be that even for the nitrogen densification anneal of A1, there is still oxidation at the interface due to oxygen supplied by the TEOS. This would cause the greater influence that is observed with sample A2.

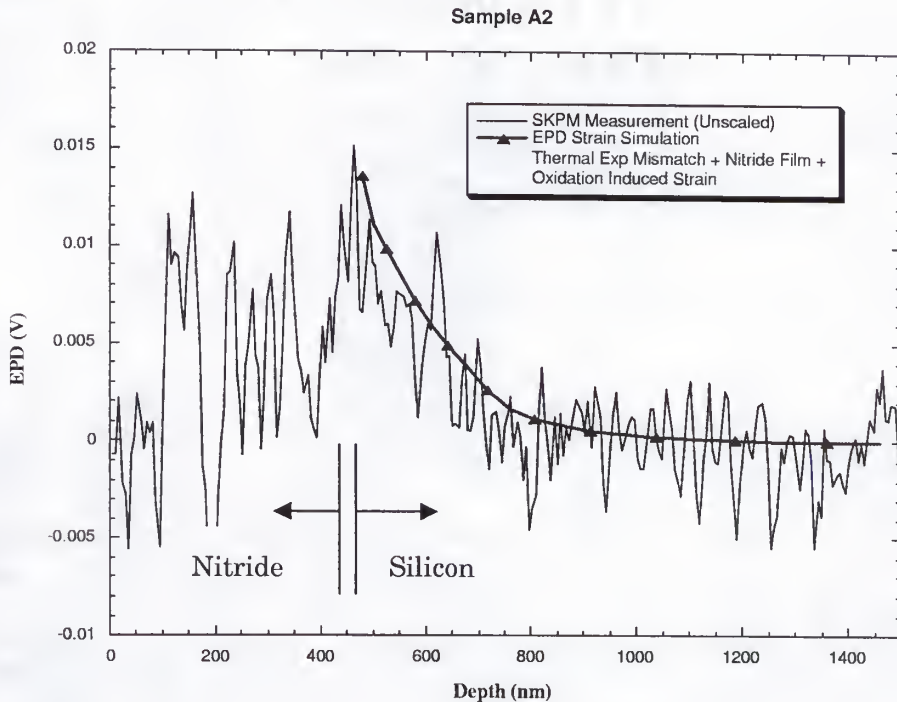


Figure 4-15 Scaled profile of EPD through the active area of Sample A2 overlayed with simulated strain-induced EPD profile.



Calibration studies are still necessary for a better quantitative interpretation of the results. Such an experiment could consist of limiting the strain source to just one source as in a nitride film edge or thermal expansion mismatch source. Then the stress state could be controlled more easily and work function variations can be extracted that are due only to one source.

#### 4.7 Summary

One goal of this work is to validate the process induced strain models described in chapter two with experimental measurements. Currently this is a major hurdle as technologies continue to scale towards the 0.1 $\mu$ m generation, due to the few characterization techniques available for localized sub-micron strain measurement. Therefore, in this chapter SKPM has been investigated as a new method for analyzing localized strains through detecting influences in the silicon work function.

The result of SKPM measurements is an associated change in the work function of silicon crystal. To relate this influence in work function, the measurements are coupled with strain simulations. Through this technique once the work function influences match, it is hoped that the mechanical strain that influenced the shift in work function is understood.

The strain simulations provided a predicted work function influence that was qualitatively in agreement with the SKPM measurements. The maximum influence was resulted at the top interface of the silicon active area

and decayed through depth, similarly to the SKPM measurements. However the magnitudes were in the neighborhood but no attempt has been made to match exactly the results of SKPM magnitudes due to the difficulties still present. Also, the simulations involve a number of material parameters that were estimated because they are not very well known currently, such as the mechanical and oxidant diffusion properties of TEOS. Varying these parameters can change the strain state simulations resulted considerably and therefore change the anticipated effect on the band gap. Considerable progress has been achieved in utilizing SKPM as a characterization technique of stress. However, calibration studies are still necessary for a better quantitative interpretation of the results.

## CHAPTER 5

### STRESS INFLUENCES IN DEVICE OPERATION

The influence of externally applied stress on electrical characteristics has been investigated for many years. Most of the research applies to sensor development rather than digital or analog IC influences. It has long been recognized that the externally applied stress has a direct influence on the energy band structure of a semiconductor [10]. This influence on the bandgap is mostly noticeable in minority carrier devices such as diodes and bipolar transistors since the minority carrier densities are strong functions of the band gap. Quantifying this effect allows a better understanding of strain influence on reverse saturation current levels and therefore supports leakage issues in CMOS and DRAM circuits, which are majority carrier devices.

#### 5.1 Uniaxial Stress Influence Experiment

Experiments have been performed relating stress effects on pn-junction operation to band structure influences based on quantum mechanical calculations [10, 19, 21]. In these studies the changes in the various semiconductor energy levels were quantified for hydrostatic and uniaxial compressive applied stress. It was shown that for silicon, band-gap

variation due to a uniaxial compressive stress is greatest in the  $\langle 111 \rangle$  direction. Also, it was recognized that a significant band-gap variation began as stress levels increased above  $1 \times 10^9$  dyn/cm<sup>2</sup> (Figure 5-1).

These derivations were then correlated to experiments involving the application of stress directly on the surface of the device with an indentation

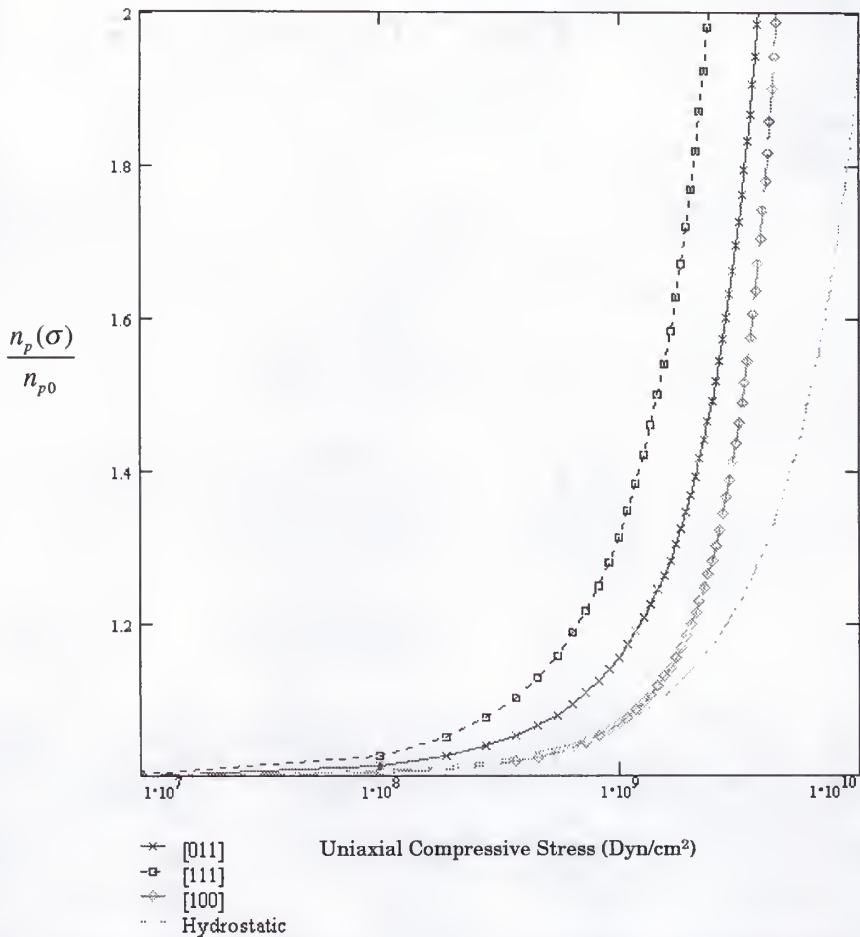


Figure 5-1 Ratio of stressed minority carrier density to unstressed minority carrier density as a function of uniaxial stress as forecasted by Wortman's model [10].

mechanism [25]. This method allows for application of a compressive stress in the region of the pn-junction but may lead to some discrepancies in the electrical measurements due to the creation of recombination centers because of the extremely high stress levels encountered. Also this mechanism does not allow for a method of exerting tensile strain in the pn-junction region.

An experiment was performed to measure the influences of an externally applied compressive and tensile stress on various types of pn-junction devices. This allows for comparison with a previous experiment [10] and for determining if the same results held for modern pn-junction devices with shallower junctions. Also it allows for measurement of tensile influences which were not performed in the earlier experiments.

#### 5.1.1 Stress-Inducing Apparatus Design

The uniaxial stress experiment involved the development of an apparatus that mechanically exerts a known stress on fabricated devices. As the stress is applied, the device operation could be monitored to observe the stress-induced variations. The apparatus was designed so that it could fit on the chuck for the probe station and not interfere with the probe pins and microscope of the probe station. This tool was also designed so that it bends a wafer strip up and down and therefore exerts a uniaxial compressive and tensile stress on the top surface of the wafer.



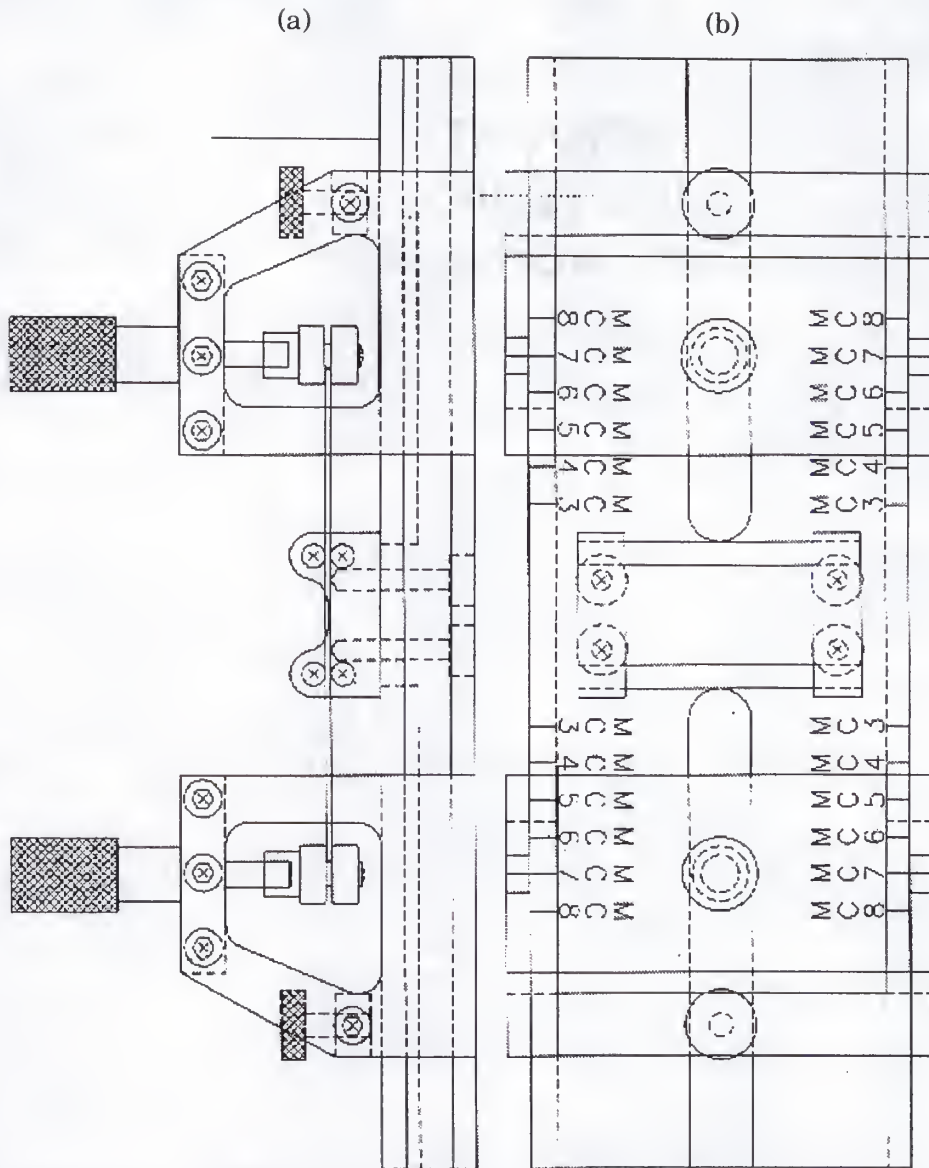
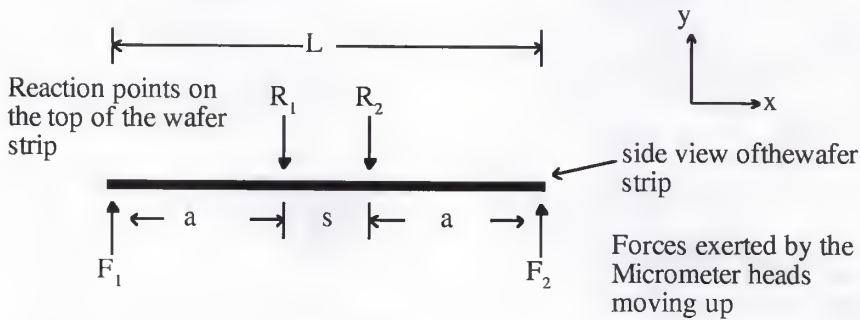


Figure 5-2 A CAD sketch of the stress-inducing tool. The left figure (a) is the side view and the right figure (b) is a top view. The wafer strip is placed between the notches of the micrometer heads as is shown in (a).

Other constraints involved in the tool design were that it accommodate wafer strips of varying widths, lengths and thicknesses. Precision in the

amount of bending displacement at the ends of the wafer strip needed to be on the order of less than 0.01mm. The wafer-bending tool was constructed with a spacing of 1.6 cm at the center between reaction points. The wafer bending apparatus is sketched in Figure 5-2.

Configuration for exerting compressive stress on the top of the wafer



Configuration for exerting tensile stress on the top of the wafer

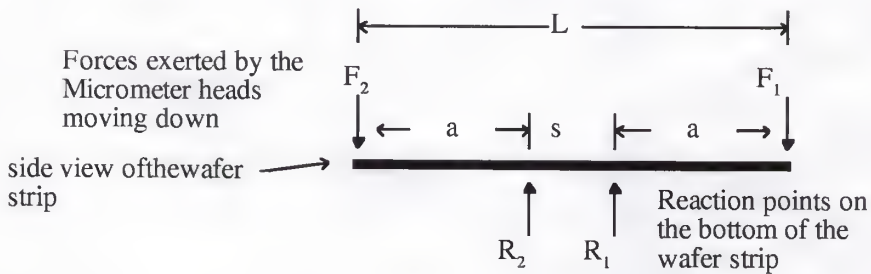


Figure 5-3 Free-body diagrams displaying the applied and reacting forces producing tensile and compressive stress along the top of the wafer strip.

### 5.1.2 Stress-Wafer Deflection Relationship

Standard elastic beam bending analysis is used to relate the amount of wafer bending at the edge to the stress resulting in the center. The free body diagram in Figure 5-3 shows the configuration of the forces acting on the wafer strip.

The geometry represented in Figure 5-3 is explained as the following: The length of the wafer strip is  $L$ ,  $s$  is the distance between reaction forces and  $a$  is the distance from the edge to the fulcrum reaction and is equal to  $(L-s)/2$ . For  $F_1 = F_2$ , by the condition of static equilibrium  $R_1 = R_2 = F_1 = F_2$ . This holds true for equal edge deflections on both sides of the beam. Using the concentrated force approximation at the beam edges as singularity functions, the following relation can be derived [56]:

$$y_{Dis} = \frac{M}{6EI} [4a^2 - 3L^2] \quad (5-1)$$

where  $y_{Dis}$  is the vertical displacement at the wafer edge referenced to the

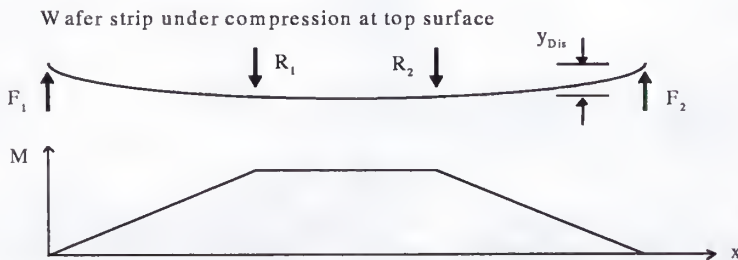


Figure 5-4 The moment function exerted along the wafer strip is at a maximum and constant between the reaction forces.

reaction positions which are fixed. The Elastic modulus  $E$  is oriented in the direction along the beam, and  $I$  represents the moment of inertia of the wafer strip. The moment  $M$  is at a maximum within the reaction forces as shown in Figure 5-4.

From beam bending analysis the moment is related to the axial stress by the following relation:

$$\sigma_{xx} = -\frac{My}{I} \quad (5-2)$$

where  $y$  is the vertical distance from the center of the beam. As an example, if the wafer thickness  $t$  is  $600\mu\text{m}$  then at the top surface  $y = +300\mu\text{m}$ . From equations (5-1) and (5-2) the axial stress can be expressed as a function of vertical beam edge displacement and vertical position

$$\sigma_{xx}(y_{Dis}, y) = -\frac{6Ey_{Dis}y}{[4a^2 - 3L^2]} \quad (5-3)$$

For the force configuration shown above, the uniaxial stress can be determined at the top and bottom surface of the center of the wafer strip from the following expressions respectively:

$$\sigma_{xx}(y_{Dis}) = -\frac{3Ety_{Dis}}{[4a^2 - 3L^2]} \quad (5-4)$$

$$\sigma_{xx}(y_{Dis}) = \frac{3Ety_{Dis}}{[4a^2 - 3L^2]} \quad (5-5)$$

These equations show equally tensile and compressive magnitudes of stress result on both surfaces of the wafer strip.

## 5.2 Experimental Procedure

DC measurements were performed to record the stress-induced forward bias current influence. In forward bias, the diode forward current  $I_F$  is proportional to the saturation current  $I_s$  and the recombination current  $I_{R0}$  by the following relations:

$$I_F = I_s \exp\left(\frac{V_F}{V_T}\right) + I_{R0} \exp\left(\frac{V_F}{2V_T}\right) \quad (5-6)$$

$$I_s = qA \left[ \frac{D_p}{L_p} p_{n0} \coth\left(\frac{W_n}{L_p}\right) + \frac{D_n}{L_n} n_{p0} \coth\left(\frac{W_p}{L_n}\right) \right] \quad (5-7)$$

$$I_{R0} \cong \frac{qAn_iW}{2\tau_0}. \quad (5-8)$$

The variation in current in forward bias can then be attributed through the stress influence on the current components  $I_s$  and  $I_{R0}$ . The minority carrier densities  $p_{n0}$  and  $n_{p0}$  and the intrinsic carrier concentration  $n_i$  are influenced by the externally applied stress through its effect on the bandgap  $E_G$ .

$$\frac{n_i(\sigma)}{n_{i0}} = \exp\left(\frac{-\Delta E_G(\sigma)}{kT}\right) \quad (5-9)$$

The carrier lifetimes  $\tau_0$  are also influenced by stress through the creation of dislocations or recombination centers to relieve the strain induced. The



influences of stress on the minority carrier densities are proportional to its effects on the total current.

The following diodes were electrically characterized under varying applied stresses:

Lateral P+ Area Diode ( $250\mu\text{m} \times 750\mu\text{m}$   $A=187500\mu\text{m}^2$   $P=2000\mu\text{m}$ )  
 Lateral P+ Periphery Diode ( $250\mu\text{m} \times 750\mu\text{m}$   $A=187500\mu\text{m}^2$   $P=2000\mu\text{m}$ )  
 N+/P-Sub Area Diode ( $250\mu\text{m} \times 750\mu\text{m}$   $A=187500\mu\text{m}^2$   $P=2000\mu\text{m}$ )  
 P+/N-Well Area Diode ( $250\mu\text{m} \times 750\mu\text{m}$   $A=187500\mu\text{m}^2$   $P=2000\mu\text{m}$ )  
 N+/P-Sub Periphery Diode ( $A=92434\mu\text{m}^2$   $P=45414\mu\text{m}$ )  
 P+/N-Well Periphery Diode ( $A=92434\mu\text{m}^2$   $P=45414\mu\text{m}$ ).

The wafers were cleaved into strips of varying lengths and widths in the  $\langle 110 \rangle$  directions perpendicular and parallel to the wafer flat. The average dimensions of each strip were about five centimeters in length and two centimeters in width.

To measure the influence of stress on each diode, the DC voltage is stepped up from  $-1.0\text{V}$  to  $0.5\text{V}$  on the P-sub terminal of the N+ diodes and  $1.0\text{V}$  to  $-0.5\text{V}$  on the N-Well terminal of the P+ diodes. The bias voltage is stepped in  $30\text{mV}$  increments. Current is measured on both terminals of the diode. Forward biased measurements were taken at various edge deflection readings (Figure 5-5). These readings were then converted to the appropriate stress levels generated by the previously introduced compressive (5-4) and tensile relationships (5-5).

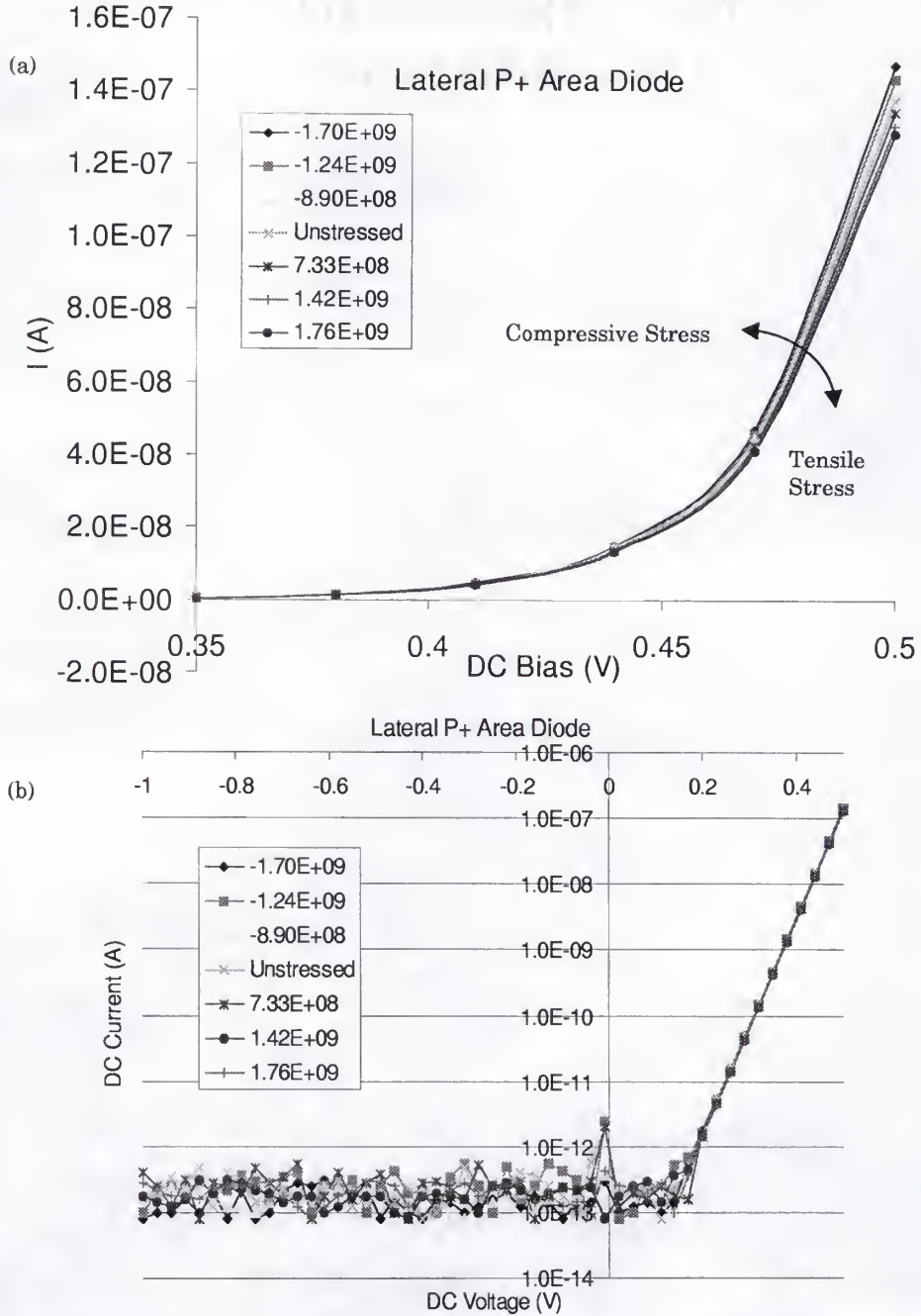


Figure 5-5 (a) Forward and (b) semi-log IV Characteristic for the lateral P+ large area diode under applied uniaxial stress (dyn/cm<sup>2</sup>).

The forward biased operation is observed to compare the influence between different stress states. The stress-induced variation  $\Delta I(\sigma)$  is measured as the following:

$$\Delta I(\sigma) = \frac{I(\sigma) - I(\text{unstressed})}{I(\text{unstressed})} (100). \quad (5-10)$$

This variation is calculated for each measured bias point. It is then averaged over the interval from 0.1V to 0.5V forward bias points. In this interval, the current magnitudes were high enough to show consistent variations due to the applied stress (Figure 5-6).

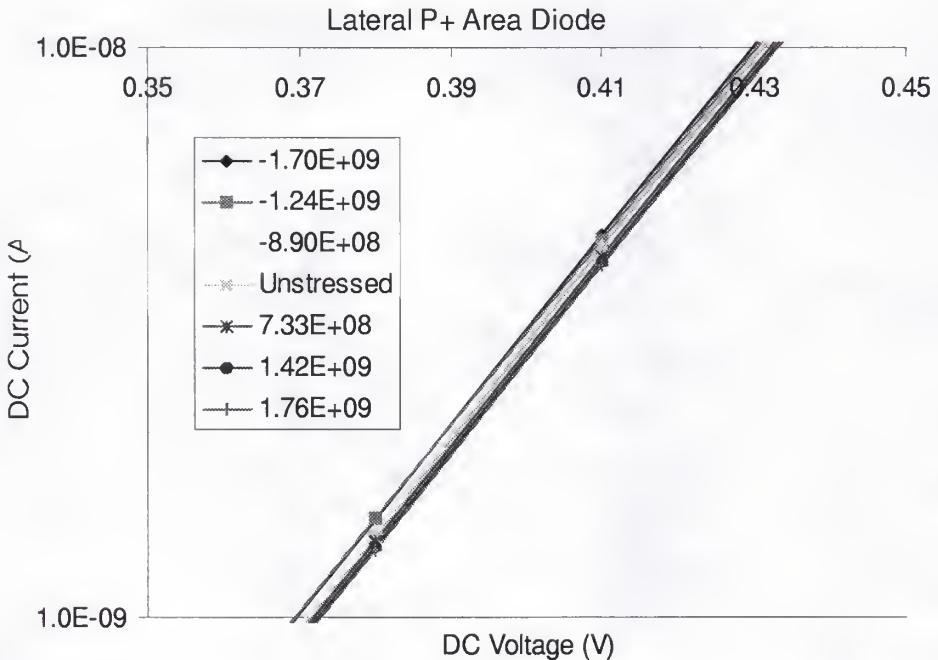


Figure 5-6 Magnification of the semi-log IV Characteristic for the lateral P+ large area diode under applied uniaxial stress ( $\text{dyn/cm}^2$ ) resulting in shifted current measurements with same slope.

### 5.3 Experimental Results

Stress levels ranging from  $-2 \times 10^9$  to  $+2 \times 10^9$  dyn/cm<sup>2</sup> were applied to each diode. This corresponds to maximum levels of one-third the yield strength of dislocation free silicon at room temperature [65]. Exceeding this stress range caused the wafer strip samples to shatter consistently due to micro-fractures along the wafer strip edges resulting from the preparation. Figures 5-7 to 5-9 display how the applied external stress influenced the forward biased DC behavior for the different diodes tested. The reverse bias operation was also analyzed under applied stress. However, the reverse bias current magnitudes were too low to detect influences due to the applied stress.

It is found that the applied stress affected the DC operation consistently for each of the diodes. Compressive stress increases the current for an applied DC voltage bias. Tensile stress decreases the current as compared to the unstressed case. For compressive stresses of about  $2 \times 10^9$  dyn/cm<sup>2</sup>, N+ diodes current increase was about 10-15 percent. Over the same stress levels, P+ diodes current increase was about 7-10 percent. Tensile stresses just below  $2 \times 10^9$  dyn/cm<sup>2</sup> caused both N+ and P+ diodes' currents to decrease about 6-8 percent. These results remained consistent when the stress is applied along the perpendicular  $\langle 011 \rangle$  directions.

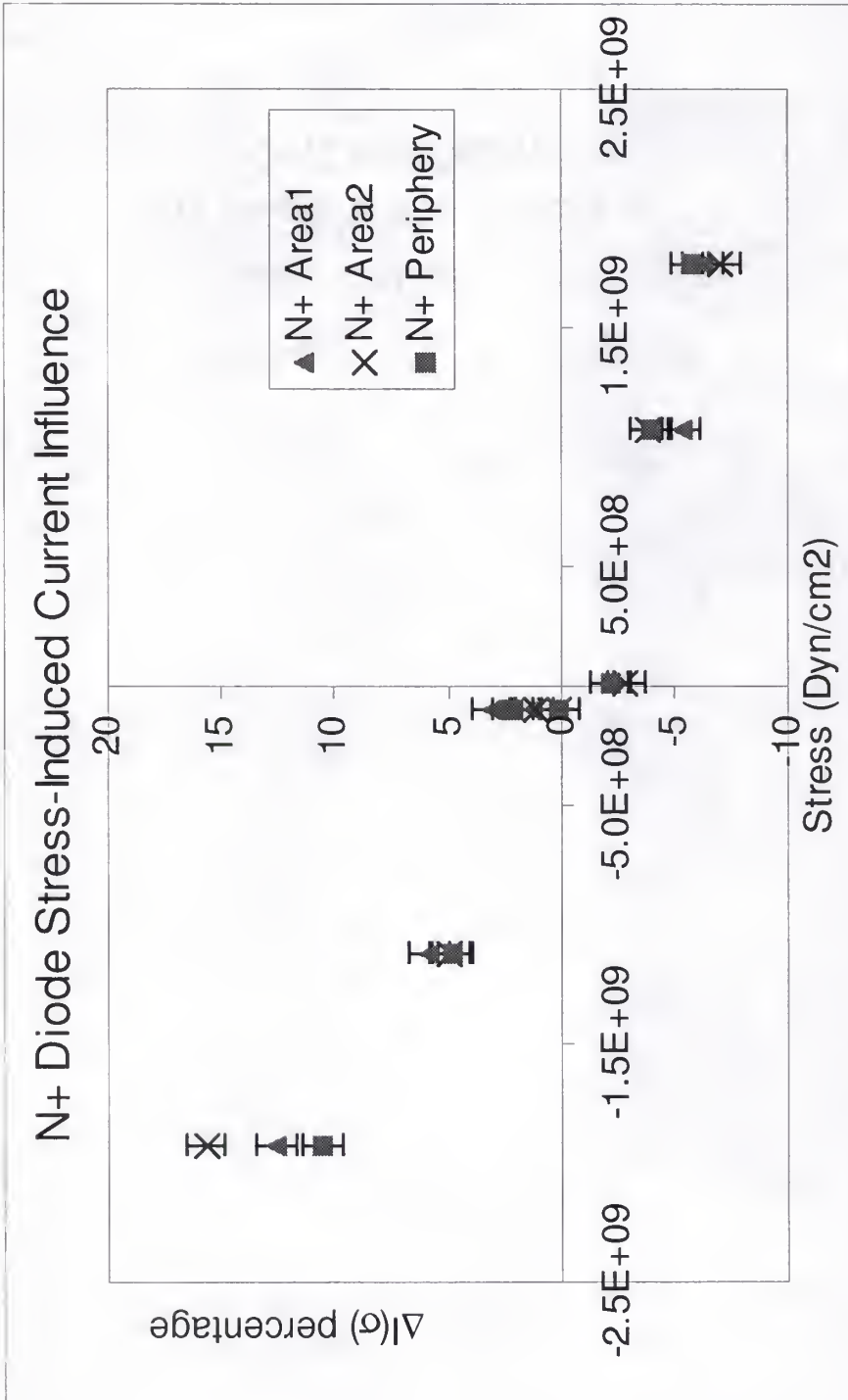


Figure 5-7 Applied stress-induced influence on N+ diodes.



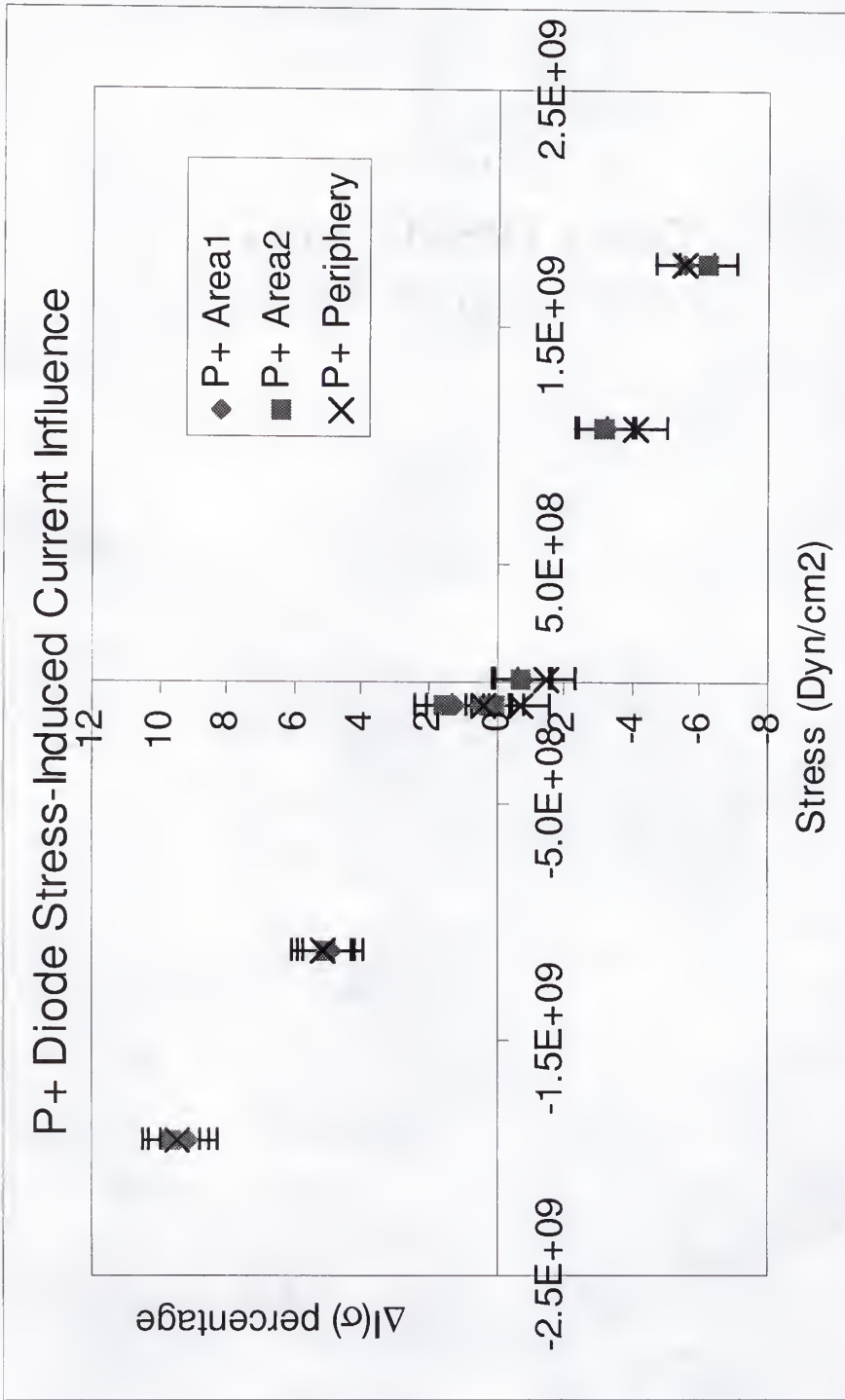


Figure 5-8 Applied stress-induced influence on P+ diodes.

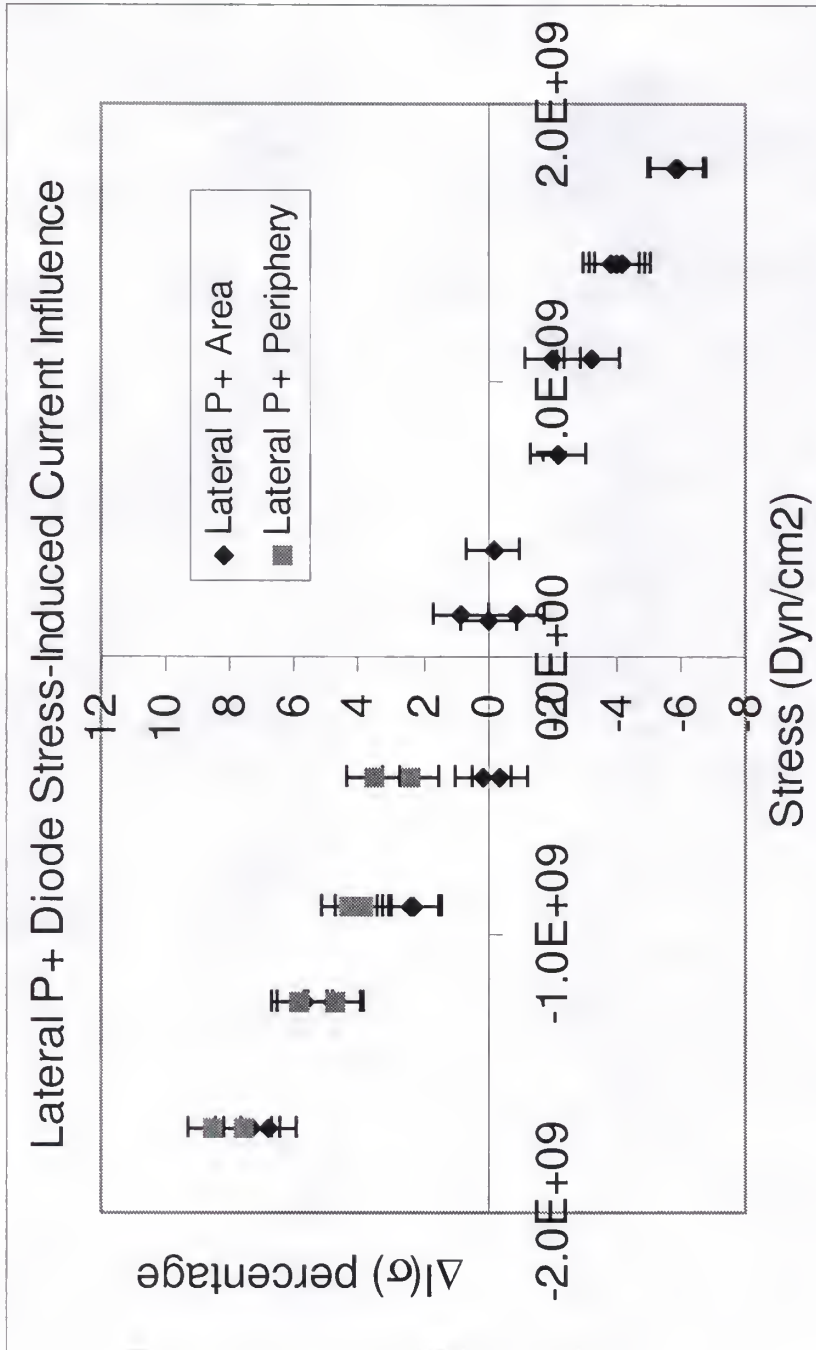


Figure 5-9 Applied stress-induced influence on Lateral P+ diodes.

Some samples were measured several times at the same applied stress levels to determine the repeatability of the influence. An example of this is shown in Figure 5-9. It is observed that the measured  $\Delta I(\sigma)$  influences were within one and a half to two percent variation. The micrometer head's reading accuracy for the edge deflection measurement is estimated to be about  $\pm 0.02\text{mm}$ . For a sample of 5cm length this translates to about  $\pm 4.6\text{e7 dyn/cm}^2$ .

The following trend-lines were linearly extracted from the N+ diodes influence measurements for compressive and tensile stresses respectively:

$$\Delta I(\sigma) = -6.74e-11 \cdot \sigma \quad (5-11)$$

$$\Delta I(\sigma) = -3.63e-11 \cdot \sigma. \quad (5-12)$$

Similarly for P+ diodes, the following linear relationships were extracted:

$$\Delta I(\sigma) = -4.891e-11 \cdot \sigma \quad (5-13)$$

$$\Delta I(\sigma) = -3.273e-11 \cdot \sigma. \quad (5-14)$$

If it is assumed that the change in current is due to the stress influence on the  $I_s$  current component alone, the linear relationships (5-11) - (5-14) can be entered into expression (5-9) to solve for the band gap influence  $\Delta E_G$ :

$$\Delta E_G = -kT \ln[\Delta I(\sigma) + 1]. \quad (5-15)$$

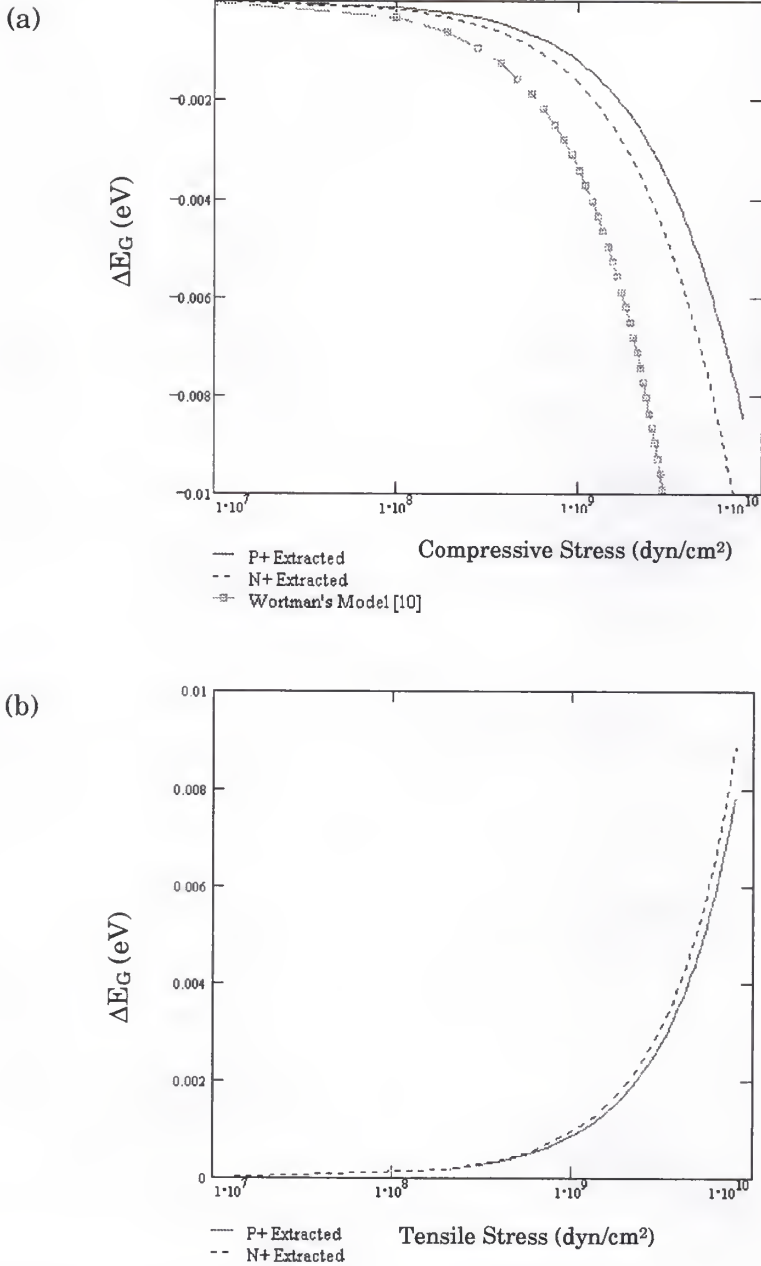


Figure 5-10 Extracted Band gap influences due to (a) compressive and (b) tensile  $\langle 011 \rangle$  uniaxial stress.

The results for the band gap influences extracted from the measurements are illustrated in Figure 5-10 along with Wortman's model [10] predictions for compressive uniaxial  $\langle 011 \rangle$  stress.

Applying Wortman's model, a  $\langle 110 \rangle$  uniaxial compressive of about  $2 \times 10^9$  dyn/cm<sup>2</sup> would result in about 30-35 percent increase in  $I_s$  (Figure 5-1). The corresponding influence extracted from the preceding measurements resulted in about 8-15 percent increase. This explains why in Figure 5-10 the model also predicts a larger  $\Delta E_G$  than was extracted from the experiment. The assumption that  $I_s$  and  $I_{R0}$  are similarly affected by mechanical stress may lead to some of the error in correlating the measurements with the experiment. This assumption neglects influences in carrier mobilities and lifetimes. Also, the relationship between wafer edge deflection and applied stress, equations (5-4) and (5-5), may induce some error in determining the stress state. However, the measurements provide at the very least a minimum bound on the influence of both tensile and compressive stress on the band gap  $E_G$ .

#### 5.4 Summary

According to the results plotted, the largest degree of measurement error encountered was at the lower magnitude stress levels. However at both high compressive and tensile stress levels a more consistent stress influenced measurement was observed. For the range of stresses produced, the



relationship looks linear. However, the highest stress magnitudes achieved using this technique were in the  $\pm 2 \times 10^9$  dyn/cm<sup>2</sup> range. When passing this range the samples usually shattered due to exceeding the yield strength.

It was also observed that compressive stresses increased the current flow while tensile stresses decreased the current flow. Also a trend that was consistently encountered was that for the same magnitude of stress applied, the compressive state had a more predominant effect as compared to the tensile state. The N<sup>+</sup> diodes under compressive stress resulted in a consistently greater influence (almost double) than the corresponding P<sup>+</sup> diodes.

Unfortunately, the stress influence on the reverse bias current was not analyzed due to current magnitudes being too low to measure at room temperature. However, a lower bound can be extracted from the forward bias influence studied. At the lower to mid-range stress levels studied, a maximum of 15 percent current influence was measured. The reverse bias current influence should be greater due to the fact that the recombination current component is more influenced by stress than the saturation current component.

## CHAPTER 1 SUMMARY AND FUTURE WORK

### 6.1 Summary

This thesis explores three different realms of mechanical stresses in silicon fabrication. The first is examining two modeling techniques for computing oxidation volume dilation-induced stress and integrating it along with other sources of stress. The main problem in this analysis is validating the models with experimental measurements. Since very few methods are available for this purpose, SKPM is investigated as a new method for characterizing localized stresses induced in STI processes. This involves understanding how the mechanical strain affects the crystal properties that can be measured, such as work function and band gap. To help understand these influences, another experiment is performed using pn-junction device electrical measurements to extract the strain influences on silicon crystal properties. The results of each task benefits the others as each has the common long term goal for improving the understanding how mechanical stress affects silicon technology and developing methods for alleviating it. Isolation processes are given special consideration as most mechanical stress problems in silicon technology are encountered there.

First, two multidimensional finite element methods are implemented to analyze mechanical stress generated by the oxidation growth process. The strain solutions from either method can be added to contributions from other sources, such as boron dopant, film, and thermal expansion mismatch. The two methods' solutions have been shown to agree qualitatively when solving for the strain induced due to the LOCOS process. At smaller nitride linewidths, the oxidation growth solutions begin to show differences due to the method utilized. Also for lower temperature re-oxidations, the STI corner rounding simulations disagreed. Under these conditions it then becomes necessary to solve for the strain in the silicon simultaneously, since it affects the strain solution in the oxide. Both techniques allow for solution from multiple strain sources simultaneously. This is necessary for analyzing stress generated from modern isolation processes such as STI and in DRAM technologies. The BL method is computationally optimized and therefore allows it to be useful for analyzing oxidation-induced strains in three-dimensions.

The solutions of stress induced by deposited nitride films are compared to Raman investigations via techniques introduced by De Wolf [52] and Jones [51]. The simulated Raman frequency shift for the nitride stack agrees both qualitatively and quantitatively with the measured data [52].

Simulations are also performed of the bending of boron-doped cantilevers due to their residual stress to examine the boron-induced strain

model. The simulations were then compared with studies of this effect and produced qualitatively favorable results. The simulations agreed with experiment in comparative bending between the different thickness cantilevers. The difference in deflection magnitudes can be attributed to the lattice strain parameter used in the model. By simply scaling this parameter, simulation deflection magnitudes would coincide better with the measurements. One possible explanation may be that the magnitude of the lattice strain parameter used may not apply since it was measured in samples with boron dopant introduced during silicon crystal growth instead of by thermal diffusion as in the cantilever experiment. Also there may be strain relaxation with a cantilever thickness dependence.

Next, SKPM is applied as a new technique to characterize the strain exerted from STI processes through measurements of work function variations in silicon. The STI experiment performed demonstrates a change in work function of silicon that is likely due to the strain induced by the STI process. The change in work function is also found to vary in magnitude depending on the STI densification anneal performed. Strain simulations are then performed to correlate the differences in work function influences to the strain induced by the densification anneals. It is found that the simulations of work function influence agree qualitatively with the measured influences. However, the measured influences' magnitudes are greater than the expected changes. This is believed to be due to the surface and biasing effects in the



SKPM measurements. Scaling the measurements to the simulated levels show the qualitative agreement over the scanned STI regions.

Finally, an experiment for quantifying the amount of uniaxial stress-induced current variation for various diode types has also been accomplished. Stress influenced measurements are performed for influences in the forward biased operation of pn-junctions. The results demonstrate that the measured influence of the applied mechanical stress was consistent among the different types of diodes. N+ diodes resulted in a greater influence due to the stress than the P+ diodes. It was also observed that compressive stresses increased the current flow while tensile stresses decreased the current flow. These measurements demonstrate how much low to mid stress levels influence pn-junction currents. The measured data provides a lower bound for how critical the uniaxial stress affects reverse current or leakage levels.

## 6.2 Future Work

The following are proposed ideas for future work related to modeling of mechanical strain induced by silicon fabrication processes:

### 6.2.1 SKPM Strain Measurement Calibration Studies

It would be useful to follow up the SKPM study with another experiment using a simpler more controllable stress source. An example of such could be depositing nitride with a high intrinsic stress directly on the silicon wafer and then pattern the nitride into stripes with varying



thicknesses and widths. Performing an SKPM scan below the nitride regions would allow for analyzing the silicon work function influences due to different levels of stress controlled by the thickness of the nitride films. Then the amount of work function shift can be correlated to strain by finite element simulations and micro-Raman investigations. Also, it could be possible to put multiple structures on the same sample to reduce work function influences due to sample preparation and measurement dependencies such as surface potentials and biasing influences.

#### 6.2.2 Effect of Stress on Dislocations

In this study, the work was focused on solving for the stress magnitudes due to various processes in silicon fabrication of integrated circuits. One consequence of highly stressed regions is the yielding of dislocations to relieve the strain in the silicon crystal. The dislocations formed then act as generation/recombination centers which worsen the device performance. It would be beneficial to begin correlating the amount of stress necessary to form dislocation densities which ultimately result in unacceptably high leakage levels. Such a study could perhaps be performed by intentionally stressing large pn-junction devices locally through either the isolation process or with films of high intrinsic stress. Then measuring influences in the leakage currents due to the stress applied as was done in chapter 5.

### 6.2.3 Silicidation-Induced Stress

Modern integrated circuit processes involve the growth of metal silicide materials for improved conductivities for interconnects between devices and contacts. During the titanium silicide growth process, a net volume contraction results due to the newly formed silicide occupying less volume than the reactant volumes of silicon and titanium. This is opposite behavior to that of silicon dioxide growth where a net volume dilation results.

This growth process may produce significant local mechanical stresses in regions such as at the gate and source/drain regions of CMOS devices formed by the silicide process. It would then be necessary to include titanium silicide growth as another strain inducing source when analyzing the strain in these regions which are critical for CMOS electrical characteristics. It is important to have an accurate strain field calculation in this active area region for examining the impact of mechanical strain on the evolution of the extended defects in the critical source/drain regions.

### 6.2.4 Three-Dimensional Modeling of the STI Process

STI technologies are rapidly becoming the standard isolation process in modern integrated circuits as minimum transistor lengths decrease below 0.25-micron. This scaling then leads to an increase in importance of three-dimensional isolation effects on device characteristics such as electric fields and leakage currents.

The main obstacle encountered in three-dimensional modeling of the STI process is a moving boundary grid handling problem. STI processes include multiple etch and depositions. These processes as well as the material growth processes encounter occasional problems in three-dimensions for handling the grid as the boundary front advances. Developments for correcting these problems are continuously resulting and has accounted for an increasingly robust grid handling in two-dimensions [66, 67]. Improving the three-dimensional grid handling routines [68] will allow for strain analysis of three-dimensional problems such as STI and DRAM structures.

## REFERENCES

- [1] D.-B. Kao, J. P. McVittie, W. D. Nix, and K. C. Saraswat, "Two-dimensional thermal oxidation of silicon-II. Modeling stress effects in wet oxides," *IEEE Transactions on Electron Devices*, vol. ed-35, pp. 25-37, 1988.
- [2] C. S. Rafferty, "Stress Effects in Silicon Oxidation-Simulation and Experiments," Ph. D. Thesis, Stanford, 1989.
- [3] S. K. Jones, D. J. Bazely, R. Beanland, G. Badenes, and B. Scaife, "Simulation of Advanced-LOCOS capability for sub-0.25 micron CMOS isolation," presented at SISPAD 97, Cambridge, MA, 1997.
- [4] A. Bohg and A. K. Gaiind, "Influence of film stress and thermal oxidation on the generation of dislocations in silicon," *Applied Physics Letters*, vol. 33, pp. 895-897, 1978.
- [5] Y. Tamaki, S. Isomae, S. Mizuo, and H. Higuchi, "Evaluation of dislocation generation at Si<sub>3</sub>N<sub>4</sub> Film edges on silicon substrates by selective oxidation," *Journal of the Electrochemical Society*, vol. 128, pp. 644-648, 1981.
- [6] C. Teng, G. Pollack, and W. R. Hunter, "Optimization of sidewall masked isolation process," *IEEE Transactions on Electron Devices*, vol. ed-32, pp. 124-131, 1985.
- [7] P. M. Fahey, S. R. Mader, S. R. Stiffler, R. L. Mohler, J. D. Mis, and J. A. Slinkman, "Stress-induced dislocations in silicon integrated circuits," *IBM Journal of Research and Development*, vol. 36, pp. 158-182, 1992.
- [8] X. J. Ning, "Distribution of residual stresses in boron doped p+ silicon films," *Journal of the Electrochemical Society*, vol. 143, pp. 3389-3393, 1996.



- [9] S. Mizuo and H. Higuchi, "Suppression by pre-diffusion annealing of anomalous diffusion of B and P in Si directly masked with Si<sub>3</sub>N<sub>4</sub> films," *Japanese Journal of Applied Physics*, vol. 20, pp. 1749-1750, 1981.
- [10] J. J. Wortman, J. R. Hauser, and R. M. Burger, "Effect of Mechanical Stress on p-n Junction Device Characteristics," *Journal of Applied Physics*, vol. 35, pp. 2122-2131, 1964.
- [11] G. Dorda, "Piezoresistance in Quantized Conduction Bands in Silicon Inversion Layers," *Journal of Applied Physics*, vol. 42, pp. 2053-2060, 1971.
- [12] S. T. Ahn, H. W. Kennel, J. D. Plummer, and W. A. Tiller, "Film stress-related vacancy supersaturation in silicon under low-pressure chemical vapor deposited silicon nitride films," *Journal of Applied Physics*, vol. 64, pp. 4914-4919, 1988.
- [13] D.-B. Kao, J. P. McVittie, W. D. Nix, and K. C. Saraswat, "Two-dimensional thermal oxidation of silicon-I. Experiments," *IEEE Transactions on Electron Devices*, vol. ed-34, pp. 1008-1017, 1987.
- [14] S. M. Hu, "Stress-related problems in silicon technology," *Journal of Applied Physics*, vol. 70, pp. R53-R80, 1991.
- [15] M. Dellith, G. R. Booker, B. O. Kolbesen, W. Bergholz, and F. Gelsdorf, "A Dislocation Formation Model of Trench-Induced Dislocations in Dynamic Random Access Memories," *Journal of the Electrochemical Society*, vol. 143, pp. 210-215, 1996.
- [16] K. Osada, Y. Zaitzu, S. Matsumoto, M. Yoshida, E. Arai, and T. Abe, "Effect of Stress in the Deposited Silicon Nitride Films on Boron Diffusion of Silicon," *Journal of the Electrochemical Society*, vol. 142, pp. 202-206, 1995.
- [17] C. Smith, "Piezoresistance Effect in Germanium and Silicon," *Physical Review*, vol. 94, pp. 42-49, 1954.
- [18] B. Kloeck and N. F. DeRoos, "Mechanical Sensors," in *Semiconductor Sensors*, S. M. Sze, Ed. New York, NY: John Wiley and Sons, Inc., pp. 153-204, 1994.
- [19] L. Kleinman, "Deformation Potentials in Silicon. I Uniaxial Strain," *Physical Review*, vol. 128, pp. 2614-2621, 1962.



- [20] L. Kleinman, "Deformation Potentials in Silicon. II. Hydrostatic Strain and the Electron-Phonon Interaction," *Physical Review*, vol. 130, pp. 2283-2289, 1963.
- [21] I. Goroff and L. Kleinman, "Deformation Potentials in Silicon. III. Effects of a General Strain on Conduction and Valence Levels," *Physical Review*, vol. 132, pp. 1080-1084, 1963.
- [22] J. J. Wortman and J. R. Hauser, "Effect of Mechanical Stress on p-n Junction Device Characteristics. II. Generation-Recombination Current," *Journal of Applied Physics*, vol. 37, pp. 3527-3530, 1966.
- [23] A. Hamada, T. Furusawa, N. Saito, and E. Takeda, "A New Aspect of Mechanical Stress Effects in Scaled Mos Devices," *IEEE Transactions on Electron Devices*, vol. 38, pp. 895-900, 1991.
- [24] C.-L. Huang, H. R. Soleimani, G. J. Grula, J. W. Sleight, A. Villani, H. Ali, and D. A. Antoniadis, "LOCOS-Induced Stress Effects on Thin-Film SOI Devices," *IEEE Transactions on Electron Devices*, vol. 44, pp. 646-650, 1997.
- [25] W. Rindner and I. Braun, "Resistance of Elastically Deformed Shallow p-n Junctions. II," *Journal of Applied Physics*, vol. 34, pp. 1958-1970, 1963.
- [26] I. D. Wolf, "Micro-Raman spectroscopy to study local mechanical stress in silicon integrated circuits," *Semiconductor Science and Technology*, vol. 11, pp. 139-154, 1996.
- [27] H. Rueda, S. Cea, and M. Law, "Mechanical stress modeling for silicon fabrication processes," presented at SISPAD 97, Cambridge, MA, 1997.
- [28] O. C. Zienkiewicz and R. L. Taylor, *The Finite Element Method*, vol. 1, 4 ed. London, U.K.: McGraw-Hill Book Company, 1987.
- [29] S. Timoshenko and J. N. Goodier, *Theory of Elasticity*, Third ed. New York, N. Y.: McGraw-Hill Book Company, Inc., 1970.
- [30] Y. C. Fung, *A First Course in Continuum Mechanics*, 3 ed. Englewood Cliffs, N. J.: Prentice Hall, 1994.
- [31] J. F. Nye, *Physical Properties of Crystals*. London: Oxford University Press, 1964.

- [32] J. J. Wortman and R. A. Evans, "Young's Modulus, Shear Modulus, Poisson's Ratio in Silicon and Germanium," *Journal of Applied Physics*, vol. 36, pp. 153-156, 1965.
- [33] W. A. Brantley, "Calculated elastic constants for stress problems associated with semiconductor devices," *Journal of Applied Physics*, vol. 44, pp. 534-535, 1973.
- [34] C. Kittel, *Introduction to Solid State Physics*, 7 ed. New York: John Wiley & Sons, Inc., 1996.
- [35] W. M. Bullis, "Silicon Material Properties," in *Handbook of Semiconductor Silicon Technology*, W. C. O'Mara, R. B. Herring, and L. P. Hunt, Eds. Park Ridge, New Jersey: Noyes Publications, pp. 422-434, 1990.
- [36] S. P. Nikanorov, Y. A. Burenkov, and A. V. Stepanov, "Elastic Properties of Silicon," *Soviet Physics-Solid State*, vol. 13, pp. 2516-2518, 1972.
- [37] P. B. Griffin and C. S. Rafferty, "A Viscous Nitride Model for Nitride/Oxide Isolation Structures," *International Electron Device Meeting Technical Digest*, pp. 741-744, 1990.
- [38] R. W. Hoffman, "The mechanical properties of thin condensed films," in *Physics of thin films: advances in research and development*, vol. 3, G. Hass and R. Thun, Eds. New York, NY: Academic Press, pp. 211-273, 1966.
- [39] E. H. Yang and S. S. Yang, "The quantitative determination of the residual stress profile in oxidized p+ silicon films," *Sensors and Actuators A: Physical*, vol. 54, pp. 684-689, 1996.
- [40] W.-H. Chu and M. Mehregany, "A study of residual stress distribution through the thickness of p+ silicon films," *IEEE Transactions on Electron Devices*, vol. 40, pp. 1245-1250, 1993.
- [41] F. H. Horn, "Densitometric and electrical investigation of boron in silicon," *Physical Review*, vol. 97, pp. 1521-1525, 1955.
- [42] C. S. Cargill, J. Angilello, and K. L. Kavanagh, "Lattice Compression from Conduction Electrons in Heavily Doped Si: As," *Physical Review Letters*, vol. 61, pp. 1748-1751, 1988.
- [43] M. E. Law, "Florida Object-Oriented Process Simulator, FLOODS/FLOOPS Manual," University of Florida, Gainesville 1993.

- [44] S. Cea, "Multidimensional viscoelastic modeling of silicon oxidation and titanium silicidation," Ph. D Thesis , University of Florida, 1996.
- [45] D. Chidambarrao, J. P. Peng, and G. R. Srinivasan, "Stresses in silicon substrates near isolation trenches," *Journal of Applied Physics*, vol. 70, pp. 4816-4822, 1991.
- [46] V. Senez, D. Collard, P. Ferreira, and B. Baccus, "Two-Dimensional Simulation of Local Oxidation of Silicon: Calibrated Viscoelastic Flow Analysis," *IEEE Transactions on Electron Devices*, vol. 43, pp. 720-730, 1996.
- [47] A. H. Perera, J.-H. Lin, Y.-C. Ku, M. Azrak, and B. Taylor, "Trench Isolation for 0.45um Active Pitch and Below," *International Electron Device Meeting Technical Digest*, vol. 95, pp. 679-682, 1995.
- [48] C. P. Chang, C. S. Pai, F. H. Baumann, C. T. Liu, C. S. Rafferty, M. R. Pinto, E. J. Lloyd, and M. Bude, "A Highly Manufacturable Corner Rounding Solution for 0.18um Shallow Trench Isolation," *International Electron Device Meeting Technical Digest*, vol. 97, pp. 661-664, 1997.
- [49] H. Rueda, I. Avci, S. Cea, and M. Law, "Modeling and Calibrated Simulation of Corner Rounding for Shallow Trench Isolation," presented at TECHCON 98, Las Vegas, 1998.
- [50] I. D. Wolf, H. Norstrom, and H. E. Maes, "Process-induced mechanical stress in isolation structures studied by micro-Raman spectroscopy," *Journal of Applied Physics*, vol. 74, pp. 4490-4500, 1993.
- [51] S. K. Jones, A. Poncet, I. DeWolf, M. M. Ahmed, and W. J. Rothwell, "An Advanced Calibration Method for Modelling Oxidation and Mechanical Stress in Sub-Micron CMOS Isolation Structures," *International Electron Device Meeting Technical Digest*, vol. 94, pp. 877-880, 1994.
- [52] I. D. Wolf, H. E. Maes, and S. K. Jones, "Stress measurements in silicon devices through Raman spectroscopy: Bridging the gap between theory and experiment," *Journal of Applied Physics*, vol. 79, pp. 7148-7156, 1996.
- [53] K. E. Peterson, "Silicon as a mechanical material," *Proceedings of the IEEE*, vol. 70, pp. 420-457, 1982.
- [54] H. Rueda and M. E. Law, "Modeling of Mechanical Strain in Borondoped Silicon Cantilevers," presented at MSM 98, Santa Clara, CA, 1998.



- [55] X. Ding, W. H. Ko, and J. M. Mansour, "Residual Stress and Mechanical Properties of Boron-doped p+ Silicon Films," *Sensors and Actuators A: Physical*, vol. 21-23, pp. 866-871, 1990.
- [56] J. E. Shigley, *Mechanical Engineering design*, Fourth ed: McGraw-Hill Book Company, 1983.
- [57] T. Hochwitz, "Implementation, Characterization, and Applications of a Scanning Kelvin Probe Force Microscope," Ph D Thesis , Dartmouth College, 1995.
- [58] A. K. Henning and T. Hochwitz, "Scanning probe microscopy for 2-D semiconductor dopant profiling and device failure analysis," *Materials Science and Engineering*, vol. B42, pp. 88-98, 1996.
- [59] M. Nonnenmacher, M. P. O'Boyle, and H. K. Wickramasinghe, "Kelvin probe force microscopy," *Applied Physics Letters*, vol. 58, pp. 2921-3, 1991.
- [60] M. Nonnenmacher, M. P. O'Boyle, and H. K. Wickramasinghe, "Surface investigations with a Kelvin probe force microscope," *Ultramicroscopy*, vol. 42-44, pp. 268-273, 1992.
- [61] A. K. Henning, T. Hochwitz, J. Slinkman, J. Never, S. Hoffmann, P. Kaszuba, and C. Daghlia, "Two-dimensional surface dopant profiling in silicon using scanning Kelvin probe microscopy," *Journal of Applied Physics*, vol. 77, pp. 1888-1896, 1995.
- [62] M. Masters, J. Slinkman, and P. Kaszuba, "Qualitative Kelvin Probing for Diffusion Profiling," presented at ISTFA 95, Santa Clara, 1995.
- [63] J. C. Hensel and G. Feher, "Cyclotron Resonance Experiments in Uniaxially Stressed Silicon: Valence Band Inverse Mass Parameters and Deformation Potentials," *Physical Review*, vol. 129, pp. 1041-1062, 1963.
- [64] P. Kaszuba, "A Technique for Achieving Ultra-Smooth Chip Cross Sections," presented at ISTFA 95, Santa Clara, 1995.
- [65] J. R. Patel and A. R. Chaudhuri, "Macroscopic Plastic Properties of Dislocation-Free Germanium and other Semiconductor Crystals. I. Yield Behavior," *Journal of Applied Physics*, vol. 34, pp. 2788-2799, 1963.

- [66] H. Rueda and M. E. Law, "Algorithms for the reduction of surface evolution discretization error," presented at SISPAD 95, Erlangen, Germany, 1995.
- [67] M. E. Law, "Grid adaption near moving boundaries in two dimensions for IC process simulation," *IEEE Transactions on Computer-Aided Design of Integrated Circuits and Systems*, vol. 14, pp. 1223-1230, 1995.
- [68] M. E. Law and M. Cerrato, "Improved Local Refinement Algorithms for Adaptive Meshing of Process Simulation Problems," presented at SISPAD 97, Cambridge, MA, 1997.



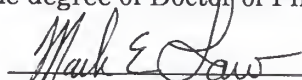
## BIOGRAPHICAL SKETCH

Hernan Adolfo Rueda was born in Chicago, Illinois, on November 9, 1970, to Hernan and Gloria Rueda. He has one brother, Camilo. Hernan grew up in Miami, Florida. He attended North Miami Senior High School and graduated in June 1988.


He then enrolled at the University of Florida in fall 1988 and earned his Bachelor of Science degree in electrical engineering in August 1992. During this time he developed interest in the fields of VLSI circuit design and fabrication and in computer programming.

In fall 1992, he began his graduate studies at the University of Florida, and soon thereafter he began his master's research in IC process modeling focusing on moving boundary problems. His doctorate research has focused on modeling and characterizing mechanical strain in silicon integrated circuit fabrication processes.

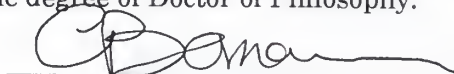
I certify that I have read this study and that in my opinion it conforms to acceptable standards of scholarly presentation and is fully adequate, in scope and quality, as a dissertation for the degree of Doctor of Philosophy.

  
Mark E. Law, Chairman  
Professor of Electrical and  
Computer Engineering

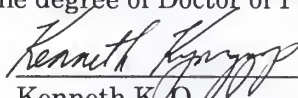
I certify that I have read this study and that in my opinion it conforms to acceptable standards of scholarly presentation and is fully adequate, in scope and quality, as a dissertation for the degree of Doctor of Philosophy.

  
Kevin S. Jones  
Professor of Materials Science and  
Engineering

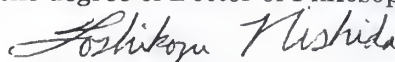
I certify that I have read this study and that in my opinion it conforms to acceptable standards of scholarly presentation and is fully adequate, in scope and quality, as a dissertation for the degree of Doctor of Philosophy.

  
Gijs Bosman  
Professor of Electrical and  
Computer Engineering

I certify that I have read this study and that in my opinion it conforms to acceptable standards of scholarly presentation and is fully adequate, in scope and quality, as a dissertation for the degree of Doctor of Philosophy.

  
Kenneth K. O  
Associate Professor of Electrical and  
Computer Engineering

I certify that I have read this study and that in my opinion it conforms to acceptable standards of scholarly presentation and is fully adequate, in scope and quality, as a dissertation for the degree of Doctor of Philosophy.

  
Toshikazu Nishida  
Associate Professor of Electrical and  
Computer Engineering

This dissertation was submitted to the Graduate Faculty of the College of Engineering and to the Graduate School and was accepted as partial fulfillment of the requirements for the degree of Doctor of Philosophy.

May 1999

---

Winfred M. Phillips  
Dean, College of Engineering

---

M. J. Ohanian  
Dean, Graduate School

LD  
1780  
1999  
R918

UNIVERSITY OF FLORIDA



3 1262 08554 4681